Signal Processing and Statistical Analysis of the Weather and Atmospheric Signals Using Radar Observations

A Thesis Submitted by

RAMYAKRISHNA ENUGONDA

(SC19D027)

In partial fulfilment of the requirements for the award of the degree of

Doctor of Philosophy

DEPARTMENT OF AVIONICS

INDIAN INSTITUTE OF SPACE SCIENCE AND TECHNOLOGY

Thiruvananthapuram – 695547

July 2023

CERTIFICATE

This is to certify that the thesis entitled **“Signal Processing and Statistical Analysis of the Weather and Atmospheric Signals using Radar Observations”** submitted by **Ms. Ramyakrishna Enugonda** (Roll No. SC19D027) to the Indian Institute of Space Science and Technology, Thiruvananthapuram, for the award of the degree of **Doctor of Philosophy**, is a bonafide record of the research work done by her under my supervision. The content of this thesis, in full or in parts, have not been submitted to any other Institute or University for the award or any degree or diploma.

Dr. V.K. Anandan	**Dr. Basudeb Ghosh**
Deputy Director	**Associate Professor**
Supervisor	**Supervisor**
RDA, ISTRAC	Department of Avionics, IIST

Thiruvananthapuram

July, 2023

Counter Signature of HOD with seal

DECLARATION

I declare that this titled **“Signal Processing and Statistical Analysis of the Weather and Atmospheric Signals using Radar Observations”,** submitted in fulfilment of the Degree of Doctor of Philosophy, is a record of original work carried out by me under the supervision of Dr.V.K. Anandan and Dr. Basudeb Ghosh, and has not formed the basis for the award of any degree, diploma, associate ship, fellowship or other titles in this or any other Institution or University of higher learning. In keeping with the ethical practice in reporting scientific information, due acknowledgements have been made wherever the findings of others have been cited.

E. Ramyakrishna
SC19D027

Place: Thiruvananthapuram

July, 2023.

Acknowledgements

First and foremost, I express my sincere thanks to my supervisor Dr V.K. Anandan for his support throughout my PhD studies and research; for his patience, motivation, enthusiasm, and insightful discussions. His guidance motivated me to become an independent researcher, which helped me write this thesis and the work that preceded it. I am grateful for his valuable discussions, suggestions and reviews. His expertise and valuable guidance helped me in seeking to achieve the best possible results in my research. I am truly thankful for his support and valuable career advice. I could not have completed this research without his support and help.

I am extremely grateful to Dr Basudeb Ghosh, my master, supervisor of IIST, for his inspiration, motivation, kind wishes, and positive energies that pushed me forward to pursue doctoral research. Besides my supervisor and co-supervisor, I would like to express my sincere thanks to the rest of my Doctoral committee members: Prof. Dr Rama Rao Nidamanuri, Dr Vineeth, Dr Deepak Mishra, and Dr Lakshmi Narayana for their encouragement, comments, and suggestions. I would like to acknowledge Shri. B.N Ramakrishna, the present Director and Dr. V.V.Srinivasan, the former Director of ISTRAC and Dr V.K. Dadhwal, the former Director of IIST and Dr.S.Unnikrishnan Nair, the present Director of IIST, for providing the research facilities and research fellowship. I would like to express my appreciation to the Dr. N.Selvaganesan, Head of the Department (HOD) of Avianics, entire staff and lab members of the department, library, Academics and administrative staff at IIST for their timely help. I would like to thank the anonymous journal reviewers for their constructive criticism and valuable suggestions.

I would like to thank C. Pradeep Kumar, Rajan, and Shahul Hameed for guiding me while learning techniques for analyzing stochastic signals and Doppler weather radar data. My discussion with Mr Rajan was a great source of learning for me. I am truly thankful for his patience. I wish to acknowledge with thanks to the Department of Radar Development Area (RDA), ISTRAC-ISRO. I would like to thank the all RDA employees for their assistance at various levels of my research.

Also, I sincerely thank all the administrative staff and library staff of ISTRAC and IIST. Remembering all my friends at ISTRAC who made life more lively and memorable.

I sincerely thank Dr T. Narayana Rao for his valuable suggestions and data.Thanks to National Atmospheric and Research Laboratory (NARL) for providing Weather and Atmospheric data.

I would like to acknowledge my teachers especially Dr. Vijaya Bhaskar Rao for his guidance.

Finally, my deep thanks go to my family. I am forever grateful for the unconditional love, support and encouragement from my parents who has made it possible for me to study for my PhD.

E. Ramyakrishna

Abstract

Higher Order Spectral Analysis (HOSA) is a very useful technique for analyzing the statistical relationships between several spectral components. HOSA can be defined in terms of Bispectrum as a third-order spectrum. This technique is useful for studying the statistical distribution of the signal when the additive noise sources are Gaussian in nature and also for studying the presence of nonlinearities in the signals. In some cases, the deviations from the Gaussian shape of the Doppler power spectrum can be considerable during severe weather conditions (due to the presence of strong wind shear and turbulence patterns), which exhibits skewed, sharp and bimodal signatures. The presence of turbulence in the atmosphere makes the process into nonlinear due to the wavenumber interactions between the eddies in a turbulent flow. Earlier studies used Bispectrum measurements to experimentally study the spectral energy transfer due to wavenumber interactions in a turbulent flow. Wavenumber triad interactions result from the quadratic nonlinearity of the Navier–Stokes equations. They are the fundamental energy transfer mechanism in fluid flows and manifest in Fourier space as triplets of three wavenumber vectors. To determine the strength of such interactions, one must measure the third-order spectra, commonly called Bispectra. One of the main reasons to consider HOSA on weather and atmospheric signals is to characterize the Doppler spectrum obtained through the backscattered echoes, which are generally skewed and have multiple peaks. The analysis also identifies deviations from Gaussianity and performs well in noisy environments. This technique will identify and detect the signals and better estimate moments for further processing. Also, it is useful to study the Bispectrum in turbulence measurements to investigate certain nonlinear properties, such as spectral energy transfer. Therefore, atmospheric signals have been considered to investigate the nonlinearities in the backscattered signals.

The main objective of this thesis is to analyze the weather and atmospheric signals to know their statistical distribution and find out any deviation occurring from the normality. It is also to investigate how the Bispectrum performs well under noisy conditions. This thesis also aims to study the nonlinearities present in the backscattered signals obtained from the MST radar.

The bispectrum technique has been applied to the complex time series data derived from a Polarimetric X-band Doppler Weather Radar (DWR) to understand the statistical distribution of the signals and the deviations from the Gaussian shape of the Doppler spectrum. The results of this analysis are compared with conventional techniques like the Fourier method and pulse pair technique. It is observed that through the bispectrum approach, the Gaussian noise components are

significantly removed from the backscattered signals and improves the detectability of the weather signals under noisy condition.

The backscattered signals from MST radar arise from the turbulence induced irregularities in the refractive index gradients. To study the presence of nonlinearities in the atmospheric signals, a novel approach has been proposed for the measurement of turbulent energy dissipation rate (ε) from Nonlinear Index (NLI) based measurements using the Higher Order Spectral Estimation (HOSE) technique. The Bicoherence obtained by this method has been applied to the backscattered signals received from the Mesosphere, Stratosphere and Troposphere (MST) radar, Gadanki. Here we considered both convective and clear air atmospheric observation for the analysis and calculated the Nonlinear Index (which represents the amount of nonlinearity in signals) for each range bin and observed that the index of nonlinearity indirectly provides information about turbulent intensity. An empirical relationship between the nonlinear index and turbulent energy dissipation rate has been established through regression models. The results of the turbulence energy dissipation rate (ε) calculated from the nonlinear index have been compared with the turbulence energy dissipation rate (ε) calculated from the spectrum width based method.

This thesis also developed an algorithmic approach to remove the noise and the ground clutter for weather signals to obtain the best quality of radar products such as Reflectivity, Velocity, and Spectrum width. Proper detection and estimation of signal and noise power measurements are important to generate the best quality of meteorological data products. Noise will be generated when the antenna intercepts the thermal radiation from various sources, including the sky, sun, ground, precipitation and man-made radiators, and it is constructively added to the receiver internal noise. In order to obtain the best quality of radar products, it is desirable to compute meteorological parameters by estimating noise power and removal of ground clutter. In this paper, an attempt has been made to study the Empirical Mode Decomposition (EMD) denoising techniques on weather radar signals in the presence of noise and ground clutter. EMD method is a time domain technique; it decomposes the signals into Intrinsic Mode Functions (IMF). Three different methods of EMD based denoising techniques have been considered and applied to the weather signals to check the best performance of the denoising technique and remove clutter. Limitations and advantages of these methods are brought out. In order to overcome the limitations of these approaches, we modified the techniques by adapting correlation based measurements. Moments have been estimated from these techniques and compared with the conventional methods like Pulse pair and Fourier based spectral moments.

CONTENTS

3. Higher order spectral analysis on weather signals………………………….. 47

4. Atmospheric Turbulence Measurements using Higher Order Spectral Analysis………………………………………………………………………… 70

List of Figures

List of Tables

Abbreviations

ADC	Analog to Digital Converter
AM	Amplitude Modulation
AP	Anomalous propagation
ASD	Auto correlation Spectral Density
BIC	Bicoherence
BITE	Built-in-test-equipment
CAT	Clear Air Turbulence
CAT	Clear Air Turbulence
CC	Correlation Coefficient
CFAD	Contoured Frequency by Altitude Diagrams
CLEAN-AP	Clutter Environment Analysis using Adaptive
CMD	Clutter Mitigation Algorithm
CPA	Clutter Phase Alignment
CR-EMDIT	Correlation based EMDIT
CR-EMDIT-EC	Correlation based EMDIT Energy Constraints
CSR	Clutter to Signal Ratio
CW	Continuous Wave
DAC	Digital to Analog Converter
DBS	Doppler Beam Swinging
DC	Direct Current
DWR	Doppler Weather Radar
EM	Electromagnetic Waves
EMD	Empirical Mode Decomposition
EMD-DT	Empirical Mode Decomposition Direct Threshold
EMD-IIT	Empirical Mode Decomposition Iterative Interval
EMD-IT	Empirical Mode Decomposition Interval Threshold

FFT	Fast Fourier Transform
fGn	Fractal Gaussian Noise
FM	Frequency Modulation
FPGA	Field Programmable Gate Array
FT	Fourier Transform
GMAP	Gaussian Model Adaptive Processing
GMM	Gaussian Mixture Model
GPPP	Generalized Pulse Pair Processing
GUI	Graphical User Interface
HOS	Higher-Order Statistics
HOSE	Higher Order Spectral Estimation
HOSM	Higher Order Spectral Moments
IMD	Indian Meteorological Department
IMF	Intrinsic Mode Function
IOT	Internet of Things
ISRO	Indian Space Research Organization
IST	Indian Standard Time
KHI	Kelvin Helmholtz Instability
LO	Local Oscillator
MCF	Mode Cell Filtering
MST	Mesosphere, Stratosphere and Troposphere
NGI	Non-Gaussianity Index
NLI	Nonlinearity Index
NP	Normal Propagation
NRGB	Number of Rangebin
NS	Navier-Stokes equation
OCXO	Oven Controlled Crystal Oscillator

OMT	Object-modeling technique
PC	Personal Computer
PHIDP	Differential Phase
PPI	Plan Position Indicator
PPP	Pulse Pair Processing
	Processing
PRT	Pulse Repetition Rate
PSD	Power spectral Density
PSU	Power Supply Unit
RADAR	Radio Detection and Ranging
RF	Radio Frequency
RMS	Root Mean Square
RMSE	Root Mean Square Error
SAM	Spaced Antenna Method
SCI	Spectrum Clutter Identification
SNR	Signal to Noise Ratio
SPDT	Single Pole Double Through
SSPA	Solid State Phased Array
STAR	Simultaneous Transmission and Alternative Reception
STD	Standard Deviation
SW	Spectrum Width
TDBZ	Texture of reflectivity
	Threshold
UPS	uninterruptible power supply
V	Velocity
VAD	Velocity Azimuth Display
VHF	Very High Frequency

VSSC	Vikram Sarabhai Space Centre
VVP	Volume Velocity Processing
ZDR	Differential Reflectivity

Nomenclature

Φ	Phase Shift
ω	Doppler angular frequency
F	Doppler frequency shift
$\boldsymbol{\lambda}$	Radar Wavelength
r	Range resolution
R	Range
v	Velocity
σ	Spectrum width
P_t	Transmitted Power
S_i	Power density
G	Antenna Gain
A_e	Effective aperture area of the radar antenna
P_r	Received Power
$\boldsymbol{\theta}$	Beamwidth(horizontal)
h	Pulse length
ϕ	Beamwidth (vertical)
$\|K\|^2$	The dielectric factor
D_i	Scatterer diameters
Z	Reflectivity
$\hat{v}$	Radial Velocity
$\hat{\sigma}_v$	Spectrum width
$\hat{S}$	Signal Power
N	Noise Power
T_s	Pulse Repetition Time
v_h	Horizontal wind speed

δ	Horizontal wind direction
ε	Turbulence eddy dissipation rate
u	Zonal component of velocity
v	Meridional component of velocity
w	Vertical component of velocity
N	Brunt Vaisala Frequency
η	Volume Reflectivity
C_n^2	Refractive Index Structure Constant
M	Refractive Index
Ri_c	Critical Richardson number
q	Specific Humidity
σ_{shear}^2	Spectral Broadening due to shear
σ_{beam}^2	Spectral Broadening due to beamwidth
σ_{wave}^2	Spectral broadening due to Atmospheric waves
U_h	Horizontal Wind Speed
L_t	Thorpe length
l_0	Inner scale of turbulence
v	Kinematic Viscosity
ρ	Atmospheric density

Chapter 1

Introduction

Various weather and atmospheric phenomena occur in the atmosphere of the Earth, which changes with time. The Doppler Weather Radar (DWR) is one of the remote sensing instruments that can be used to study the various weather and atmospheric phenomena, such as precipitation, clouds and other dynamics of the atmosphere, and it can also detect the radial velocities, wind speed, and direction, in heavy rainfall and clear air areas.

The backscattered signals received from the radar undergo various processing and filtering before estimating radar parameters. Sometimes, the existing methods will produce biased estimates in the case of ground clutter and noise. The returns from the non-moving ground targets generate the ground clutter echoes. Another problem is extracting the radar return signals in the low SNR environment where the receiver system is configured for a very large dynamic range of observation, and also, the estimates will produce severe bias, especially in the case of deviations occurring from the observed Doppler power spectrum. For example, autocovariance (pulse pair) processing is an extensively used technique in DWRs for the estimation of Doppler moments; even though it is considered as the most efficient estimator, this technique is valid under the assumption of a symmetric weather spectrum. But this assumption may not be valid in severe turbulent conditions associated with wind shear. Some studies showed that as the skewness increases, the Pulse pair method produces biased estimation in both velocity and spectrum width measurements (Doviak, 1984).

The complexities of the physical processes within the atmospheric system make it difficult to understand whether the process actually is a Gaussian/non-Gaussian and Linear/Nonlinear during severe weather events like strong wind shear and turbulence. Generally, it is assumed that the atmospheric and weather signals have Gaussian characteristics. But this assumption may not be valid during severe weather conditions (such as strong wind shear and irregular turbulence patterns). In some conditions, the Doppler power spectra exhibit deviations from the Gaussian shape and also exhibit nonlinear behaviour observed from the backscattered signals. Nonlinearity identification in the system is generally based on input and output data. Such datasets can be generated for an ideally controlled system, but the control of the input is not possible for some natural processes to measure directly. Therefore, measurements are derived indirectly. Even though, the man-made systems are linear, the system will exhibit nonlinear behaviour at certain conditions (Huang,1998). For example, the atmosphere is governed by generalized equations such as the dynamics of fluids and thermodynamics. The generation of turbulence in the atmosphere will create nonlinearity in the processes (Pope, 2000). The quadratic nonlinearity of the Navier–Stokes equations results wavenumber traid interactions between eddies and this is the main mechanism of energy transfer in fluid flows. In Fourier space, as triplets of three wavenumber vectors. To better understand the process associated with the weather and atmospheric system, we need to develop sophisticated algorithms and approaches to extract the weather information from these radars using proper filtering and processing. In atmospheric radars (wind profilers), most of the signals received from the vertical beam have non-Gaussian characteristics. This study has been clearly explained by Anandan et al. (2001).

Nowadays, many meteorological products are generated from the base products of Doppler Weather Radar (DWR) observations. In India, recently, a number of Polarimetric DWRs are being developed and installed. Already, many studies are carried out in the field of weather signals from the observations of Polarimetric DWR. Whereas, in India, the study related to DWR observations are in a nascent stage and the algorithm used for extracting the signals follows the moments extraction technique followed in statistical theory. There is a need for efficient algorithms to be developed and tuned specifically to the Indian meteorological conditions influenced by very different terrain topography compared to the algorithms already existing and developed outside India. In addition to this, there is a need to understand the statistical properties of the signal and the process associated with it, using novel approaches and algorithms. It is planned to have a study in this direction to develop more efficient algorithms for estimating weather and atmospheric parameters. It opens up looking into weather and atmospheric signal properties in different ways by applying various signal processing techniques, thereby enhancing the capability of signal extraction techniques leading to better estimation and parametrization.

1.1 Statistical distribution of the received signals

It is assumed that the statistical distribution of I (in-phase) and Q (quadrature-phase) parts of the backscattered signals obtained from the pulsed radar follows the Gaussian distribution

(Papoulis 1965). The received echoes in the resolution volume results from the sum of the distinct scattered echoes from all scatterers. With respect to the Central Limit Theorem, the sum of independent random variables likely to have a Gaussian density function, which is absolutely true for hydrometeor echoes. Therefore, I and Q components have a Gaussian distribution. The received signals have features similar to the Gaussian noise with narrowband seen in communication theory (Middleton, 1960). The absolute value of the complex weather signal follows a Rayleigh distribution (Bringi, 2001). The Rayleigh distribution fits the signal amplitude measurement well. The echo intensity is distributed as an exponential density function. These distributions can be used to determine the characteristics of estimators obtained from received signals. But, in real-time applications, this assumption is not fully valid. Sometimes, we may observe the deviations from the above distribution having the presence of Gaussian distribution and its changes along with nonlinearities in the received signals from both weather and atmospheric radars during severe weather events.

1.2. Literature Review

1.2.1 Non-Gaussian Doppler spectra observations

The power spectrum of the radar backscattered echoes gives the power-weighted radial velocity distribution inside the radar resolution volume. Power, mean radial velocity and spectrum width (zero, first and second moments) are the important parameters of the radar, that can be estimated by spectral methods (frequency domain) or the auto covariance method (time domain). The first three moments are sufficient for Gaussian-shaped Doppler spectra to characterize the power spectrum fully. However, there are only limited studies are available to systematically investigate and verify the Gaussian assumption using current Doppler weather radar. It has been observed that, the Doppler spectral shape is not exactly Gaussian in many weather events, The mean radial velocity and spectrumwidth can be obtained using the auto covariance method, and this method will be biased (Sirmans and Bumgarner, 1975) for non-Gaussian or asymmetric spectra.

The pulse pair processing method, often used for its robustness and computation efficiency, can obtain the radar parameters based on the Gaussian assumption, like reflectivity, mean radial velocity and spectrum width. However, size of the resolution volume of the radar increases with the detection range, resulting in the volume filling non-uniformly with different hydrometeors distributions. As a result, the spectrum may deviate from a Gaussian form. Many literatures have been reported already that, in some cases, deviation from Gaussian shape can be considerable during strong convective events: the main reason for this isthe presence of strong wind shear and irregular patterns of turbulence (Janssen, 1985; Yu et al., 2009) which shows skewed or sharp and, bimodal signatures (Dong, 2022). Janssen (1985) observed the deviation from the Gaussian shape from the precipitation spectra. To quantify this, they estimated spectral variability to know its deviation by fitting a parabola to an observed Doppler power spectrum. On a logarithmic scale, the Gaussian shape can be regarded as a parabola. Applying the least square criterion fits these spectrum estimates to a linear curve at degree 2. All readings will be performed at levels below the noise threshold except for spectral data exceeding a noise limit of 5dB. Such a constraint avoids troublesome transitions from the noise level to the power spectrum and vice versa. For deviations from Gaussian shape, it is appropriate to assume a squared mean difference between the fitted parabola and computed spectrum. There's a term for that, spectral variability. He discovered that there may be significant deviations from Gaussianity in about a fourth of the spectra.

Some studies examined deviations from the Doppler power spectra of a tornadic supercell thunderstorm. They observed that, the spectra exhibiting non-Gaussian, skewed, flat top behaviour during severe weather events. Yu et al. (2009) observed spectral deviations during a tornadic supercell event, which exhibits features like dual peak spectra. To study this feature, he modelled dual Gaussian (mixture of two Gaussian components) spectra for better observation of the spectra. Additionally, he measured the asymmetry and tailedness of a distribution using skewness and kurtosis. For the estimate of six spectral moments, he applied a nonlinear fitting algorithm to compare them with those obtained by an autocovariance method. Furthermore, he produced theoretical bias values of the mean radial velocity and the spectrum width acquired by the auto covariance approach in accordance with the six spectral moments.

Dong (2022) proposed a new generalized PPP (GPPP) technique to detect the non-Gaussian spectral signals using higher-order spectral moments (HOSM). This method calculates the higher-order spectral moments using the autocorrelation function and includes other two parameters, such as skewness and kurtosis, which describe the power spectral density (PSD) shape. They employed theoretical skewness and kurtosis values of 0 and 3, respectively, in their analysis. The Gaussian mixture model (GMM) was utilized to represent the weather signal, and the elbow approach was employed to determine the number of Gaussian spectra in

GMM. The parameters of the GMM are obtained by using the Expectation Maximization (EM) algorithm, which is similar to iterative optimization algorithm for estimating the parameters of probability models. In this case, they obtained initial values using the K-means clustering algorithm.

Williams (2018) estimated skewness and kurtosis for different Doppler spectra shapes observed from the Ka-band (35GHz) radars operating in the vertical directions. Thus, it is important to detect the non-Gaussian Doppler power spectrum, also required to develope the appropriate suitable algorithm for estimating spectral moments. For weather radars, reflectivity, velocity, and spectrum width can be calculated using autocovariance processing based on the assumption of the Gaussian spectrum model, and it will produce a biased estimation of moments in case of Doppler spectrum deviates from Gaussianity.

Many works have been reported for the estimation of spectral moments in spectral domain processing. Warde et al. (2014) proposed Autocorrelation Spectral Density (ASD) estimator for weather signals analysis, which is a generalization of the conventional Power spectral density (PSD). The Prony method was suggested by Lee (2010) for the detection of hazardous weather conditions. But this method has some computationally more complicated limitations, and additional processing is required for spectrum width calculations.

A new nonparametric approach has been developed for the estimation of spectral moments by Dias (2000). He assumed that the power spectral density function is band-limited in this approach. Lagha (2006, 2013) used the Ramanujan Fourier Transform technique and wavelets method for estimating the spectral moments of weather radar echoes. A new method Minimum mean square estimator was proposed for the estimation of the Doppler power spectrum by Yoshikawa (2021). Based on the features extracted from the Bicoherence, a new turbulence hazard detection technique has been established by Naumenko (2016).

During strong convective weather events, especially inthe case of Doppler power spectra deviation from the Gaussian shape,which shows the bimodal, skewed signatures, we should not consider the pulse pair technique for moment estimation because it produces a biased estimation of moments. Zhang et al. (2014) used a vast number of precipitation signals to obtain the Doppler power spectra, and they observed that the spectral shape is related to the width of the spectrum. As a result, a signal with a broad spectral width can considerably generate a non-Gaussian spectrum shape.

To verify this Gaussian assumption, we have analyzed the backscattered signals received from the polarimetric Doppler weather radar during severe convective events. We investigated the shape of the Doppler spectra using higher-order spectral analysis. Assuming that the noise generated signal has Gaussian distribution. For Gaussian signals, the cumulants spectra of order more than two are approximately zero. If a non-Gaussian signal is received with the additive Gaussian noise, transforming it to a higher-order cumulants domain will eliminate the noise. Hence, there is a specific advantage in applying bispectrum analysis to signals of non-Gaussian characteristics for their detection and parameter estimation, particularly in dealing with the signals from the region of poor signal-to-noise ratio (Nikias and Mendel, 1993; Giannakis et al., 1990).

1.2.2 Nonlinear identification

This thesis not only discussing about identifying the non-Gaussianity but also discussing about identifying the presence of nonlinearities in the backscattered signals. The main motivation to study the nonlinearities in the signals is the presence of atmospheric turbulence. Atmospheric turbulence causes spectral width enhancement in radar observations, making the process into nonlinear.

Many studies have developed statistical tests to check the linearity and Gaussianity of the signals. Initially, Rao and Gabr (1980) developed a statistical test for whether the process is Gaussian or linear using Bispectrum approach. Afterwards, Hinich (1982) presented a simple approach to check the Gaussianity and linearity of a data. He showed that, for Gaussian signals, the skewness function is a central chi-square (χ^2) distribution with two degrees of freedom. By using this information, he created a statistical hypothesis test to identify the linearity in the signals by examining the Bicoherence value at each frequency in the principal domain. When applied to each of the bifrequencies in the principal domain of the squared bicoherence plot, the likelihood of false detection is enhanced by a significant number of bifrequencies in the principal domain. As a result, the number of bifrequencies with significant bicoherence magnitude is underestimated. Finally, Choudhury et al. (2004) created two new indices to identify nonlinearity and non-Gaussianity in signals: the non-Gaussianity Index (NGI) and the nonlinearity index (NLI).

Fourier representation of the turbulence fields provides information on the dissipation rate of homogeneous isotropic turbulence (Pope, 2000). Navier-Stokes (NS) equation (second order partial differential equation, which is useful to describe the flow of viscous fluids) contains one nonlinear term, called the convective term. After applying a Fourier transform, this term becomes nonlinear and nonlocal as it involves interactions of wavenumber triads. Pope (2000) gave a complete description of the transport equation of turbulence in the spectral space. Triad interactions refer to the elementary momentum exchanges between Fourier components of the velocity field in wave vector space (Domaradzki, 1990). Discussions on nonlinear triad interactions of homogeneous turbulence in spectral space and detailed behaviour of the energy transfer function are reported by Orszag (1970), Domaradzki (1990), and Waleffe (1992). Several writers have pointed out the need of addressing local versus nonlocal triad interactions in isotropic turbulence models (Yeung, 1995; Moffatt, 2014; Praskovsky et al., 1993; Domaradzki, 1990; Zhou, 1993a and b; Waleffe, 1992).

1.3 Bispectral Measurements in Turbulence Analysis

Turbulence generation in the atmosphere is considered as a chaotic phenomenon in meteorology. Atmospheric turbulence can be generated by static and dynamic instability, which is related to buoyancy and shear mechanisms. Clear air turbulence (CAT) is normally associated with shearing, and convective turbulence is associated with buoyancy. CAT is the erratic air currents that occur in cloudless regions that cause violent aircraft buffeting. This turbulence is associated with wind shear commonly occurring at higher altitudes. Convective turbulence is commonly caused by thunderstorms which havestrong updrafts and downdrafts. If the atmosphere is more turbulent, nonlinear interactions between eddies results in coupled spectral frequency components in the backscattered signals received, which can be identified by the higher-order spectral analysis. The detailed discussion of Higher order spectral analysis and Bispectrum has given in Chapter 3.

Bispectral measurement studies have been done (Lii et al., 1976; Van Atta, 1979) experimentally to investigate the spectral energy transfer due to wavenumber interactions in a turbulent flow. Various works of literature are available on applications of Bispectrum in turbulence measurements (Yamada, 2010; Hasselman, 1963; Helland, 1978; Yeh, 1973; Herring, 1980). The quadratic nonlinearity of the Navier-Stokes equations determines the interactions between wave number triads. They make up the fundamental mechanism for energy transfer in fluids, manifesting as triples of three wavenumber vectors in Fourier space. The third-order spectra, usually known as bispectra, must be measured in order to establish the strength of these interactions. Investigating certain nonlinear properties, such as the transfer of spectral energy, is a major motivation for the characterisation of the Bispectrum in turbulence measurements (Lii et al., 1976).

Similar kinds of observations have been made experimentally by Yeh and Van Atta (1973), Lii et al. (1976), and Helland et al. (1978). Van Atta (1979) has done the derivations of the spectrum corresponding to the net transfer of energy from one wavenumber to another wavenumber. He showed three types of interactions among triads of wavenumbers related to the Bispectrum.

Therefore motivated by these observations, in this thesis, we aim to study the presence of nonlinearities in the backscattered signals using Higher order spectral analysis; for this, here, we considered data collected from the MST radar, located at Gadanki.

1.4 Parameter Estimation

Two approaches are mainly adapted for estimating radar parameters (such as power, velocity and spectrum width). 1. Autocovariance or Autocorrelation (Pulse pair processing) and 2. Fast Fourier Transform methods. The autocovariance method calculates the first two moments of the Doppler spectrum from estimates of the autocovariance function at lag Ts. The second method uses the Fourier transform for the estimation of spectral moments. The technique was first used in 1968 by Woodman and Hagfors (1969) for estimating the electromagnetic drift of ionosphere plasma at Jicamarca andfor stratospheric and mesospheric applications. The autocovariance method performs nearly the same as the spectral moments estimation method. Still, it is limited in discriminating against fading ground clutter or any other kind of interference, and itis very sensitive to the pre-filtering of the time series by matched filter (Woodman, 1985). The spectral moments estimation has become simple using the Fast Fourier Transform algorithm developed by Blackman and Tukey (1958). Now most of modem radars use the power spectrum approach for real-time implementation. However, in practice, the problem is complex because the signal is contaminated with noise and ground clutter.

The radar antenna receives most of the noise contributions from the surroundings (Bringi, 2001). The main source of noise is external (such as galactic noise, cosmic background noise, solar noise, Earth noise, noise due to precipitation, and noise from nearby structures such as buildings and radome, etc.) and internal (such as thermal noise and shot noise) contributions to the receiver system. This noise should be calculated properly for estimating base products, such as Reflectivity, Velocity and Spectrum width. There are different ways of measuring noise on weather radars, where after each volume scan, a calibration is performed as part of the online system. This measurement is performed at a high antenna elevation angle, and results will be adjusted by the use of predefined correction factors for additional antenna elevations. Radar systems cannot perform calibrations in online, therefore, the noise power should be measured in offline (Ivic, 2010, 2013). The noise power has angular dependence in both azimuth and elevation. Several methods have been proposed in the past for noise level calculations. Hildebrand and Sekhon (1974) proposed a method of estimating noise level in the spectral domain, where Fourier coefficients are discarded recursively until statistical conditions are satisfied. Urkowitz (1992) applied the Kolmogorov Smirnov test to the periodogram by successively discarding the Fourier spectral lines until the noise hypothesis was met. To determine the level of noise in a dynamic way, Siggia (2004) used ranked order statistics on power spectral density estimates. There are some limitations in the previous methods, which are discarding the excess spectral coefficients until the remaining ones satisfy the statistical conditions for the noise. To overcome these limitations, Ivic et al.(2010) suggested a technique that dynamically estimates the system noise power from in-phase and quadrature (I and Q) components in a radial direction. This method uses the radar range resolution volumes, which do not contain weather signals and uses those volumes to estimate the noise power.

For the identification of noise levels and removal of undesirable spectrum lines, different methods have been used for atmospheric radars. Donaldson (1967) set a noise limit of 10dB below the spectral peak that can lead to considerable error in estimating the spectrum variance and vertical air velocity by using modified Batten method. (Atlas, 1973). An objective approach to noise threshold determination has been employed by Hildebrand and Sekhon (1974). The method does not rely on knowledge of the noise levels in a radar instrument system; observed Doppler spectrum and physical characteristics of white noise are used. Nowadays, this method is widely used in atmospheric radar for noise level calculation and removal. A source of additional problems is the presence of ground clutter in the received signals. Sometimes ground clutter contaminates the weather signals and introduces bias in the meteorological variables. Under strong clutter contamination conditions, reflectivity estimates are falsely over estimated, and Doppler velocities and spectrum widths are shifted toward zero (Li, 2013). If we ignore the clutter contaminations, these biases could transmit into the algorithms and models that depend on weather radars.

It has been treated with a variety of techniques to reduce or eliminate its effects. The signal from the ground clutter consists of a spectral signature, which is essentially a single spectral line at the origin, with a strength dependent on the ground shielding of the radar. It is at least comparable to the signal and often many orders of magnitude higher, for atmospheric radars at tropospheric or stratospheric heights. To be exact, getting rid of those signals is very difficult. One way to eliminate its biasing effect is to ignore thefrequencies around zero (dc) frequency. This is possible only when the spectral offset is larger than its width.

Although conventional filtering is frequently used to remove ground clutter from weather signals, this filter may suppress the weather signal components that present near-zero frequency and produce a biased estimation of moments. Even though Gaussian Model Adaptive Processing (GMAP) works well to remove the ground clutter, applying GMAP at every gate consumes more time. Many clutter detection and removal algorithms have been developed (Groginsky, 1980; Sachidananda, 2000; Siggia, 2004; Hubbert, 2009 I and II; Ice, 2009; Yinguang, 2011; Li, 2013;Zhang,2014; Williams, 2018) and used in the weather radar community.

To significantly remove noise fluctuations and presence of ground clutter, we have applied Higher order spectral analysis on weather signals and implemented Empirical Mode Decomposition (EMD) based denoising and clutter removal algorithm for weather signals. The description of EMD and its denoising techniques has been given in Chapter 5.

1.5 Motivations and Objectives of the Thesis

Therefore, motivated by these observations, higher order spectral analysis has been performed on both weather signals and atmospheric signals to clearly understand the deviation from Gaussianity happening from the precipitation echo and suppress the noise components which has Gaussian distribution and study the presence of nonlinearities with the help of Bicoherence obtained from the Bispectrum. We observed that the actual Doppler profile observed from X-band Doppler Weather Radar during the convective event shows the skewed and dual peak signatures in the Doppler spectra. It has been observed that noise components are suppressed significantly.The same can also be expected in weather signals; if it is purely Gaussian, it will become zero, but we observed slight deviations observed from the precipitation spectra, which can be expected in severe weather events. Therefore, peak detection has been improved. It can be clearly seen from the results presented in Chapter 3.

The higher-order spectral analysis, also known as Bispectrum, is useful for identifying nonlinearities present in the signals. Previous studies have used bispectral measurements for experimental purposes to study spectral energy exchanges due to interactions of wavenumber in a turbulent flow, which is briefly discussed in the manuscript, and this is one of the main motivations for considering HOSE on Atmospheric signals.This kind of nonlinear interaction among eddies can be studied using HOSE (Lii. et al., 1976; Van Atta, 1979).

1.5.1 Objective

The main objective of this thesis is to understand the process associated with backscattered signals observed from the weather and atmospheric radars. Therefore, it is planned to develop an efficient algorithm to study the statistical properties of weather signals under varying noise conditions and to find deviations from the Gaussian shape of the precipitation spectra during severe weather events (strong convective events). Thereby improving the spectral estimations, mainly first and second-order moments, by removing noise and clutter present in the Doppler power spectrum. The pulse pair estimator will be biased for meteorological targets with high spectrum widths. Therefore, using higher-order spectral analysis provides an improved estimation of the velocity and spectrum width. Also, this thesis focused on studying atmospheric turbulence analysis using Higher order spectral analysis and developing algorithms for the turbulence eddy dissipation rate based on nonlinear index-based measurements, which is the first of its kind.

A sequence of three specific objectives, listed below, is proposed to develop efficient algorithms for weather signals and atmospheric signals.

1. Development of an efficient algorithm to understand statistical properties of weather signals under noise-varying conditions and to find out the deviations occurring from the Gaussian shape of the precipitation spectra during severe weather events (strong convective events).
2. Development of a novel approach for estimating turbulent kinetic energy dissipation rate (which measures the turbulence intensity) from nonlinear index-based measurements, which gives an indirect measurement of turbulence intensity without any system-dependent corrections.
3. Development of a new EMD correlation-based algorithm for denoising and clutter removal in weather signals.

4. Study of Temperature sheets using Higher Order Spectral Analysis observed from the MST (VHF) radar based on the above observations and new estimation approaches.

1.6 Structure of the thesis

The thesis has been organized as follows.

Chapter 2 discusses the system description and processing of time series data. This chapter also discusses the extensive survey of the literature work on various noise and clutter removal techniques for weather radar signals.

Chapter 3 presents a study of the statistical distribution of weather signals (any deviations occurringfrom normality during severe weather events) under varying noise conditions. Skewed or sharp and bimodal signatures were observed from the precipitation spectra. This chapter provides a general background of the bispectral analysis reported in the literature that is the basis of the research. This chapter also discusses the data being used and the analysis carried out and gives details of the results obtained through this analysis and its impact on the weather signal estimation and parameterization, and provides the conclusion derived from the research work.

Chapter 4 provides an overview of atmospheric turbulence and methods using both radar and radiosonde based measurements. This chapter describes the novel approach proposed for atmospheric turbulence. This chapter also briefly discusses data analysis and describes the results obtained. This chapter also compares the results obtained through both approaches with the proposed method and gives the conclusion.

Chapter 5 provides a study of Empirical Mode Decomposition based denoising techniques and clutter removal algorithms for weather signals.

Chapter 6 providesa study of temperature sheets observed from the VHF radar using Higher order spectral analysis.

Chapter 7 provides a summary and overall conclusions of the previous chapters and presents some ideas for future works.

Chapter 2

Radar system description and Data Processing Techniques

2.1 RADAR Introduction and its basic principles

RADAR (RAdio Detection And Ranging) is an electromagnetic sensor that can detect, locate, and identify a target. S.M. Taylor of the U.S. Navy and F.R. Furth in November 1940, established that term. The acronym is the result of an agreement between the Allied powers in World War II, which had been adopted in 1943 and subsequently was generally accepted around the world. RADAR is considered as the first modern remote sensing technique used in meteorology. Radars operate on the echo sounding concept. When an electromagnetic wave is transmitted, some of the energy in the radiation is scattered in all directions, some part is transmitted, some part is reflected, and the object's material observes some part. The radar will measure the distance and movement of the target by analyzing the received signal. The time delay between the transmitted pulse and received pulses gives information about the target's range and radar cross-section. When the target is moving, the signal returned comes from a Doppler shift in the transmitted frequency. The velocity of the line of sight to the target is determined by this Doppler shift.

Assume the target moves with a radial component of velocity v, and the range (r) and phase shift (Φ) vary constantly. A frequency is defined as a change in Φ with regard to time. This is known as Doppler angular frequency, and it is denoted by,

$$\omega = 2\pi F = d\Phi/dt = (4\pi/\lambda)*(dr/dt) = 4\pi v/\lambda \qquad (2.1)$$

where F is the Doppler frequency shift

$$F = 2v/\lambda = 2vf/c\ , \qquad (2.2)$$

$$v = F\lambda/2 \qquad (2.3)$$

Nowadays, two types of radars are available. Continuous Wave (CW) radar, for example, emits a continuous sine wave. As a result of the phase shift, the transmitted radiation can identify the received echo. The second one is pulsed radars which use a pulsed carrier frequency instead of CW carrier frequency. These radars are developed to mitigate the problems that exist in CW radars. Unacceptably wide range ambiguity, for most applications, is a significant limitation of CW radar operations at microwave frequencies. Radar normally consists of a transmitter, receiver, duplexer and antenna. Radar systems can be monostatic or bistatic; with monostatic radar, the transmitter and receiver are in the same location, but in bistatic radar, the transmitter and receiver are at different locations.

Several types of pulsed radars have been developed and used in various applications, such as Doppler weather radar, Atmospheric radar, Synthetic Aperture Radar and Imaging radar etc.

2.1.1 Frequency Bands in Radar Applications

Transmission frequencies ranging from few MHz to 100 GHz are employed to identify atmospheric scatterers. Electromagnetic waves scattering characteristics are highly dependent on their wavelength. Therefore, in the context of remote sensing applications, the best combination of all scattering mechanisms is with a certain band of wavelength. Usually the objective particles size is between several micrometres to several mm. Therefore, electromagnetic waves with wavelengths ranging from mm to a few cm have been considered for these targets so that the particles can be identified. In atmospheric applications, The major source of scatterers is caused by the refractivity index fluctuations created by turbulence in the atmosphere and waves. The refractive index is subject to changes over a large range of spatial scales. In atmospheric radar measurements only scattered from a certain spatial scale corresponding to half of the radar wavelength is detected. Therefore, the backscatter from refractive index perturbations can be easily observable by utilizing radar wavelengths at twice the largest scales of perturbations. Therefore, weather radars are useful for observing precipitation, which operates at wavelengths between 3 and 10 cm. The targets of these radars are clouds and hydrometeors. Fig.2.1 shows the operating frequency band of the individual radars and their adjoining bands.

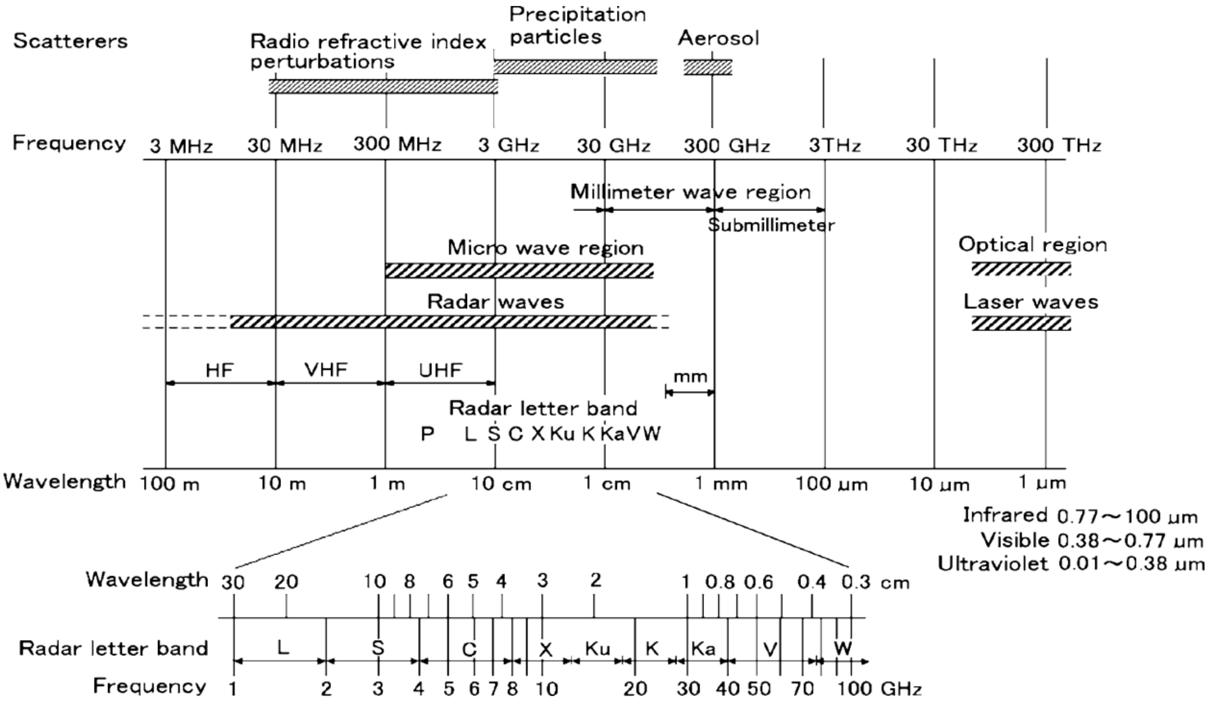

Fig.2.1: The operating frequency band of the individual radars and their adjoining bands (Fukao, 2014)

2.2 Types of Weather and Atmospheric Scattering Mechanisms

The scattering mechanism in radars will depend on the size and material property of the target. Objects like aircraft, ships, raindrops, hail, clouds and refractive index fluctuations scatter the EM waves emitted by the antenna. The power received from the radar will vary depending on the wavelength of the target. Therefore, the selection of radar wavelength will depend on the applications.

The scattering/reflection of electromagnetic energy from the atmosphere results from many physical scattering mechanisms. There are mainly four types of scattering mechanisms: Rayleigh scattering, Mie scattering, Bragg scattering and Fresnel reflection scattering.

2.2.1 Rayleigh Scattering

Weather radars are designed to get backscattering signals from precipitation. This scattering mechanism is mainly due to Rayleigh scattering from the falling drop in the radar pulse volume. This type of scattering is preferred because of the linear relationship between power return and the target size. The drag force caused due to the interaction of rain droplets will cause the liquid water droplet to breakup. This causes the wide distribution of drop size in the radar pulse volume. The scattering of electromagnetic energy depends on the 6^{th} power of drop diameter.

The scattering regime can be determined by the size of the weather target compared to the wavelength of the radar. Rayleigh scattering occurs when the intercepting target is small compared to the wavelength of the radar. This type of scattering is fairly uniform in all directions, and the amount of power reflected increases linearly with increasing size. Therefore, Rayleigh scattering is a very good assumption for all weather targets smaller than 7mm, which includes practically all rain but does not include hail.

2.2.2 Mie scattering

Mie scattering occurs when the intercepting targets become roughly similar in size to the wavelength of the radar beam. This scattering mechanism createsan oscillating relationship between power return and target size (example: Hail).

2.2.3 Bragg Scattering

Refractive index Irregularities will cause electromagnetic waves scattering (Booker and Gordon, 1950). The principal source of the VHF/UHF radar's clear air returns is Bragg or turbulence scattering. Backscattering signals are created by a spatial Fourier component whose wavelength is comparable to one-half of radar wavelengths, according to the theory of radio waves scattering owing to turbulent fluctuations in the refractive index. Hence, the condition for coherent backscatter should satisfy the $\lambda_{min}<\lambda/2<\lambda_{max}$, where λ_{min} and λ_{max} are belong to the turbulence inner (l_0) and outer scale (L_0) sizes. If the systems are sufficiently sensitive, then highest altitude from which backscattered echoes of a particular wavelength may be detected is determined by the l_0 height distribution.

2.2.4 Fresnel Reflection Scattering

The discontinuities in the refractive index in the vertical direction cause this kind of scattering mechanism. Fresnel scattering/ reflection is a process that includes fluctuations of spatial coherence orthogonal to the radar beam. This kind of mechanism is caused mostly by horizontally stratified refractive index variations in the troposphere and stratosphere. Fresnel reflection is a single-layer notion caused by a noticeable discontinuity in the index of refractivity in the vertical beam direction. Fresnel scattering is a multilayer concept that generates specular echoes from volume scattering as a result of a random distribution of refractive index discontinuities in the vertical direction.

2.3 Introduction to Weather Radars

Doppler weather radar (DWR) is important for observations and research in the atmospheric and meteorological sciences for forecasting weather phenomena. ISRO developed radars are operating in various parts of India like SHAR-Sriharkota, NARL-Gadanki, Kochi, Gopalpur, VSSC-Trivandrum, Chennai and Mumbai, which are operated in S, C, and X bands in addition to operational DWRs in Indian Meteorological Department (IMD).

Weather radar plays a key role in observing, analyzing and predicting severe weather events and other meteorological phenomena. The Weather Radar estimates the three base products 1. reflectivity (Z), 2. mean velocity (V) and 3. spectrum width (σ). The Doppler Weather Radars deployed worldwide operate in 'S','C', and 'X' band frequencies.Weather Radars are pulsed radars that provide information about the intensity and internal velocity of hydrometeors in the atmosphere. When the radio wave emitted by the transmitter intercepts any object (here the target is hydrometeor), a part of the incident energy is transmitted through, a part of the energy is scattered in all directions, and the material of the object absorbs a part of the energy.

2.3.1 Polarimetric Doppler Weather Radar

Unlike conventional weather radars, the Polarimetric DWR provides a betterprecipitation estimation over the single polarization radars, as it transmits and receives pulses of microwave energy in horizontal and vertical polarizations. Dual-polarized radar transmits the pulse of microwave energy in horizontal and vertical polarizations. It provides information about horizontal and vertical characteristics of the target that scatter transmitted energy back to the radar and also provide a better sense of the size and shape of the hydrometeor targets detected and also differentiate the targets and non-meteorological targets (birds, insects and ground clutter). From the backscattered energy, we can calculate the six parameters, i.e., Reflectivity (Z), Velocity (V), Spectrum width (SW), Differential Reflectivity (ZDR), Differential phase (PHIDP) and Correlation Coefficient (CC). This type of radar gives meteorologists a better sense of the size and shape of the detected hydrometeor targets and differentiates the targets from non-meteorological targets.

C Band DWR, VSSC, S Band DWR, Kochi (ISRO)

Fig. 2.2: C and S-band Doppler Weather Radar located at VSSC and Kochi

2.3.2 Basic Radar Equation:

The received power depends on the transmitting power, the target's radar cross-section, and the range. Raghavan (2003) provides a more comprehensive derivation.

$$P_r = \frac{P_t A_e G \sigma}{(4\pi)^2 R^4} \qquad (2.4)$$

2.3.3 Weather Radar Equation

A radar antenna is composed of an array of distinct dipole antenna elements or, in most cases, the paraboloid dish over which radio waves pass through a horn waveguide.

The following equation gives the received power from a distribution of meteorological targets, often called the meteorological radar equation (Probert-Jones, 1962).

$$P_r = \frac{\pi^3 P_t G^2 \theta \phi h \sum |K|^2 D_i^6}{1024 \ln 2 \lambda^2 r^2} \qquad (2.5)$$

where $Z = \sum D_i^6$ (2.6)

The relationship between Z and P_r is given by, $Z = \frac{P_r R^2}{C}$ (2.7)

Where P_r is the received power, P_t is the transmitted power, G is the antenna gain, θ is the beamwidth (horizontal), ϕ is the beamwidth (vertical), h is the pulse length, $|K|^2$ is the dielectric factor (for rain 0.93), D_i is the scatterer diameters, λ is the radar wavelength, r is the distance between sample and radar antenna, C is the constant and Z is the reflectivity.

2.4 Block diagram, System Description and Configuration

The overall block diagram of the Doppler weather radar system is given in Fig.2.3. As per the requirement, the system can be configured in different modes of operation based on polarization, namely STAR & Alternate mode of operation. In STAR mode, both the SSPAstransmit & receive simultaneously. For alternate mode of operation, both SSPA transmitsalternatively in H & V polarizations. Two SSPAs are proposed, one for H Mode and the other for V mode. Each SSPA is capable of transmitting 300W. It is having forced cooling arrangement for maintaining the temperature of the SSPA module. The input to SSPA is fed from the TX drive module via a switching module.

The switching module has a phase shifter and SPDT switch. The phase shifter is used to adjust the phase in the transmit path, and the SPDT switch is used during the alternate mode of operation. The input to TX drive module is fed from the up converter module. The upconverter, exciter & RF down converter module forms the RF subsystem. The RF subsystem, along with the digital subsystem (radar computer) & Power distribution, is housed inside a 38U rack. The radar controller provides the command signal for the radar computer.

The radar controller is a GUI that sends commands and experimental specifications for radar operation to the radar computer, and radar signal processor and also collects the status of each subsystem. The RF & digital subsystem is fully synchronized with a high precision, highly stable and low phase noise oven controlled crystal oscillator(OCXO). This OCXO acts as the master clock for generating various other clocks and waveforms for synchronization. DAC module, Exciter module and up converter are used to generate the RF waveform for transmission. The SSPA module amplifies the RF signal to the required power level through a circulator & directional coupler & OMT radiates to the atmosphere. Circulator provides the isolation between the transmitted signal and the received signal. The received signals are processed using four digital receiver channels, two for Horizontal polarization(High and Low gain) and the other two for vertical polarization (High/Low gain). The Compressed I & Q data are sent to the radar signal processor through Ethernet for further base data processing. The system has a provision for validating the noise figure of the receiver chain by injecting the noise source at the coupled port of a 20 dB directional coupler. The BITE signal can be injected via the SPDT switch controlled by the radar computer. The entire power supply for the Radar system is derived from the 3-Phase supply. Fig 2.3 shows the block Diagram of X-Band Polarimetric Doppler Weather Radar upgradation system.

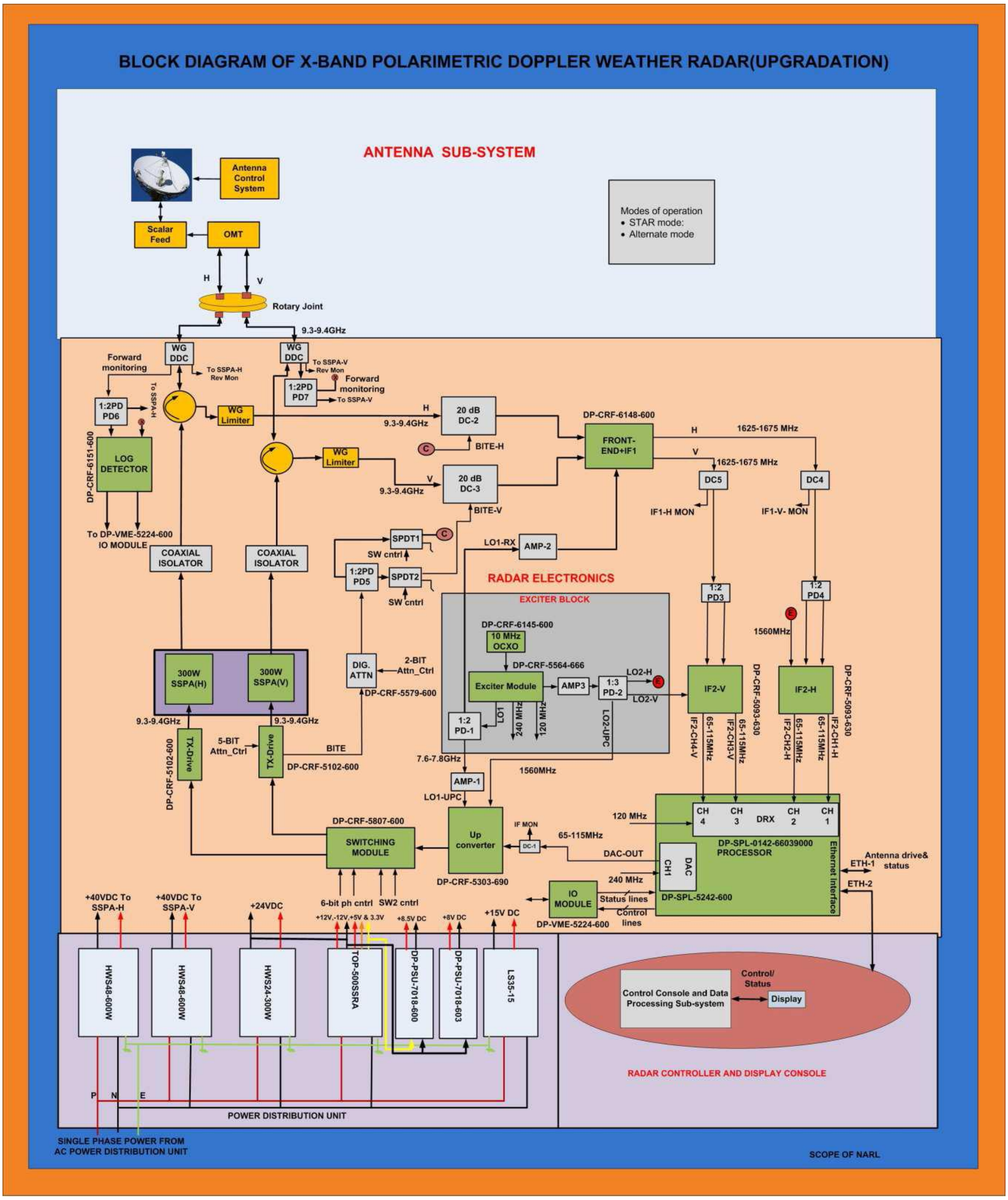

Fig 2.3: Block Diagram of X-Band Polarimetric Doppler Weather Radar upgradation system (Source: Data Pattern)

The functional requirements of the Polarimetric Doppler Weather Radar can be met with the following Subsystems.

1. Antenna Subsystem
2. Transmitter Subsystem

3. RF subsystem
4. Radar Controller
5. PSU Subsystem

2.4.1 Antenna Subsystem

Basically, An antenna operates as a transducer between freespace and guided wave propagation. During transmission, the antenna emits energy in the form of a shaped beam that points in the desired direction into space. During reception, the antenna absorbs energy, which includes an echo signal, and transfers it to the receiver. The parabolic dish and mechanical mounting fittings comprise the Antenna subsystem. The antenna's beam width is roughly 1 degree in the azimuth and elevation planes.

2.4.2 Transmitter Subsystem

The transmitter subsystem is responsible for the generation of high power X band (9.3 to 9.4 GHz) RF signal with required power level and pulse width. The output of the transmitter subsystem is fed to the directional coupler through the isolator & circulator. The directional coupler output is fed to the OMT, where the signal is polarized into different planes (Horizontal &Vertical).

2.4.3 RF Subsystem

RF Subsystem consists of an Exciter module, Switching module, TX drive module, upconvertermodule, RF front module, down converter module & Log detector module. The exciter module is responsible for generating the X-band and L band Local oscillator signals. These LO signals are used for the up-conversion in case of transmission mode and in receiver mode for down-converting the received pulse to IF frequency. The Exciter module also generates the 120MHz ADC sampling clock signal and 240MHz reference clock for the DAC module. The receiver uses the X band LO signal (7.675 to7.725 MHz) for the down-conversion of the X band received signal to the L band (1625 to 1675MHz), then uses an L band LO signal (1560MHz) for the further down conversion to IF frequency.

2.4.4 Radar Controller

The radar controller is a Man Machine Interface (MMI). All the radar experiments are carried out through the radar console. This involves the configuration of experiments and displays of online health status. This entity generates the control signals based on the commands issued by the GUI and distributes them to the other subsystems of radar. The radar controller comprises a processor module, PC & IOT module. The processor module consists of an onboard quad ADC channel and a piggy DAC module. The ADC channel digitizes the IF signal synchronously with the same master reference clock. Thus the digitized data is processed till pulse compression in FPGA and sent to the radar signal processing computer through Ethernet for base product generation.

2.4.5 PSU Subsystem

The AC and DC power distribution throughout the system is carried out by the PSU subsystem of radar. The input to the entire system is a 3ϕ AC supply, which is regulated and supplied to all thesubsystems of radar through the UPS units as a single phase 230VAC supply. The PSU subsystem distributes the DC power to SSPA and other cards from AC-DC converters.

Table 2.1: Specifications of Polarimetric X band DWR located at Gadanki

S.NO	Parameter	Specification
1.	Type	Polarimetric DWR with solid state technology
2.	Operating Frequency	9.3-9.6 GHz with instantaneous BW of 100MHz
3.	Polarization	Alternate transmission of H and V
4.	Volumetric coverage	hemispherical
5.	Observation Time	<8 min
6.	AZ coverage	0 to 360 deg
7.	Elevation	-5 to +95 deg
8.	Beam width	<=1.2 deg
9.	Beam point accuracy	<=0.1 deg
10.	Beam pointing resolution	<=0.01 deg
11.	System Sensitivity	Better than 13 dBZ @ 100 Km
12.	Antenna Side lobe Level	28 dB or better down from the main lobe to 12 deg, 30dB or lower thereafter
13.	Scan strategy	10 Elevations within -5 to 30deg for normal observations.
14.	Scan capability	Upto 6 RPM
15.	Transmit & Receive RMS phase noise	<=0.2 deg
16.	Cross Polar Radiation	Better than 36 dB
17.	Transmitter	H & V channel SSPA's should have minimum 300W peak power output each.
18.	Max capabiliy	150 Km
19.	Minimum range resolution	Better than 75m
20.	Range side lobes	Less than 35 dB
21.	Clutter suppression capability	40 dB typical (time & frequency domain)

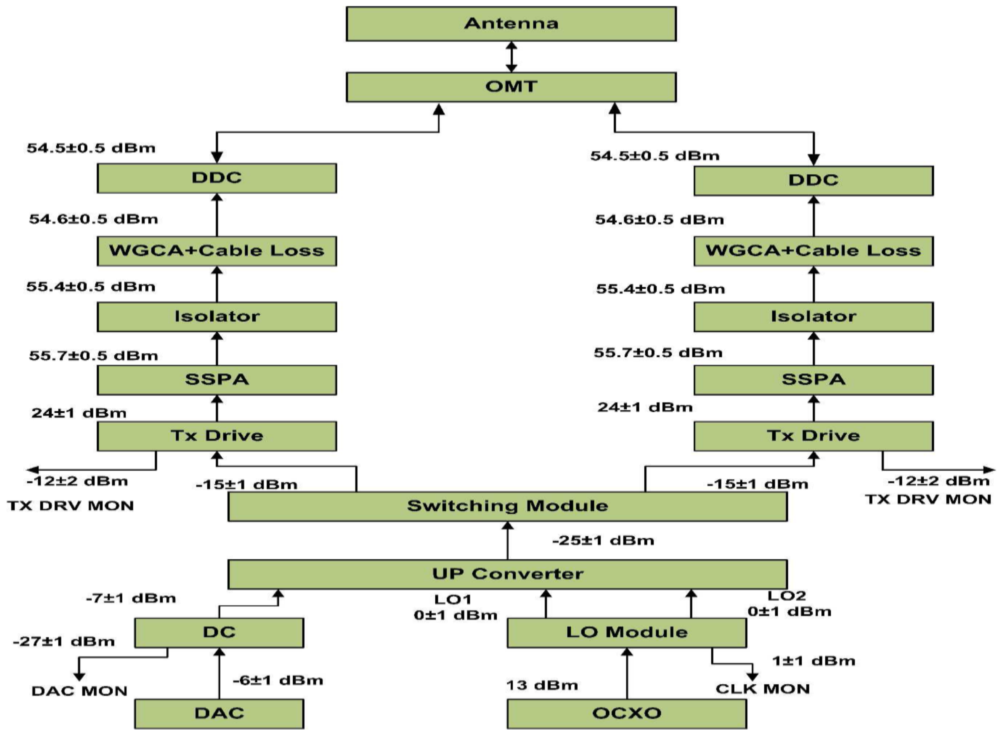

Fig: 2.4: System Transmit Path. (Source: Data Pattern)

2.4.6 Transmit Chain Gain

The transmit chain gain for the system is provided below. The transmit chain consists of OCXO, exciter module, up converter module, switching module and Tx drive module. The output from the coherent signal generator is -6±2 dBm, which is converted to RF signal using an exciter module, up converter module, switching module, Tx drive module & SSPA.

2.4.7 Receiver Chain Gain

The signal level that is received at RF front end is -125dBm to -25dBm. Hence theRF receiver chain is designed in such a way that the power levels at all the RF & IF modules of the receiver are not saturated. For higher power levels, the digital receiver chain is protected from saturation by the limiter at the front end, while the signal input below the noise floor is recovered by the signal processing gain. The power calculation of the RF receiver chain is given below.

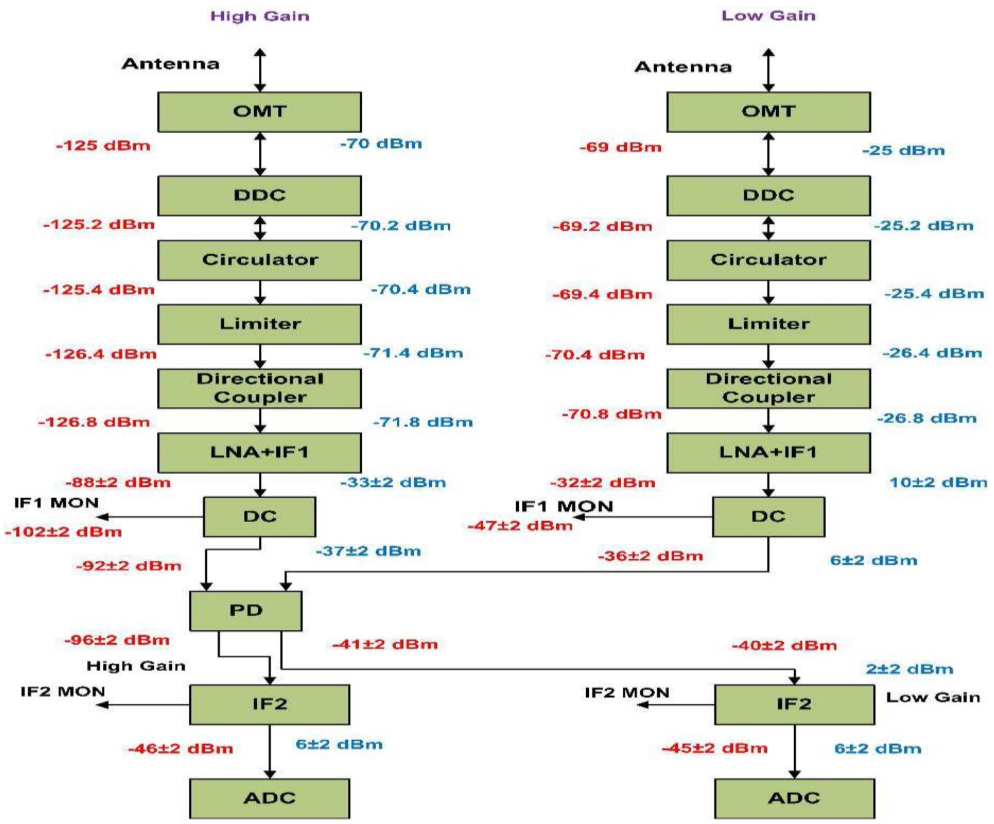

Fig 2.5: System Receive Path. (Source: Data Pattern)

2.5 Noise

Noise is random in nature, which are unwanted signals that are entering into the receiver system. When an object has a physical temperature greater than 0^0 K, the system can emit noise. This noise might come from within or without the receiver system. The major source of external noise for the receiver chain is antenna noise.

The antenna's location is critical for this noise power, which must be estimated appropriately. The antenna noise changes with elevation angle, with lower elevation angles producing more noise than higher height angles. Because of the warm temperature of the Earth, the noise temperature rises at lower elevation angles. The amount of precipitation recorded also has an effect on antenna noise. The noise temperature stays almost constant when looking at clear air, but increases in the presence of warm precipitation. At low to moderate SNR levels, the reflectivity and spectrum width estimators rely on noise power measurements; erroneous noise power measurements may result in biased meteorological variables. To achieve the highest quality radar outputs, it is preferable to compute radar variables after eliminating noise and clutter from the Doppler power spectra. To get a reliable assessment of moments, the noise and clutter in the Doppler power spectrum must be removed.

2.6 Ground Clutter

Weather radars are not only collecting echoes from precipitation but also from the ground features such as mountains, trees, ships, aircraft, buildings and birds. Knowing the characteristics around the radar, like hills, buildings, and towers, allows you to identify ground clutter from the reflectivity display. The existence of ground clutter around the radar is quite strong, and the gain reduction techniques cannot reduce it. There is more like probability to get eliminates precipitation echoes during this process. Vertical side lobes will have strong clutter echoes. Raising the antenna elevation can eliminate most of the clutter, but sometimes the precipitation echoes will also get removed. The ground clutter from the solid targets will be steady, i.e. have a smaller variance than precipitation echoes, which fluctuate considerably, that can be used to reject the ground clutter.

The presence of clutter also will affect the moments estimation and introduce bias on weather radar parameter estimation. The radar environment is so complex that a wide range of sources of clutter are present, e.g. clutter from the ground, insects and birds, radio frequency interferences, radar artifacts, etc. In particular, it has a significant impact on the accuracy of measurements and observation of precipitation areas. To that end, a way of reducing the undesirable echoes must be found. To suppress ground clutter that is centered around 0 m/s, a conventional method like a narrow notch filter will be useful. This method depends on the ground clutter spectrum width. As a result of changes in environment and observation conditions, the spectrum width is therefore variable. There may be overlaps between the radial velocities of rain and ground clutter that result in loss of target signal. Groginsky (1980) introduced a canceller design for removing the clutter. But one of the main limitations of this approach is that there is a chance that the precipitation echoes will be eliminated, which have near zero velocities. Passarelli, 1983 proposed a parametric estimation approach for retrieving spectral moments using autocorrelation function from the clutter contaminated observations. But one of the limitations of this approach is the complexity of the multiple trip echoes that are present. Sachidananda (2000) employed a staggered PRT waveform with negligible distortion to minimize clutter using the matrix approach.

2.6.1 Ground Clutter detection and suppression techniques in DWR

The identification of ground clutter needs an adaptive algorithm that examines time series data. The clutter mitigation decision (CMD) algorithm is one such adaptive technique. The

CMD technique is widely recognized and approved in the weather radar field for integrating three discriminants: clutter phase alignment (CPA), texture of reflectivity (TDBZ), and SPIN to detect the presence of clutter using a fuzzy logic approach. The CPA is calculated using time series data, while the TDBZ and SPIN are calculated using reflectivity over the range.
Clutter identification on a bin-by-bin basis is performed by Clutter Mitigation Decision (CMD) algorithm, and clutter suppression or reduction is performed by the Gaussian Model Adaptive processing (GMAP) algorithm (Siggia, 2004). GMAP algorithm applies filtering only to those bins identified by the CMD. Weather signals and clutter signals look different. This can be approximated by the Gaussian curve.

1. Remove the power from a narrow spike near zero velocity
2. Once power is removed, GMAP attempts to rebuildthe lost weather signal

Weather and clutter signals have different characteristics. A clutter signal has high power, is centered at zero velocity and has a narrow spectrum width. Weather signals (broader ones) are not usually centered at zero velocity, which will have varying power, velocity and spectrum width. GMAP design is that both clutter and weather signals can be well represented by Gaussian curves.

CLEAN-AP (clutter environment analysis using adaptive processing) filter, which uses ground clutter features to automate the identification and mitigation of ground clutter contamination in both Normal propagation (NP) and Anomalous propagation (AP) conditions (Groginsky, 1980). CLEAN-AP outperforms the present CMD/GMAP in terms of ground clutter mitigation (detection and filtering).

SCI, the spectrum clutter identification method (Sachidananda, 2000; Li, 2013; Zhang, 2014), integrates four discriminants to determine the existence of clutter: spectral power distribution, spectral phase variations, spatial texture of echo power, and spectrum width. This approach is designed to identify ground clutter in conjunction with meteorological signals. Even with a low clutter to signal ratio (CSR), this approach can provide biased weather moment estimations.
The Scan-to-scan (Li, 2013) correlation approach, which takes use of the fact that the correlation time of echoes from hydrometeors is often significantly shorter than that of ground objects, is another way for identifying ground clutter.

2.7 Received signal characteristics

Individual scatterers' relative positions in a scattering resolution volume are constantly varied, regardless of whether the density of scattered particles remains constant, for precipitation particles which are randomly distributed and defined by beamwidths from radar antenna and pulse duration. As a result, the scattered signal becomes random and is interpreted as a stochastic signal, with the returned signal phase from one scatterer signal being evenly distributed throughout $[-\pi, \pi]$. Furthermore, the magnitude of scattered signals varies at random. For this reason, an approach based on statistics is necessary to obtain any relevant information from radar signals.

The back scattered signals received from the pulsed Doppler radar can be written as the sum of individual scattered echoes generated by all scatterers in the resolution volume. Papoulis 1965 used the central limit theorem and showed that the real and imaginary components of the back scattered received signals being distributed in Gaussian shape with zero mean, in case of zero bias.

Let us consider V(t) is the received signal, which can be written as

$$V(t)=I(t)+Q(t) \qquad (2.8)$$

The following properties should be met by the in-phase (I(t)) and quadrature-phase components (Q(t)), which provide information about stochastic processes.

- At the same time I and Q components are uncorrelated.
- Mean of I and Q components are Zero.
- Variance of the I and Q components are same.
- I and Q components have the same Autocorrelation function.
- Even though the I and Q components are uncorrelated simultaneously, they are correlated at different times.

Fig.2.6. Shows the statistical distribution of the weather signals observed through time series data. The absolute value and the intensity value of the complex weather signal follows a Rayleigh distribution and exponential distribution, respectively (Bringi, 2001).

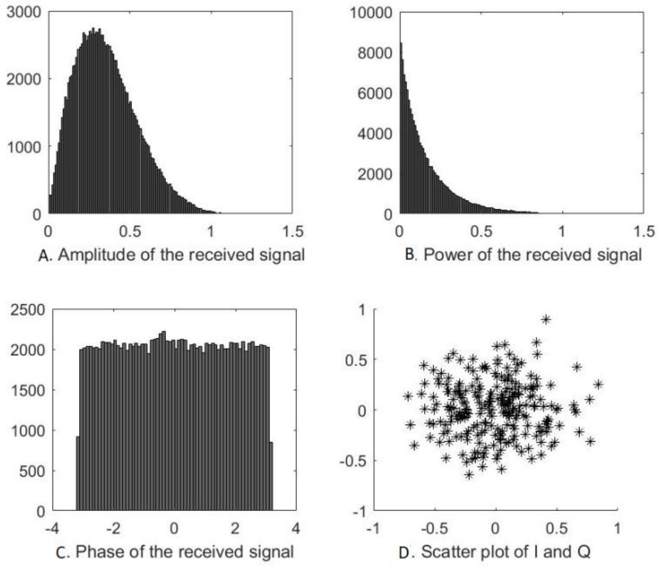

Fig.2.6. Statistical Properties of the received signal

2.8 Signal Processing

Received signals are random variables. A wide range of physical characteristics for scatterers can be estimated by processing a number of received signals statistically. The analysis of the frequency components that compose the radar signal received and which are used for spectral analyses is a fundamental processing technique. In addition, for radar signal processing it is generally necessary to analyse correlation functions as an efficient means of analysing the relationships between more than one signal in a time series. The Fourier transform, which is the most commonly used spectral analysis technique for transforming time series signals into a signal in the frequency domain, is an important tool to do this. However, the processing of time series signal is carried out with autocorrelation function analysis. When one signal is shifted to a certain time with respect to an original signal, it displays the degree of similarity between that signal with its original signal. The cross-correlation function also useful to deduce the time delay between two similar signals.

2.9 Moments Estimation

The first three order moments are very important for weather radar and atmospheric radar to study the dynamics of the weather and atmosphere.Any error generated during moments extraction will lead to an erroneous estimation of the weather and atmospheric parameters. Moments can be extracted by the two methods 1.) Pulse pair processing 2.)Spectral moment estimation.

2.9.1. Pulse pair estimation algorithm (Auto covariance processing)

The pulse pair processing technique is frequently used in weather radars to compute spectral moments. The Doppler frequency can be found by analyzing the autocorrelation between two subsequent pulses. It is a time domain process that uses a complex autocorrelation function of the weather radar signals. This method requires the first few lags to estimatethe first (velocity) and second moment (spectral width). The first moment gives information about velocity, and the second moment provides information about spectrum width. When M pulses are transmitted in a series at intervals of Ts, the autocorrelation can be inferred from the sum.

The first moment velocity will be computed at lag 1 is given by Doviak(1984)

$$\mathrm{R}(1) = \frac{1}{\mathrm{N}}\sum_{\mathrm{n}=0}^{\mathrm{N}-1} \mathrm{V}^*(\mathrm{N})\mathrm{V}(\mathrm{N}+1) \tag{2.9}$$

$$\hat{v} = -\left(\frac{\lambda}{4\pi T_s}\arg\hat{R}(1)\right) \tag{2.10}$$

As the weather signal spectrum is closely correlated with a Gaussian shape, its spectrum width shall usually be estimated from estimates of an autocorrelation coefficient. The spectrum width is given by,

$$\hat{\sigma}_v = \frac{\lambda}{2\pi T_s\sqrt{2}}\left|ln\left(\frac{\hat{S}}{|\hat{R}_1|}\right)\right|^{1/2} sgn\left[ln\left(\frac{\hat{S}}{|\hat{R}_1|}\right)\right] \tag{2.11}$$

By deducting the known noise power from the average of the squares of the magnitudes, the signal power $\hat{S}$ can be calculated.

$$\hat{S} = \frac{1}{M}\sum_{k=0}^{M-1}|V(k)|^2 - N \tag{2.12}$$

V(N) is the N^{th} sample complex voltage. The complex conjugate represented by the asterisk (*) symbol.

Ts is the pulse repetition time

λ is the radar wavelength

Arg indicates the argument of the complex quantity of R, expressed in radians. (Doviak 1984,1993). The term "sgn" is used in this context to identify the negative spectrum width values and permits the assignment of widths to a collection of small values.

The complete theoretical background of signal processing may be found in Bringi (2001), Dovik and Zrnic (1984), and Keeler and Passarelli (1990).

This approach is useful for analyzing the Gaussian spectra, and this method introduces negative and large bias in the case of increased spectrum widths and skewed spectra. A wider spectral width is an indicator of severe weather conditions. The spectrum width also indicates turbulence, which is hazardous to air carriers. This is one of the limitationsof the pulse pair estimation technique, where this is not the case for both Fourier and bispectrum methods. The advantage of the Fourier and Bispectrum methods is the absence of bias introduced by the skewed spectra.

2.9.2. Spectral processing

Direct spectral methods are becoming an attractive means of calculating the mean frequency, due to the introduction of FFT and subsequent reduced circuit costs required for computation.

The estimation of mean Doppler frequency f is given by employing the discrete power spectral density estimate.

$$\hat{f} = \frac{1}{MT_s}\frac{\sum_{k=-M/2}^{M/2} k\hat{S}(k)}{\sum_{k=-M/2}^{M/2}\hat{S}(k)} \qquad (2.13)$$

Where $\hat{S}(k)$ is the k_{th} sample periodogram given by

$$\hat{S}(k) = \left|\frac{1}{MT_s}\sum_{m=0}^{M-1} v(m)e^{-j2\pi km/M}\right|^2 \qquad (2.14)$$

The aforementioned estimations are biased, particularly when an aliasing-induced displacement of a portion of the original Doppler spectrum occurs (Mahapatra 1999). The equation below enhances the Doppler frequency and spectrum width to reduce estimation bias.

We must first estimate the periodogram, which estimates the power spectrum, in order to calculate the mean frequency. Afterward, calculate a rough estimate of the mean frequency, k_m/MT_s, where $k_m(-M/2 \le k_m \le M/2)$ may be the index of the strongest Fourier coefficient. The mean frequency estimate is then provided by,

$$\hat{v} = -\frac{\lambda}{2M}\left\{\frac{k_m}{T_s} + \frac{1}{\hat{P}T_s}\sum_{k_m-M/2}^{k_m+M/2}((k-k_m)\hat{S}[mod_M(k)]\right\} \qquad (2.15)$$

Where $\hat{P}$is the total power in the periodogram, and $mod_M(k)$ is the remainder by dividing k by M.

Spectrum width is given by,

$$\hat{\sigma}_v^2 = \frac{\lambda^2}{4\hat{P}T_s^2}\sum_{k_m-M/2}^{k_m+M/2}\left(\frac{k}{M}+\frac{2\hat{v}T_s}{\lambda}\right)^2 \hat{S}[mod_M(k)] \tag{2.16}$$

In the present study,all three moments were computed in the spectral and time domains. The signal power, Doppler shift, and spectrum width are all represented by the three lower-order moments. The zeroth moment provides a total power of the required weather echo. The Doppler shift is related to the motion of raindrops. The spectrum width is useful for studying the characteristics of turbulence. The time series data obtained is subject to removing the DC bias before pre-processing by taking out the mean value from each sample point. So, any bias that influences the moment estimation will be removed by this method. The radar reflectivity is proportional to the mean power of the received signal. When estimating the mean power, it is necessary to average either the signal power intensity or the logarithmic signal levels. Averaging the signal power provides smaller variance values for the same number of independent samples.The first moment throws some light on the Doppler shift. We can estimate the radial velocity by multiplying the Doppler shift by half of the radar wavelength. The second central moment represents the variance, which measures the velocity dispersion; from the second central moment, we can calculate the spectrum width, which is the square root of the second moment.

2.10 Wind Measurements

Wind is one of the meteorological risks that can have a significant effect on regions with dense people. One of the hazardous properties of abrupt changes in wind speed and/or direction, such as those caused by whirlwinds or microbursts, is wind shear. The horizontal wind field estimation is based on velocity measurements from Doppler weather radars. During field campaigns, a few methods have been used in the past. Short term nowcasting, such as around an airport, could take advantage of a wind field. Weather radars will not give an exact wind vector; they are merely measuring a radial component of the wind vector.

Doppler weather radars not only provide information about precipitation but are also capable of providing wind associated with severe weather phenomena. The mean radial velocity, which depends on range, azimuth, and elevation, is a measurement that the Doppler weather radar provides data on. Weather radars are used to track the dispersion of velocities inside each pulse volume as well as to monitor precipitation in the free atmosphere. The wind shear, turbulence, and precipitation fall speed all affect the Doppler power spectra's structure.

However, meteorological factors like wind and rainfall rate are more interesting than reflectivity or radial velocity. A Doppler radar is typically used to determine the radial speed of hydrometeors. In some circumstances, such as those involving vertically focused beams, these speeds may be significantly different from the radial component of the wind. Targets like water drops have a little mass and are rapidly responsive to horizontal wind forces, allowing them to trace the wind precisely. For radar beams at low elevation angles, the target terminal velocity (steady state vertical velocities relative to the air) produces small bias errors in the radial wind component. High elevation angles must be used to estimate these velocities.

2.10.1 Linear wind model

The horizontal winds and wind vectors at unknown spatial point can be measured using the linear wind model. The model assumes that on the vertical altitude plane z and horizontal distance plane x y, wind speed has a linear variation in all directions. First, it explains how to use a general model for estimating wind vectors from unknown spatial locations. The general model is in three dimensions (3D), in comparison to horizontal wind estimation (2D) Doviak and Zrnic (1984).

The horizontal wind speed and direction are described as,

$$v_h = \sqrt{u^2+v^2} \tag{2.17}$$

Wind direction=atan2(v,u)*(180/pi) (2.18)

$u =$ x- component of v_r in m/s

$v =$y-component of v_r in m/s

$\theta = \frac{3\pi}{2} - arctan\frac{u}{v}$, where v is negative

$= \frac{\pi}{2} - arctan\frac{u}{v}$, where v is positive.

The total amount of the solution errors was reduced via the linear least squares method.

2.10.2 Velocity Azimuth Display (VAD)

The Velocity Azimuth Display (VAD) technique, which was initially presented by Lhermitte and Atlas (1961), can be used to derive the wind field using a single Doppler radar. A single radar can be used to estimate the wind vector using the conventional VAD technique. That technique can be categorized as a frequency-based technique because it relies on a Fourier series to determine the direction and speed of the wind.

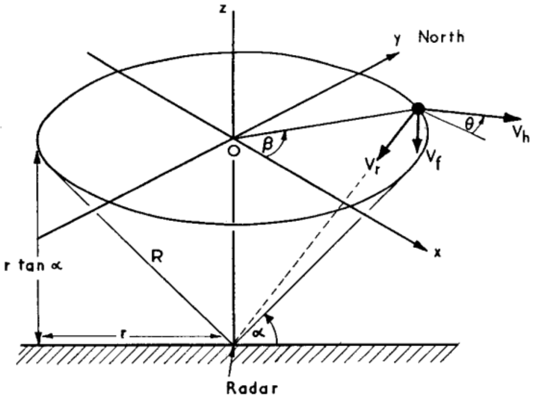

Fig.2.7: Coordinate scheme of VAD method (Browing, 1968).

The conically guided radar beam in the wind field is depicted in the Fig. 2.7, circulating in a circle at a constant range of r.

With the VAD approach, the horizontal wind vector and its horizontal gradients above the radar are precisely measured as an average around the circle at a constant range of a conical PPI scan, or at an elevation of roughly 20^0. This method makes the assumption that the wind field inside this circle is uniform. Unless this assumption is neglected, the estimate for the horizontal wind vector is quite precise and falls within the standard deviation of a Doppler velocity. The VAD method is used to analyze a radar round scan with a Doppler velocity as harmonic data, but it has no impact on the physical frequency. Additionally, it is presumable that the homogenous vertical wind vector w, which symbolizes the fall speed, is present throughout the full circular scan.

In the VAD approach, the zeroth coefficient can be utilized to calculate horizontal wind divergence and the second coefficient to calculate deformation (Doviak, 1984; Browing, 1968). The horizontal wind speed and direction can be calculated using a defined u, v. Data points that are oriented symmetrically in the azimuth direction and round scan velocity data from an elevation angle of a constant are prerequisites for the VAD method.

2.10.3 Volume Velocity Processing

A precise assessment of wind, divergence, and wind field deformations depends on a number of elements, including the volume's size and shape, accurate measurement of wind speed in radial directions, and actual winds linearity, etc. By using a single Doppler radar, the VVP approach is able to acquire wind vectors directly within the volume with a radial speed. The volume's dimensions are range depth of 20–30 km, azimuthal angle width of 30^0–40^0, and elevation angle width of 1^0–2^0. Doviak (1984) provides a comprehensive description of volume velocity processing.

2.11 Wind Profiles

Wind profilers are useful to measure the wind aloft regularly. The radar signals sent by a wind profiler are scattered by dust, molecules, insects and turbulence particles moving with the wind. As those objects move closer or farther away from the wind profiler, the frequency of the returning radar pulse varies. The shift in the return frequency of the radar beam may be used to calculate the wind speed of the air. This allows the vertical wind field to be measured at a certain location continuously. An essential part of understanding weather and climate is to monitor the atmosphere. Thousands of weather observations are made in the world every day. In meteorology, the instruments used for such measurements have evolved into a common instrument.

Weather radar provides precipitation information, whereas atmospheric radars provide wind information. The Indian MST radar is an outstanding tool for monitoring high-resolution atmospheric winds, vertical shear of horizontal winds, and numerous atmospheric turbulence characteristics. One of the important parameters of the atmosphere is the turbulence eddy dissipation rate, which measures the turbulence intensity.

2.11.1 Observation of echoes from Clear Air

Even if there are no phenomena like tornadoes or hail in clear air, which can be seen during severe storms, their structure is strongly influenced by weather events that leads to the storms developments.

2.11.2 Wind profiling

Using radar techniques, wind profiling allows the measurement of winds at a very distant altitude. Such measurements can be made using Doppler weather radars, lidars, and special purpose profiling radars known as profilers.

The Wind Profiler is a Doppler radar that can be used in almost all weather conditions to measure vertically and horizontal wind profiles. The first clear air radar of wind soundings in the troposphere was demonstrated in 1979 (Ecklund et al., 1979), and soon after, a wind profiling network was proposed(Strautch et al., 1984) which operates in the frequency band of VHF and UHF bands (50-900 MHz). A particular frequency band will be selected based on the desired altitude coverage and economy. The eddies create largescale distortions in the Refractive Index, which are less likely to occur in the dissipative range of turbulence. However, the antenna size for lower frequencies should be greater to get higher resolution. 50 MHz, 400 MHz and 900 MHz radars are designed to cover the height up to 20km, 16km and 10km, respectively, depending on the transmitted aperture power product.

2.12 Indian MST radar

MST radar is an excellent tool for studying the different dynamical processes in the atmosphere, operating at 53 MHz (VHF band). It is also useful for studying the prevailing winds, turbulence, atmospheric stabilities and other phenomena. It is also used to study irregularities in the ionosphere results from coherent backscatter above 100 km. This radar can provide atmospheric parameters on a continuous basis. The Indian MST radar currently located at Gadanki (13.5^{0}N, 79.2^{0}E). This radar was commissioned for scientific use in 1993.

Fig.2.8: Indian MST Radar phased antenna array (https://www.narl.gov.in/)

The radar employs a phased antenna array with two orthogonal sets of 1024 three-element Yagi-Uda antennas arrayed in a 32 x 32 matrix across a 130m × 130m area. The radiation pattern is generated by the array with a major lobe of 30 and a gain of 36 dB.

In the matrix grid, the inter-element spacing is 0.7λ, where λ is the wavelength of the radar. The grating lobe free array beam may scan up to angles of 20° from the vertical in the EW and NS planes with a resolution of 1° by utilizing the 8-bit phase shifters. The feeder line's suitable couplers are used to distribute the 32 antennas in line along the subarray through a 3 dB inphase power divider (combiner for reception). The power distribution throughout the array approximates Taylor's modified distribution in both principal directions. By recording the radio source Virgo-A (3C274), phase switching interferometry techniques (Ryle, 1952) were used to analyze the antenna pattern in reception mode.

2.12.1 System Block Diagram

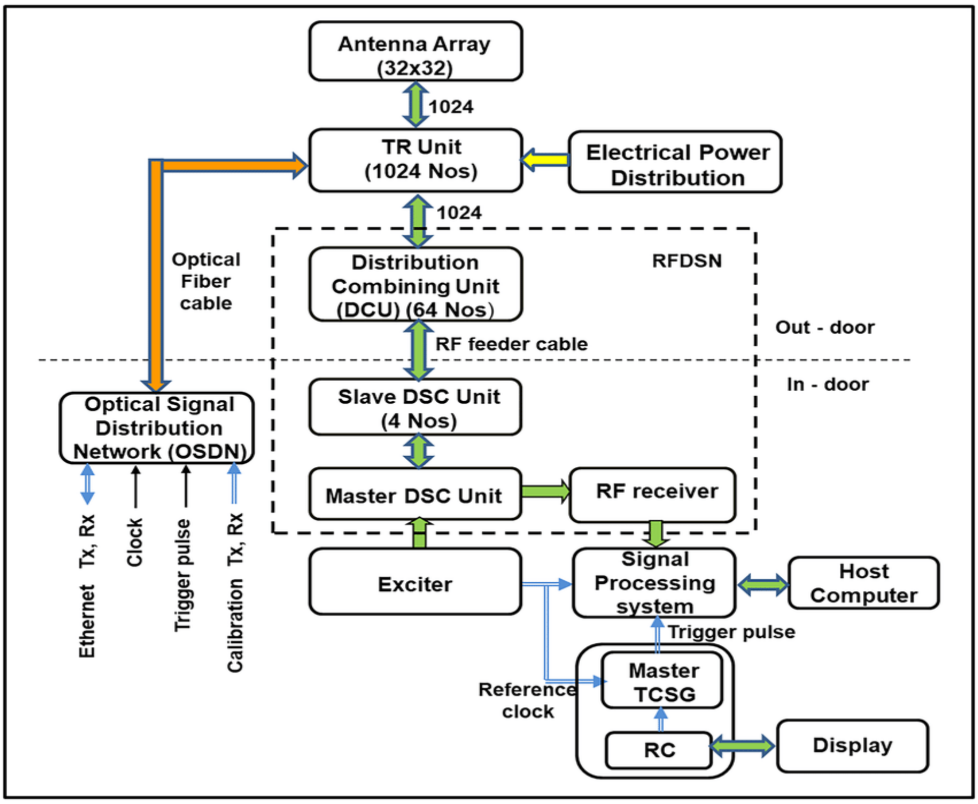

Fig. 2.9: Block diagram of MST radar (Rao, 2020)

Table 2.2: Specifications of MST Radar Gadanki

Parameter	**Value**
Frequency	53MHz
Transmitted peak power (maximum)	2.5MW
Antenna	1024 3-element Yagi
Antenna area	130 × 130 m^2
Beam width (one-way half power)	3^0
Beam direction	13.2^0 off zenith and due north
Receiver gain	120 dB
Receiver bandwidth	1.7 MHz
Receiver dynamic range	70dB
Pulse width	16 µs
Interpulse period	2000 µs
Pulse code	Complementary code
Baud length	1 µs

Coherent integration	4
Incoherent integration	1
Number of FFT points	128

2.13 Wind Profiling Methods

There are mainly two types of wind profiling techniques that exists 1) Doppler Beam Swinging (DBS) and spaced Antenna method (SAM).

2.13.1 Doppler beam swinging method (DBS)

The Doppler beam swinging type of operation for VHF and UHF radar is the most popular. In this technique, a small radar beam pointed vertically up is used by the antenna array. The beam can be switched from zenith angle to off-vertical (north, east, south or west of vertical) directions, $\psi=(90-\boldsymbol{\theta})$, $\boldsymbol{\theta}$, ψ are the elevation and zenith angle. By controlling the signal's relative phase by feeding it to individual antenna elements. Sometimes the observed Doppler shifts may exceed certain windows in ionosphere applications. Therefore, it is desirable to increase the maximum unambiguous Doppler beyond ±125 Hz, and more range gates are also required than the currently available 256 and more than 512 FFT points. More beams are also required for conducting some special experiments. DBS is one of the most used radar techniques to measure wind vectors. In DBS, the entire antenna array will act as transmitter and receiver. The radar beam will be pointed in three or five orthogonal directions to measure the radial velocities. One will be the zenith beam, which will directly measure the radial velocity.

2.13.2 Spaced Antenna method (SA)

Spaced Antenna method was originally used for ionospheric studies. In SA mode, the array has to be divided, and complex signal amplitudes are to be recorded for two-phase centres along East-West and North-South directions. This method provides the horizontal structure of the scattering irregularities. In the SA method, the entire array is divided into segments, where one will act as a transmitter, and all other segments will act as receivers simultaneously. In this method, radar measures the field intensity of scattered signals from refractive index irregularities. The transmitter section will be transmitting vertically into the atmosphere. The refractive index irregularities moving through the radar transmitter beam will create a diffraction pattern in the receiving segments of the radar. The horizontal velocities can be calculated by cross-correlation analysis of signals received from different receivers.

2.14 Signal Processing Techniques

Processing of atmospheric radar signals is nearly as similar to the processing of Doppler weather radars. Clear details have been mentioned in Clothiaux et al. (1994), and Keeler and Passarelli (1990). The returns from a turbulent scatter are quite weak for VHF and UHF radar. Compared to the inter pulse period of the radar, the correlation time of the scattering process is very high. Therefore, the I and Q signal components are integrated separately. Coherent integration refers to this procedure since integration happens in the same phase. As a result, integrating N samples increases the SNR by a factor of N while decreasing the amount of data that has to be processed. Here we obtained the power spectrum using Fast Fourier Transformation (FFT) technique. Due to the random nature of the turbulence, the power spectrum produces statistical fluctuations. The outputs from the radar receivers consist of time series data with Gaussian distribution. The power spectral density (PSD) is the sum of the squares of the spectral components' real and imaginary parts. The spectral density is proportional to the power spectrum's standard deviation. By incoherent integration of successive data, the magnitude of statistical fluctuations can be decreased.

Before estimating the spectral moments, we need to remove the noise from the power spectrum. First, the noise power density value for each range gate is calculated following Hildebrand and Sekhon (1974). The radial velocity is chosen by selecting the largest spectral peak first. The extent of the peak that exceeds the maximum noise is determined. The power of all the points within the extent of the peak above the mean noise is summed. This gives the total backscattered power (zeroth moment). The Doppler (first moment) shift is determined by dividing the sum of the power times frequency of the points within the extent of the peak by the sum of the power points. The spectral width is two times the square root of the second moment about the mean velocity, which is the sum of the power times the frequency squared of the points within the extent of the peak above the mean noise divided by the sum of the power points. These moments (zero, first and second) can be computed using Woodman (1985). The equations for estimating spectral moments are given below in detail.

- The total signal power is given by

$$M_0 = \sum_{i=m}^{n} P_i \quad (2.19)$$

- The Doppler shift is given by

$$M_1 = \frac{1}{M_0}\sum_{i=m}^{n} P_i f_i \tag{2.20}$$

- The variance, is given by

$$M_2 = \frac{1}{M_0}\sum_{i=m}^{n} P_i (f_i - M_i)^2 \tag{2.21}$$

Where m, n are the lower and upper limits of the Doppler bin of the spectral window.

- The Signal-to-Noise Ratio (SNR) in dB is given by

$$\mathrm{SNR} = 10\log\left(\frac{M_0}{N.L}\right) \tag{2.22}$$

N and L represents total number of Doppler bins and mean noise level, respectively.

- The formula for calculating doppler width, which is assumed to be the whole width of the doppler spectrum, is

$$\text{Doppler width} = 2\sqrt{M_2} \tag{2.23}$$

2.15 U V W Estimation

Radial velocity (V_r) at each height can be obtained from Doppler shift (f_d) and it is given by $V_r = -f_d\lambda/2$ ms^{-1}, where λ is the wavelength.

Following the calculation of the radial velocity at various beam positions, the absolute velocities (U, V, W) can be determined. To calculate (U, V, W), at least three non-coplanar beam radial velocity data must be available. If more distinct beam data are provided, the algorithm will yield the best result using the least squares approach.

Case 1: The computation of (U, V, W) from six beam positions is given by.

$$U = \frac{Vr_{East} - Vr_{West}}{2sin\theta} \tag{2.24}$$

$$V = \frac{Vr_{North} - Vr_{South}}{2cos\theta} \tag{2.25}$$

$$W = Vr_{ZenithX \ or \ ZenithY} \tag{2.26}$$

where suffixes represents the different beam directions.

Case 2: The computation of (U, V, W) from one East (West) and one North (South) beam position and one vertical beam position is given by,

$$U = \frac{Vr_{East(West)} - Vr_{ZenithX(ZenithY)} \times cos\theta}{sin\theta} \tag{2.27}$$

$$V = \frac{Vr_{North(South)} - Vr_{ZenithX(ZenithY)} \times cos\theta}{sin\theta} \tag{2.28}$$

W can be calculated in a similar way as mentioned above.

Case 3: The zonal (U) and meridional (V) may be computed as indicated above if all the beams are present except for the vertical beam, and a vertical velocity can be determined as

$$W = \frac{Vr_{East(North)} - Vr_{West(South)}}{2cos\theta} \tag{2.29}$$

2.16 Turbulence studies: An overview

Turbulence generation in the atmosphere is considered as a chaotic phenomenon in meteorology. The study of atmospheric turbulence is having great interest tothe research community and operational forecasters and meteorologists due to its importance in influencing weather changes and atmospheric energy transportation and its dynamics. Higher turbulence in the atmosphere is a hazardous parameter for air carriers; unexpected turbulence can cause severe damage to aircraft and loss of life. Turbulence study has considerable interest to the radar and aircraft engineers for selecting wavelength and aircraft design.

Atmospheric turbulence can be generated by static and dynamic instability related to buoyancy and shear mechanisms. Normally Clear air turbulence (CAT) is associated with shearing, and Convective Turbulence is associated with buoyancy. CAT is the erratic air currents that occur in the cloudless regions that cause violent aircraft buffeting. This turbulence is associated with wind shear commonly occurring at higher altitudes. Convective turbulence is commonly caused by thunderstorms which have strong updrafts and downdrafts. If the atmosphere is more turbulent, nonlinear interactions between eddies results in coupled spectral frequency components in the backscattered signals received, which can be identified by the higher-order spectral analysis.

The conversion of kinetic energy into heat represents the eddy dissipation rate. It is an important parameter to understand the energy flow (which represents how the energy of eddies transfers from larger to smaller scales) within the atmosphere. Methods for estimating ε from VHF radar are discussed by Hocking (1983), Cohn et al. (1995), and Satheesan (2002). Various methods are available for estimating turbulence measurements; however, these approaches require additional in situ data. The spectrum width method is one of the most frequently used techniques for measuring the ε from the spectral moments. The major limitation of this approach is non-turbulent spectral broadening by the instrumental and meteorological sources, which need to be known and accounted. Spectrum width measurements are influenced by five main spectral broadening processes, according to Doviak (1984). Spectral broadening includes beam broadening and wind shear broadening effects. The antenna beam's finite width leads to the beam broadening. Koaly et al. (2002) have examined the narrowing and widening of the doppler spectrum as a result of external contributions. Atlas (1964) observed that the finite beam width, wind shear, and atmospheric turbulence contribute to the spectrum width. Sloss (1968) studied shear broadening in the cross-beam motions of radar scatterers. A series of theoretical works have been reported on estimating ε from the Spectral width calculations (Frisch, 1974; Gossard, 1983; Gossard, 1998; Hocking, 1983; Hocking, 1985; Brewster, 1986; Nastrom and Eaton, 1997; Gage, 1980; Sato, 1985; Narayana et al., 1997; Delage, 1997; Ghosh, 2000; Furumoto, 2001; Narayana Rao et al., 1997; Li, 2016).

The turbulent eddy dissipation rate ε quantifies the energy cascade via inertial subrange turbulence scales. ε is an essential component of turbulence theory. It is also crucial to our knowledge of energy movement throughout the atmosphere since it represents energy conversion into heat. The movements of the smallest turbulent eddies are determined by the fluid's dissipation rate and kinematic viscosity. When there are no sources or sinks of kinetic energy in the inertial subrange, indicates the rate at which energy cascades to smaller eddies until it is converted into heat in the viscous subrange. As a result, although ε may be calculated from the energy flow at any scale within the inertial subrange, its magnitude can be utilized to infer information about turbulence at smaller scales.

2.17 Methods for Estimating Turbulence Energy Dissipation Rate Observed from the Radar

Three methods are available for calculating turbulence energy dissipation rate using radar spectral parameters.1.) Power method, 2.)Variance method and 3.)Spectrumwidth method.

The power and variance method requires additional insitu measurements (such as Brunt Vaisala Frequency (N)) which can be measured from Radiosonde. Spectrum width depends on the radar and meteorological parameters, and it requires spectral broadening correction for the measurement of turbulence energy calculations.

2.17.1 Dissipation Rates from Backscattered Power

The power method uses a measured profile of refractive index structure constant (C_n^2) and requires well calibrated and additional information about atmospheric humidity and stability. The average reflectivity per unit volume η of the target is related to the backscattered power at the radar antenna P by the radar equation (Rogers 1979).

$$P_r = P_t \frac{G^2 \lambda^2 \theta^2 h \eta}{1024 \pi^2 \ln 2\, r^2} \tag{2.30}$$

Where P_t, G, λ, θ, h, r are the radar transmitted power, antenna gain, radar wavelength, radar beamwidth in radians, transmitted pulse width, and range to the target, respectively.

η is correlated with the C_n^2 averaged over the pulse volume $(C_n^2)_{avg}$ for refractive index variations driven by turbulence within the inertial subrange (Tatarskii 1961).

$$\eta = 0.38 (C_n^2)_{avg} \lambda^{-1/3} \tag{2.31}$$

Therefore, the fundamental turbulence measurements of the radar are the volume averaged refractive-index structure constant $(C_n^2)_{avg.}$

Hocking (1985) shows the relation between ε and (C_n^2)to be

$$\varepsilon = \left(\frac{C_n^2 N^2 M^{-2}}{a^2 \alpha' Ri_c}\right)^{3/2} \tag{2.32}$$

$$\text{where } M = -77.6 \times 10^{-6} \frac{PN^2}{Tg} \times \left(1 + 15500 \frac{q}{T} - \frac{15500 q' g}{2N^2 T}\right) \tag{2.33}$$

Where ε and C_n^2 are the turbulence eddy dissipation rate and refractive index structure constant within a turbulence layer. The critical Richardson number Ri_c is taken to be 0.25, and $a^2$and α' are constants approximately equal to 2.8 and 1, respectively. M is the mean vertical gradient of generalized potential refractive index (Ottersten 1969), andN is the Brunt-Vaisala frequency.

Where P, T, g, q, q' is the pressure in millibars, absolute temperature, gravity acceleration, specific humidity, its vertical derivative, respectively. To apply this equation to radar data, it must be modified to account for the fact that C_n^2 is the structure constant within a turbulent layer, but the radar measures a volume average $(C_n^2)_{avg}$that can include turbulent layers of varying strengths and possibly also non-turbulent layers. As a result, the radar volume's fraction F was filled with turbulence must be estimated for use with the radar-determined value ($C_n^2)_{avg.}$ the modified equation is shown below,

$$\varepsilon = \left[1.43(C_n^2)_{avg} N^2 M^{-2} F^{-1}\right]^{3/2} \tag{2.34}$$

2.17.2 Dissipation rates from variance method

The eddy dissipation rate influences the velocity variance driven by turbulence in stably stratified flow, and it is given by

$$\varepsilon \approx C v'^2 \mathrm{N} \tag{2.35}$$

where C is a constant that was calculated empirically by Hocking (1985) and can range from 0.45-0.49. For the radar estimation, previous research typically utilize a value of C 0.45- 0.5. The velocity variance observed by the radar corresponds to the transverse one-dimensional spectrum function for the direction radial from the radar, as shown by various studies. From the radiosonde measurements, the buoyancy frequency N was derived as gdln(θ_s)/dz, where θ_s(z) is the sorted profile of dry potential temperature monotonically.

2.17.3 Turbulence eddy dissipation rate from Spectrum width

The turbulence intensity affects the fluctuating RMS velocity of scatterers in the turbulence medium. Turbulence energy dissipation rate (ε) from spectrum width is given by (Cohn, 1995),

$$\varepsilon = \frac{1}{\delta}\left[\frac{\sigma^2}{1.35\alpha\left(1-\frac{\gamma^2}{15}\right)}\right]^{\frac{3}{2}} \tag{2.36}$$

Pulse length in the radial direction and receiver-matched filtering gives an effective distribution that is approximately Gaussian with a standard deviation of σ_p=150 m. In the transverse direction (beamwidth), the power distribution of radar pulse volume is effective, that is approximately Gaussian with a standard deviation of σ_B=100-300 m depending on range.

$\gamma^2 = 1-(\sigma_p/\sigma_B)^2$, and $\delta = \sigma_B$, when $\sigma_p < \sigma_B$,

$\gamma^2 = 4(1-(\sigma_B/\sigma_p)^2)$, and $\delta = \sigma_p$, when $\sigma_p > \sigma_B$,

σ is the turbulent spectral width, α is a constant value, and lies in the range of 1.53-1.68 (Gossard and Strauch, 1983).

2.18 Spectral broadening corrections

Before estimating the accurate measurements of turbulence eddy dissipation rate, it is important to do the spectrum width corrections. The intensity of turbulence is merely one factor that affects the spectrum's width. The spectrum can be broadened by the non-turbulent fluctuations in the winds and radar characteristics. The two elements, such as beam and shear broadening, can both broaden the spectrum.

2.18.1 Beam broadening

A radar beam with a finite width exhibits beam broadening due to the horizontal wind radial velocities close to the edge. The radar's limited beam width leads to beam broadening. This problem affects all beams. The radar measures the scattering movements of the radar beam in the radial direction. For instance, the radial is not nearly vertical at the edge of a vertical beam, therefore, any scatterers in that area of the pulse volume will contribute radial velocities with both vertical and off-vertical components. A tiny component of the horizontal velocity observed at the beam's edges could still be relevant because horizontal winds are frequently stronger than vertical winds. The Doppler spectrum will be broader because the horizontal component won't have the same radial velocity as the vertical wind. The beamwidth increases with increasing broadening. Beam broadening varies substantially in size

2.18.2 Shear Broadening

Shear broadening is a fluctuation in the mean horizontal wind inside a radar pulse volume. When echo frequencies vary with radial wind velocity, the Doppler spectrum is broadened.

When the mean wind velocity varies across a pulse volume at various ranges, shear broadening happens. Because the horizontal velocity of off-vertical beams has a strong radial component and changes greatly with height. Therefore, shear broadening occurs only in the off-vertical beams. Sloss and Atlas (1968) explored shear broadening for a vertical beam and found that it had a considerable effect on the Doppler spectrum. Vertical velocity changes are often linked with turbulent dynamics, hence shear adjustments are not required for vertical beams.

The observed variance can be written as (Hocking, 1983; Sato, 1985),

$\sigma_{obs}{}^2 = \sigma_{turbulence}{}^2 + \sigma_{shear}{}^2 + \sigma_{beam}{}^2 + \sigma_{wave}{}^2$ (2.37)

$\sigma_{turbulence}{}^2$, $\sigma_{shear}{}^2$, $\sigma_{beam}{}^2$, and $\sigma_{wave}{}^2$ represent the spectral broadening due to turbulence, shear, beam width and atmospheric waves. Since $\sigma_{wave}{}^2$ is so small in comparison to the other correction variables, the final term may be ignored.

$\sigma_{shear}{}^2 = \varphi * |U_h|$ (2.38)

$\sigma_{beam}{}^2 = 0.5 * \left|\frac{\partial U_h}{\partial z}\right| \Delta Z \, sin\theta$ (2.39)

Where U_h is the horizontal wind speed, $\left|\frac{\partial U_h}{\partial z}\right|$ is the vertical shear of horizontal wind respectively with height,

$\boldsymbol{\varphi}$ is the half power half width of the two-way radar beam, and θ is the off-zenith angle.

2.19 Turbulence eddy dissipation rate from the Thorpe method using Radiosonde observations

Thorpe method (Thorpe and Deacon, 1977) uses the potential temperature profile (ө) to estimate the turbulence eddy dissipation rate. The fundamental idea underlying this approach is that the potential temperature rises monotonically with altitude under stable conditions.

Thorpe's technique is affected by instrument noise. We followed Wilson et al. (2010, 2011) method to remove the instrument noise variance observed from the radiosonde data to identify the actual overturns by comparing the range of data samples with the range of normally distributed data of the same data sample size. In the Thorpe method, the potential temperatures were sorted monotonically in increasing order. The vertical displacement of the air parcel's position in the actual profile to that of the same parcel in the sorted profile can be used to determine Thorpe displacements (Td = Z_p-Z_q, where Z_p is the initial position of the air parcel and Z_q is the position of the air parcel after sorting the potential temperature). By using the Root Mean Square (RMS) value, the Thorpe scale can be calculated from the Thorpe displacement.

The relationship between ε and L_t is given by,

$\varepsilon = CL_t{}^2N^3$ (2.40)

Where N=(g/θ)($d\theta$ / dz) is the Brunt Vaisala frequency, C=0.3 is considered for the Indian region (Sunil Kumar, 2015;Nath, 2010; Alappattu, 2010; Muhsin, 2016). Sometimes, C values vary between 0.2 to 1 (Fritts, 2016) depending on stages of turbulence, but till now, exact values have yet to be provided.

2.20. Turbulence length scales

The two most crucial elements of turbulent movements are the turbulent kinetic energy and the interaction among turbulent eddies. There are various subranges that can be used to distinguish the relationship between the scales of turbulent development and decay as well as the energy flow between them. The transition between the energy input, viscous, and inertial subranges characterizes a turbulent flow. The discovery of these transitions can reveal a lot about a turbulent volume and its more significant effects. Size scales are crucial for displaying the size of the eddies. The largest scale of turbulence, referred to as the Inner scale, transition occurs from inertial to viscous subranges at the Taylor Microscale. When talking about turbulence, it's important to consider the inner and buoyancy scale sizes.The inner scale size of turbulence l_0 is given by

l_0=7.4η (2.41)

where$\eta$is the Kolmogorov microscale.

Where $\eta = \left(\frac{v^3}{\varepsilon}\right)^{1/4}$ and $v = \frac{2\times10^{-5}}{\rho}$

Where v, ε and ρ are the kinematic viscosity, turbulence eddy dissipation rate and density of the atmosphere, respectively. Sasi and Sen Gupta's (1986) model was used to determine atmospheric density for the calculation of η and l_0. The buoyancy scale represents the largest eddies that can be obtained from ε and N.

$L_B = \frac{2\pi}{0.62}\varepsilon^{1/2}N^{-3/2}$ (2.42)

Chapter 3

Higher Order Spectral Analysis on Weather Signals

Prelude: This chapter discusses the application of Higher-order spectral estimation techniques to analyse the weather signal to know its statistical distribution and find any deviations from the normality. This chapter also discusses how the Bispectrum performs well under noisy conditions and how this technique significantly removes the Gaussian noise components and improves signal detectability under noisy conditions.

3.1 Introduction to Higher order spectral analysis

Higher-order spectral analysis is the rapidly developing technique in digital signal processing for solving the signal detection and reconstruction problem in radar systems. It is used in various applications of science and engineering to understand the characteristics of unknown signals and the associated process. This technique is very helpful for identifying and estimating signals through a nongaussian process with additive Gaussian noise of unknown covariance. Even though various statistical tools are available for analysing random processes, it utilises first- and second-order statistics for the analysis. Many of the signals in nature are related to nonlinear, non-Gaussian and non-stationary statistics; therefore, these are poorly characterised and indexed by second-order statistics.

The Power spectral density is one of the most frequently used techniques in signal processing of discrete-time signals, whether deterministic or stochastic. The power spectrum is a second-order spectrum, a member of the Higher-Order Spectra. The power spectrum is useful for analysing the Gaussian distribution signals. One of the disadvantages of the power spectrum is that it does not provide any phase relationship between the frequency components. Only the Higher-order spectrum contains such information about deviation from Gaussianity andthe phase of the signals.

HOSA has an important property of being identically zero for the mean Gaussian process. So, it is useful to analyse the weather signals which are contaminated by the Gaussian noise components. Applying Bispectrum on weather estimates is useful to find out whether any deviation is occurring from the normality also. Generally, the noise associated with most observations is Gaussian; the bispectrum process will work in a higher SNR regime, thereby better detecting the signal. Bispectrum estimation is a double Fourier transform of the third-order cumulant function. Most of the signals are always contaminated by noise; applying the bispectrum estimation may help to eliminate the Gaussian noise and characterise the remaining signals for further applications(Giannakis,1990).

The motivation behind the use of higher-order spectral analysis (Nikias, C.L., and J. M. Mendel, 1993; Nikias, C. L., and A. P. Petropulu, 1993; Nikias C. L., and M. R. Raghuveer, 1987; Rosenblatt,1965) in signal processing is 1) It suppresses the additive Gaussian noise, 2) it can reconstruct the non-minimum phase signals, 3) It extracts the information about deviation from Gaussianity (Sadler,1994) 4) It is useful for characterisation and detection of nonlinearities in time series (Kim,1949; Nikias, C. L., and A. P. Petropulu,1993). In the first motivation, all cumulant spectra of order greater than two are identically zero for the Gaussian process. Third-order cumulant spectra will suppress and eliminate any Gaussian noise that is additive to the received signal. Therefore, certain advantages exist in detecting and estimating signal parameters from cumulant spectra.

In the second motivation, the Higher-order spectrum preserves the true phase of the signals. Second-order statistics are useful for modelling the time series data in signal processing. Because these are results from least squares optimisation criteria, using the autocorrelation function will suppress the phase information of the signal. The phase reconstruction can only be possible in the autocorrelation domain if the signal is the minimum phase. Higher order spectrum can reconstruct the non-minimum phase signal due to the ability of polyspectra to preserve the magnitude and phase information. In the case of the third motivation, non-Gaussian signals have nonzero higher-order spectra. The fourth motivation is based on the analysis of nonlinearities present in a system operating at random input. Higher order spectra will help in identifying and characterising the nonlinearity in a system from its output data (Rao and Gabr, 1980; Nikias and Petropulu, 1993; Hasselemann et al., 1963; Barnell et al., 1971)

Therefore, HOSA technique is widely used in various applications such as oceanography (Cherneva, 2004; Hara,2003; Hasslemann, 1963), bio-medicine (Barnell, 1971; Coelli,2019; Kotriwar, 2018; Pradhan,2012), speech signal processing (Nasrolahzadeh,2018), fluid mechanics(Imran,2018; Van Atta,1976) (to study the nonlinearity and non-Gaussianity processes) (Birkelund, 2009;Kim, 1979; Peter,2018; Pires, 2021) and Radar signal processing (Totsky, 2018).

Here, a Higher order spectrum has been considered for analysing weather signals, which is useful to find out the deviation from the Gaussianity and suppress the Gaussian noise components thereby, improve the spectral estimations, mainly first and second-order moments. The pulse pair estimator will be biased for meteorological targets with high spectrum widths (Doviak, 1984). The higher-order spectral analysis provides an improved velocity and spectrum width estimation. In conventional methods, noise level estimation is required before calculating moments. In contrast, higher-order spectra do not require noise level computations because the third-order spectrum will become identically zero for Gaussian components. This paper mainly focuses on how Bispectrum performs under noise-varying conditions and improvement in the spectral moments, especially first and second-order moments since noise is considered white Gaussian.

The definition, properties, and higher-order statistics computation for real signals, namely cumulants and moments, as well as higher-order spectra of them are clearly explained in (Nikias, C.L., and J. M. Mendel, 1993; Nikias, C. L., and A. P. Petropulu, 1993; Nikias C. L., and M. R. Raghuveer, 1987; Rosenblatt,1965).

3.1.1 Cumulants and Moments

For a Gaussian process, cumulant spectra order greater than or equal to two are equal to zero, because cumulants are strongly associated with moments. Non-Gaussian cumulant spectra thus give a measure of non-Gaussianity. Moments or cumulants are frequently used to define HOSA (Nikias, C.L., and J. M. Mendel, 1993). For stochastic signals, cumulants are preferable, whereas moments are preferable for deterministic signals. Lower-order statistics are contained in Moments. Cumulants may be calculated in the same way as moments can. The natural logarithm of the moment generating function yields the cumulant generating function. When Gaussian noise components contaminate signals, cumulative-based approaches increase the signal-to-noise ratio (SNR) and detectability.

The bispectrum technique is generally a complex function. Cumulant spectra are more effective than moment spectra, particularly when processing random signals. It is known that complex signals do not have the same symmetric properties as real signals. For complex-valued signals, the position of the complex conjugate operator in the third-order cumulant function determines the symmetry property of the Bispectrum (Brillinger, 1967). There are 2n different ways to define the nth order moment functions of a complex signal, depending depending on where the complex conjugate operators are positioned. As a result, each moment spectrum with various conjugation patterns has its own principal domain and symmetries. This is clearly described in literatures (Jouny,1992; Nikias, C. L., and A. P. Petropulu,1993).

3.1.2 Higher order spectral analysis on complex signals

Let us consider x(n), x(n+p) and x(n+q) as complex data sample points with zero mean.

The autocorrelation function of complex data is given as

$r(p)=\Sigma\ x^*(n)\ x(n+p)$ (3.1)

The equivalent power spectrum is given by,

$S(\omega)=\Sigma\ r(p)\exp(-j\omega p)$ (3.2)

The third-order cumulant of complex data is defined as,

Case1: $c(p,q)=\Sigma\ x^*(n)x(n+p)x(n+q)$ (3.3)

Bispectrum is the double Fourier transform of third-order cumulants. Hence, the Bispectrum is defined as,

$B(f_1,f_2)=\sum\sum c(p,q)\exp(-j2\pi f_1 p - j2\pi f_2 q)$ (3.4)

Where c(p,q) is the third order cumulant of complex data, is defined as,

Case1: $c(p,q)=\Sigma\ x^*(n)\ x(n+p)\ x(n+q)$ (3.5)

$B(f_1,f_2)=\sum\sum\sum x^*(n)x(n+p)x(n+q)\exp(-j2\pi f_1 p)\exp(-j2\pi f_2 q)$

$=\sum\sum\sum x^*(n)x(k)x(r)\exp(-j2\pi f_1(k-n))\exp(-j2\pi f_2(r-n))$

(where, n+p=k and n+q=r)

$=\sum\sum\sum x^*(n)\exp(j(2\pi f_1 + 2\pi f_2)n)x(k)\exp(-j2\pi f_1 k)x(r)\exp(-j2\pi f_2 r)$

$=X^*(f_1 + f_2)X(f_2)X(f_1)$

$=X^*(f_3)X(f_2)X(f_1)$ (3.6)

where, $f_3 = f_1 + f_2$

Case2: $c(p,q) = \Sigma\, x(n)\, x^*(n+p)\, x(n+q)$ (3.7)

$$B(f_1,f_2) = \sum\sum\sum x(n)x^*(n+p)x(n+q)\exp(-j2\pi f_1 p)\exp(-j2\pi f_2 q)$$

$$= \sum\sum\sum x(n)x^*(k)x(r)\exp(-j2\pi f_1(k-n))\exp(-j2\pi f_2(r-n))$$

$$= \sum\sum\sum x^*(k)\exp(-j2\pi f_1 k)x(n)\exp(j(2\pi f_1 + 2\pi f_2)n)x(r)\exp(-j2\pi f_2 r)$$

$$= X^*(-f_1)\, X(-f_1-f_2)\, X(f_2) \qquad (3.8)$$

The definition of cumulants is based on the Expectation operations and an infinite length of data, but in practice, we only deal with a finite length of data. Therefore cumulants can only be approximated. The cumulants and power spectra can be calculated by using two methods.1) Indirect method 2) Direct method. The direct method is being followed in the present (Nikias, C.L., and J. M. Mendel,1993; Nikias C. L., and M. R. Raghuveer,1987) analysis.

Bispectrum can be obtained by applying a Fourier transform to the third-order cumulant function, and it is a 3-dimensional (3D) complex-valued function having both magnitude and phase. Therefore Bispectrum can be plotted against frequency variables f_1 and f_2 in a 3D plot. The interaction between frequency components f_1 and f_2 represents the nonlinear interactions in signals. The bispectrum function in discrete form is given by,

$$B(f_1,f_2) = X(f_1)\, X(f_2)\, X^*(f_1+f_2) \qquad (3.9)$$

$B(f_1,f_2) = |B(f_1,f_2)|\ \exp(j\theta(f_1,f_2))$, where f_1, f_2 are frequency indexes. X denotes the Fourier transform of the signal, and X* is its conjugate. The Bispectrum in the above equation (3.9) explain the measure of the level of three-wave interactions observed in the frequencies of f_1, f_2 and f_1+f_2.

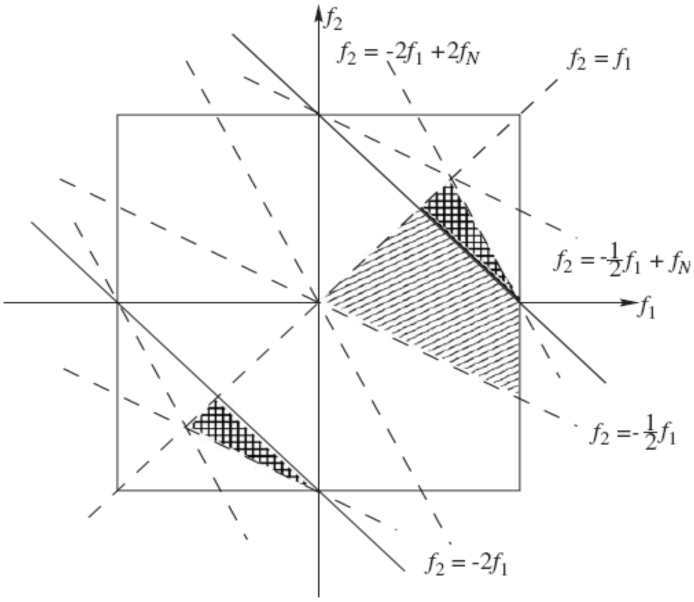

Fig.3.1: Symmetric properties of Bispectrum for complex valued signals (Peter J. S, 2006)

Therefore, knowledge of the bispectrum in this triangle region is sufficient to describe its whole bispectrum. Fig.3.1 shows the symmentric properties of bispectrum for complex signals.

Table 3.1: Placement of the Complex Conjugate in the Third Order Cumulant and its Corresponding Bispectrum

Third order cumulants	Bispectrum
Σx*(n)x(n+p)x(n+q)	$X^*(f_3)X(f_2)X(f_1)$
Σx(n)x*(n+p)x(n+q)	$X^*(-f_1)X(f_2)\,X(-f_1-f_2)$
Σx(n) x(n+p) x*(n+q)	$X(f_1)X^*(-f_2)X(-f_1-f_2)$
Σx(n) x*(n+p) x*(n+q)	$X^*(-f_1)\,X^*(-f_2)X(-f_1-f_2)$
Σx*(n) x*(n+p) x(n+q)	$X^*(-f_1)\,X(f_2)X^*(f_1+f_2)$
Σx*(n) x(n+p) x*(n+q)	$X(f_1)\,X^*(-f_2)X^*(f_1+f_2)$

3.2 Bispectrum algorithm

3.2.1 Direct Method

This paper followed the Direct method for estimating Bispectrum based on DFT coefficients (Anandan et al., 2001; Bartlet, 1984; Nikias, C.L., and J. M. Mendel,1993; Nikias C. L., and M. R. Raghuveer,1987).

Let {X(1),X(2),…….,X(N)} be the available data set of observations for the bispectrum estimation.

Let fs be the sampling frequency and

Δ_0=fs/N_0be the required spacing between frequency samples in the bispectrum domain

N_0 is the total number of frequency samples.

The following are the steps to be followed:

Segment the data into K segments of M samples each, i.e., N = KM.

Subtract the mean value of each segment. We can do zero padding to get the required series length for FFT analysis.

Based on M points, compute the Discrete Fourier Transform (DFT) coefficients Y_i (λ) of each segment.

$$Y_i(\lambda)=\frac{1}{M}\sum X_i(k)\, e^{\frac{(-j2\pi k\lambda)}{M}}, \quad i=1, 2,...., K \qquad (3.10)$$

Bispectrum estimated based on the DFT coefficients.

$$c_i(\lambda_1,\lambda_2)=\frac{\sum\sum Y_i(\lambda_1+k_1)Y_i(\lambda_2+k_2)Y_i^*(\lambda_1+\lambda_2+k_1+k_2)}{\Delta_0^2} \qquad (3.11)$$

For the special case where no averaging is performed in the bispectrum domain, M_1 = 1, L_1 = 0, and therefore:

$$c_i(\lambda_1,\lambda_2)=\frac{Y_i(\lambda_1)Y_i(\lambda_2)Y_i^*(\lambda_1+\lambda_2)}{\Delta_0^2} \qquad (3.12)$$

Obtain the Bispectrum by averaging all the K segments. i.e.,

$$B(\omega_1,\omega_2)=\frac{1}{K}\sum c_i(\lambda_1,\lambda_2) \qquad (3.13)$$

Where ω_1= ($2\pi f_s/N_0$) (λ_1) and ω_2=($2\pi f_s/N_0$) (λ_2)

The direct method produces unbiased bispectrum estimates in cases where N is large. The variance of the estimates can be reduced by increasing the number of records and the record size.

3.2.2 Indirect Method

Let {X(1),X(2),…….,X(N)} be the available data set of observations for the bispectrum estimation.

1. Segment the data into K records of M samples each, i.e., N=KM.
2. Subtract the average value of each record.
3. Estimate the third-order cumulant sequence of each segment.

   $r'(m.n) = \frac{1}{M}\sum_{p=s_1}^{s_2} x^i(p)x^i(p+m)x'(p+n)$ (3.14)

   Where i=1,2,…,K

   S1=max(0,-m,-n)

   S2=min(M-1,M-1-m,M-1-n).

4. Average $r^i(m,n)$ over all segments
5. $c_3^x(m,n) = \frac{1}{M}\sum_{i=1}^{K} r^i(m,n)$ (3.15)
6. Now, generate the bispectrum estimate
7. $C_3^x = \sum_{m=-L}\sum_{n=-L} c_3^x(m,n)W(m,n)\exp\{-j(\omega_1 m + \omega_2 n)\}$ (3.16)

   where L<M-1. W(m,n) is a two-dimensional window function.

3.3 Power spectrum computation from Bispectrum

The power spectrum can be reconstructed from Bispectrum (Anandan et al., 2001)

$B(\omega_1,\omega_2)=X(\omega_1)X(\omega_2)X^*(\omega_1+\omega_2)$ (3.17)

For given samples, $B(p,q)=B((2\pi/N)p, (2\pi/N)q)$; p, q=0,1,….N-1 of the bispectrum $B(\omega_1,\omega_2)$ of a sequence x(n) of length N. Bispectrum of the samples can be computed as

$|B(p,q)|=|X(p)||X(q)||X(p+q)|$ (3.18)

$|X(k)|$ can be obtained from the samples of $|B(p,q)|$ by using the Bispectrum samples by making one of the axes equal to zero. i.e. $\omega_1=0$ or $\omega_2=0$ this can be done by substituting either $q = 0$ or $p = 0$,

When $p = 0$,

$$|B(0,q)| = |X(0)|\,|X(q)|\,|X(q)|$$

$$= |X(0)|\,|X(q)|^2 \quad \text{(Or)}$$

$$|X(l)|^2 = \frac{|B(0,q)|}{|X(0)|} \tag{3.19}$$

Where, $|X(0)|=|B(0,0)|^{1/3}$

Equation (3.19) is the equivalent power spectrum computed via Bispectrum estimation. Once the power spectrum is obtained from the Bispectrum, moment calculation will be the same as in equations (2.15) and (2.16).

3.4. Simulation Analysis and Verifications

The weather radar real time series data does not always match the Gaussian spectral model exactly. However, for simulating time series data, the model is still a standard method for testing signal processing algorithms (Curtis, 2018).

A simulation study of weather signals has been carried out to investigate any deviation from the Gaussian shape observed from the power spectrum and also to study how Bispectrum performs well under noise-varying conditions. Simulation has been performed with the realisation of different weather signals having different properties in terms of SNR, mean velocity and spectrum width. A Gaussian Mixture Model (GMM) of Doppler power spectra(Dong, 2022) has been considered for this analysis and generated the time series of complex-valued weather signals using the approach of Zrnic,1975, with different SNR conditions. This analysis has been performed clutter free regions because clutter may produce non-gaussian spectra.

The weather signal's power spectrum can be modelled using Gaussian Mixture Model (GMM) (Dong, 2022; Yu et al., 2009).

$$S(f)=\sum_{k=1}^{K} \frac{w_k P}{\sigma_{fk} sqrt(2*pi)}\, exp\left[-\frac{(f-f_k)^2}{2{\sigma_{fk}}^2}\right] \tag{3.20}$$

Where P is the total signal power, K is the number gaussian shaped spectra contained in a power spectrum,w_k are the weighting coefficients ($0<w_k<1,\sum_{k=1}^{K} w_k = 1$), σ_{fk} and f_k are the spectrum width and mean velocity.

In this section, a known dual Gaussian power spectrum model in each realisation is simulated with a 1000 realisation process and simulated weather echoes by the procedure (Dong, 2022; Zrnic,1975), which are used as the input of the proposed method. Using Bispectrum and Fourier methods, we obtained the velocity and spectrum width and calculated Root Mean Square Error (RMSE) to verify the advantage of the proposed method. Finally, we applied bispectral analysis on the real-time series obtained from the Doppler weather radar for verification.

The values SNR is 0, 10, 20, 30, and 40dB considered for every 200 realisations, respectively. Here, four realisations with different SNRs and the theoretical values of skewness and kurtosis were obtained from the Gaussian mixture model. The simulation parameters used are listed in Table 3.2. Four realisations are selected for different SNRs, shown in Fig.3.2. It can be observed that the power spectrum shape deviates from the Gaussianity in all four realisations. Black lines show the simulated spectra (true spectra), and spectra reconstructed from the Fourier and Bispectrum are shown by magenta and blue colour lines, respectively. It can be seen that the Bispectrum can better characterise the simulated spectra, and the noise fluctuations are also suppressed compared to spectra reconstructed from the Fourier approach. It can also be observed that the Bispectrum method performs much better than the Fourier method. The skewness and kurtosis with different SNRs of four realisations are listed in Table 3.3.

Table 3.2: GMM Power spectrum model Parameters

No	wk	v(m/s)	$\boldsymbol{\sigma}_v$(m/s)
1	0.8	3.15	1.5
2	0.2	-10 to 10	1 to 5

Table 3.3: Spectrum width, Skewness and Kurtosis of four realisations with different SNR

No	SNR(dB)	σ_v(m/s)	Sk	Theoretical Sk	Kt	Theoretical Kt
1	10	3.53	B:-0.72 F:-0.92	-0.69	B:2.08 F:2.33	1.93
2	20	4.75	B:-1.47 F:-1.37	-1.50	B:3.75 F:3.50	3.78
3	30	3.28	B:0.42 F:0.71	0.55	B:1.67 F:1.98	1.76
4	40	4.9	B:-0.88 F:-1.07	-0.83	B:2.02 F:2.69	2.13

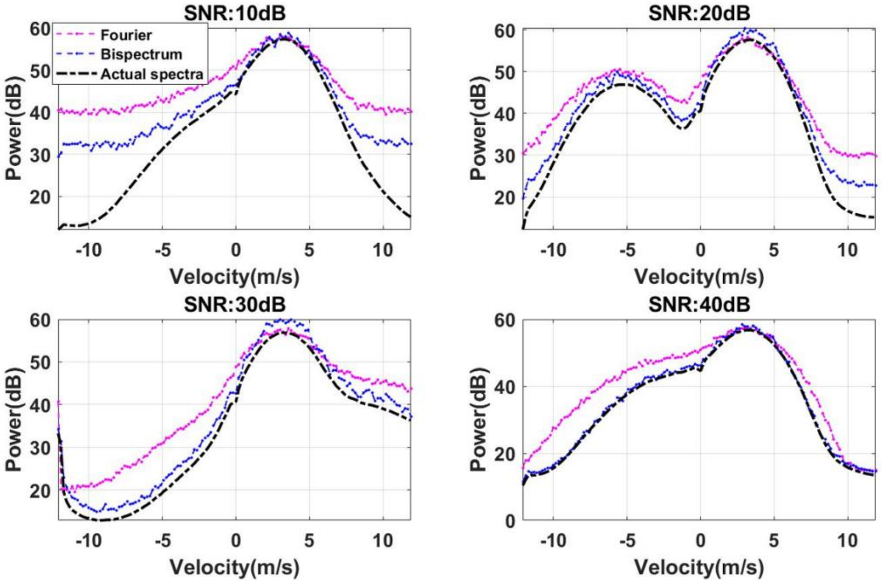

Fig.3.2: Simulated Power spectrum reconstructed from Fourier and Bispectrum approach with different SNR.

The number of samples is 128, and the maximum unambiguous velocity is 12m/s with a number of realisations of R=1000. The root mean square error (RMSE) values are calculated to verify the advantage of the bispectrum approach compared to the Fourier method. The RMSE is calculated from the actual spectra and reconstructed spectra obtained from both the

Fourier and Bispectrum techniques, as shown in Fig. 3.3. It can be seen that the Bispectrum performance is better than the conventional Fourier method under noisy conditions.

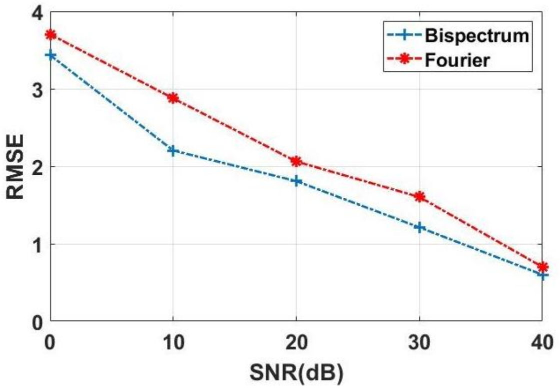

Fig. 3.3: RMSE from both Fourier and Bispectrum methods.

3.5. Experimental results of weather radar observation

The dual Gaussian and skewed piecewise Gaussian model fitting algorithms (Lee, 2010)are very useful when the Doppler power spectrum deviates from the Gaussianity. It is observed that many Doppler spectra deviate from the Gaussianity, which is observed from X-band Doppler weather radar on 17th October 2019. To check the deviations, the dual Gaussian model (Gaussian Mixture Model) is used to fit the single-peaked and double-peaked from the observed spectra, respectively, of different range bins, as shown in Fig 3.4.

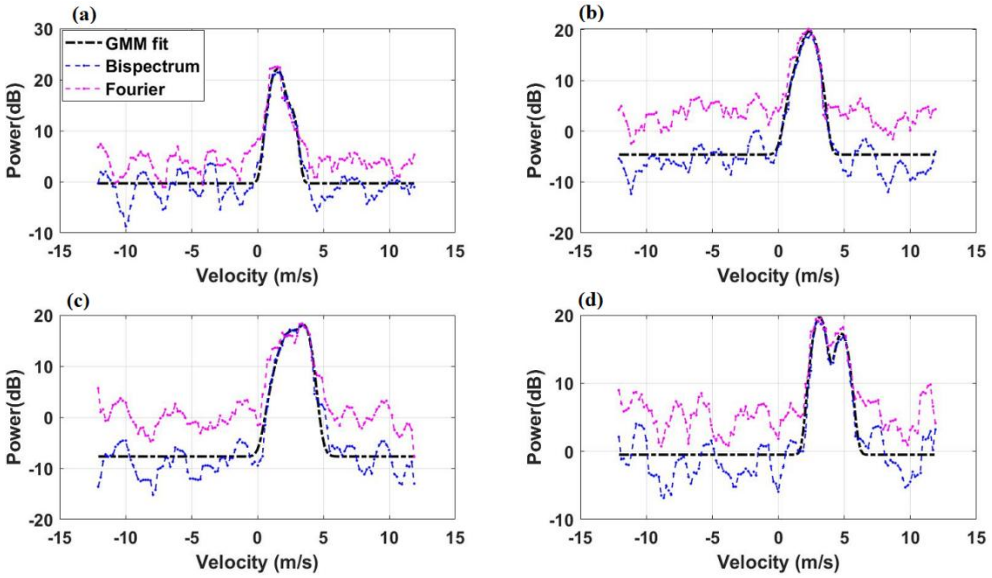

Fig. 3. 4: Gaussian Mixture Model(GMM) fit the observed spectra obtained from X-band DWR on 17th October 2019, corresponding range gates ofa) 60, b) 71, c) 175 and, d) 354 azimuth: 70, respectively.

To obtain the Initial guess parameters followed the Yu et al., 2009 approach to fit the GMM to the observed spectrum. Fig.3.4(a)-(d) shows the Fitting of the GMM curve to an estimated power spectrum obtained from the Bispectrum for 60, 71, 175, and 354 range gates, respectively (in logarithmic scale). On a logarithmic scale, the Gaussian shape corresponds to a parabola. It can be observed from Fig 3.4 that the observed spectra deviated from the Gaussian spectral shape.

3.6 Weather Data Analysis

Bispectral analysis was performed on complex time series data obtained from an X-band polarimetric Doppler weather radar at Gadanki (13.5°N, 79.2°E) with a range resolution of 150m and a sampling period of 1500 Hz. Backscattered signals are preserved as in-phase and quadrature-phase components. To get a Doppler power spectrum, complex time series data is treated for both Fourier and bispectral analysis. A total of 128 samples were processed using a standard algorithm for deriving the power spectrum and bispectrum computations by the direct method.

It is observed from the bispectral analysis the shape of the precipitation echo slightly deviates from the Gaussianity in the power spectrum. Therefore, slight deviations can be expected in weather signals, which need not follow the exact Gaussian shape. Higher-order spectral analysis has been carried out in every range bin to find the deviation from Gaussianity from the observed Doppler power spectra. Since noise has Gaussian characteristics, therefore the magnitude of the Bispectrum is very less (it should not be exactly zero but identically zero). Thereby, it suppresses the noise level very well from the spectra.

The bispectrum $B(\omega_1,\omega_2)$ is a two-dimensional function. The signal corresponding to $B(\omega_1,0)$ retains the information about the true signal.

3.7. Results and Discussions

The direct method of bispectrum estimation algorithm was applied to complex time series data of polarimetric X-band DWR. The data corresponds to a single azimuth orientation of the antenna with a particular elevation of 10 degrees observed on 17th October 2019. The results obtained from the Fourier method, Pulse pair method and bispectrum analysis are presented to show how the bispectrum analysis has performed over the conventional methods.

Fig.3.5 shows the Doppler power spectrum obtained by using the Fourier method up to a range of 81.45 km. It is observed that both the ground clutter and the weather signals are present in the spectrum. Most of the signals contain ground clutter due to non-moving targets like trees and hills, which are typically stationary. We can observe from the Fig. 3.5 that zero-velocity signals in the ranges from 0 -10 km have the typical characteristics of ground clutter (i.e., narrow spectrum with near-zero velocity), whereas the signals in the ranges from 5 – 60 km have the characteristics of weather signals (i.e., modest spectrum width and velocities representative of their radial motion). Fig.3.6(a) shows the power spectrum obtained by both Fourier and bispectrum techniques. It can be observed that the bispectral analysis significantly filters the noise components that are Gaussian in nature (white noise in characteristic) and improves the signal detectability compared to the conventional Fourier method. As can be seen from Fig.3.6(a), significant additive components of noise are also removed from the weather signal as the spectrum from the bispectral analysis shows reduced fluctuations in the weaker returns of the weather signals. Fig.3.6(b) and Fig.3.6(c) clearly show that the shape of the precipitation Doppler spectra deviates from Gaussianity. Therefore, it is evident that applying the bispectrum method significantly reduces the noise components. The spectral components that remain after the application of the Bispectrum are the skewed Doppler power spectrum.

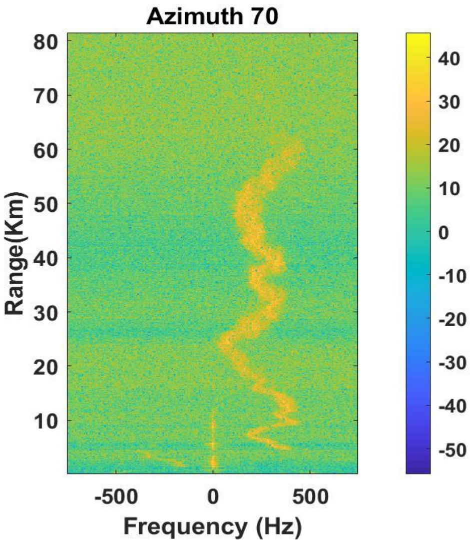

Fig. 3.5: Doppler Power spectrum estimated through conventional method (FFT) of Azimuth 70 and 10 degree elevation observed on 17th October 2019.

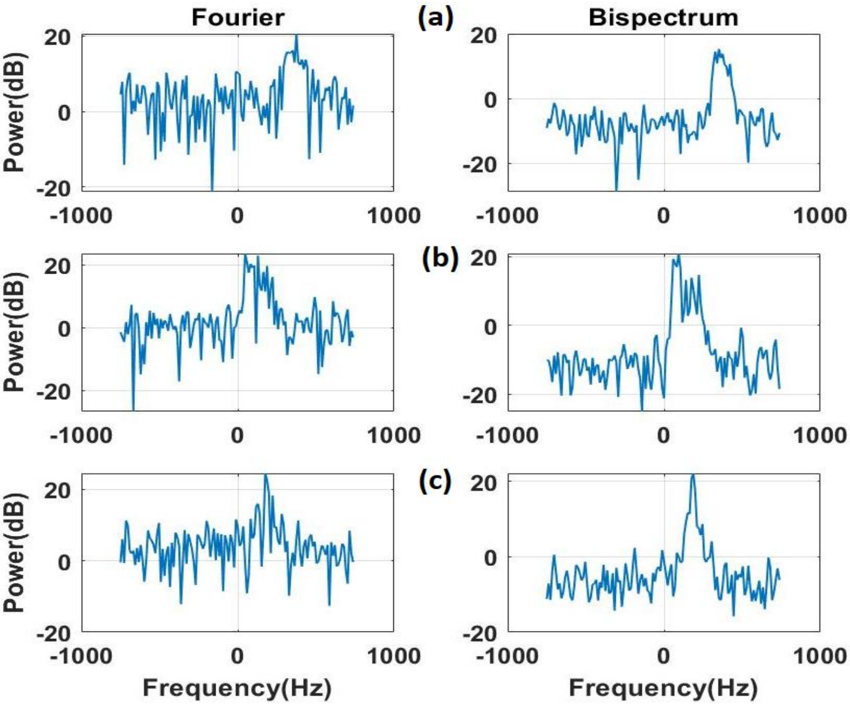

Fig. 3.6: Sample power spectrum computed through conventional method using Fourier method and Bispectrum for different range gates a) NRGB=61, b) NRGB=170, and c) NRGB=340.Sample power spectrum computed through FFT and Bispectrum at higher range bin.

Fig.3.7 show the sample power spectrum computed through Fourier and Bispectrum approaches. It can be observed that most of the weather signals are not following the exact Gaussian spectral shape; some deviations have been observed from the Gaussianity of the spectral shape. It can be seen clearly that noise fluctuations have been suppressed in the bispectrum approach. Therefore, the noise level comes down to a low value compared to the conventional Fourier method.

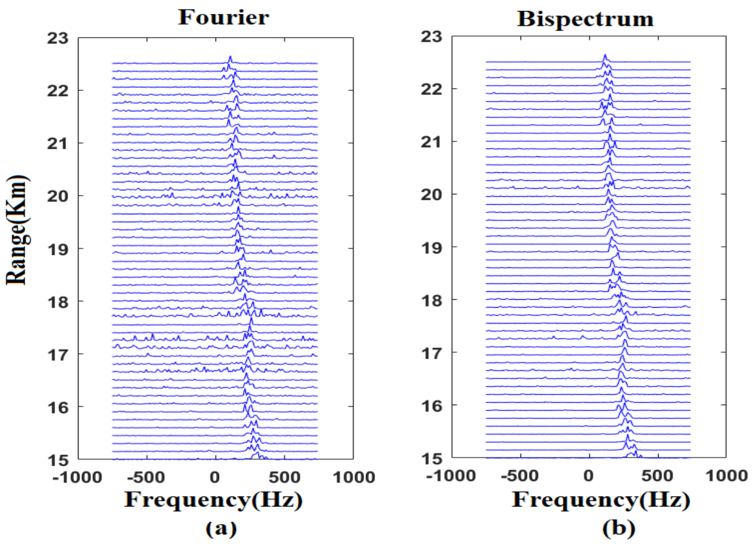

Fig.3.7: Sample power spectrum computed through conventional method using. a) Fourier method and b) Bispectrum for fewer range gates.

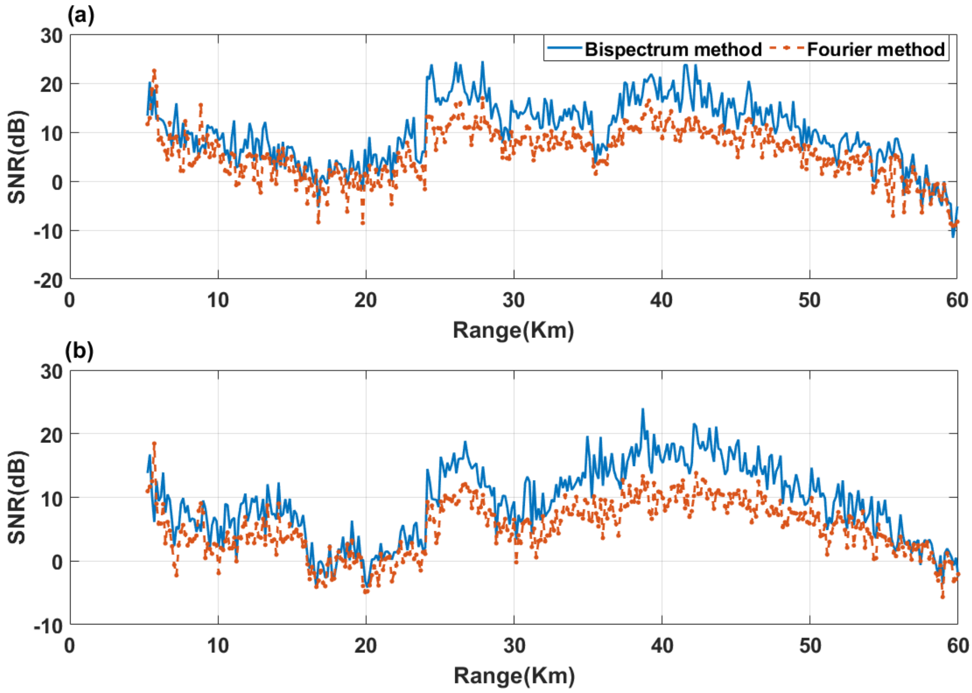

Fig.3.8: Range profiles of SNR estimated through conventional method using Fourier method and Bispectrum method a) Azimuth: 65 b) Azimuth: 70 respectively.

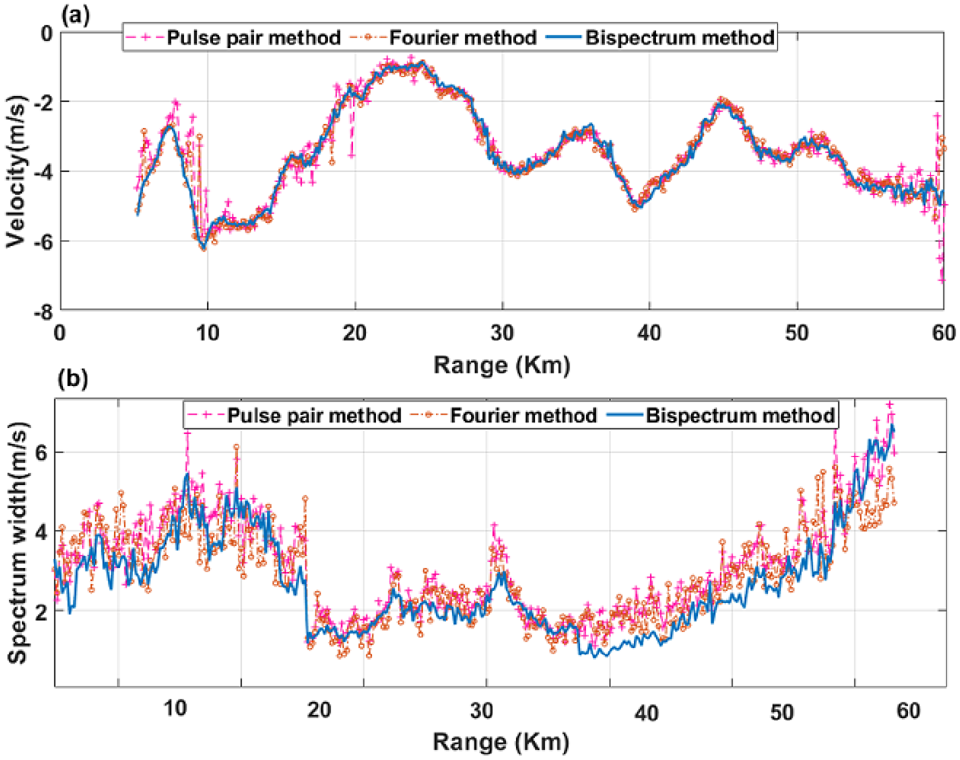

Fig.3.9: Range profiles of a) Velocity and b) Spectrum width estimated using Fourier, Pulse pair and Bispectrum method, Azimuth: 65

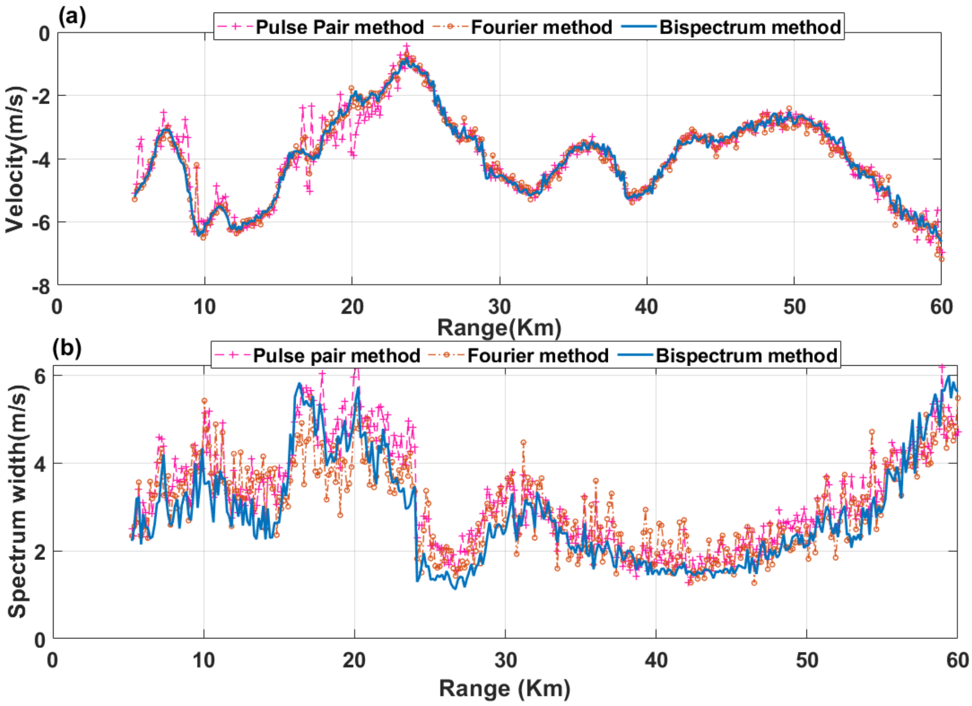

Fig.3.10: Range profiles of a) Velocity and b) Spectrum width estimated using Fourier, Pulse pair and Bispectrum method, respectively, Azimuth: 70

To understand the capabilities of both methods, one needs to estimate the spectral parameters extracted using both analyses. The mean noise level should be calculated and subtracted from the signal before estimating moments. There are different noise estimation techniques reported in the literature. Here the objective is whatever method is considered the same will be applied to both techniques so that the basic comparison of results has the same treatment on the estimation of parameters. Even though applying the Bispectrum reduces the Gaussian noise components, but needs to estimate the residual components of the noise level present in the signal. An objective method developed by Hildebrand and Sekhon (1974)is system independent and is mostly used in atmospheric signals, and the same has been used in this analysis. In this method, the mean noise level of each range bin is subtracted from the corresponding power spectra, and then the spectral moments (Bringi, 2001; Doviak, 1984) are computed.

Fig.3.8(a)-(b) shows the SNR computed using the Fourier method and Bispectrum method up to a range of 60km as it can be observed that an improvement in SNR in the precipitation region when using the bispectrum method. This is evident as the precipitation is present in the Doppler spectrum from 5km to 60km.

The Doppler weather radar not only gives information about the backscattered power received from the target but also gives information about the velocity component of the target in the direction in which the radar beam is pointed.

The target velocity is negative if it moves towards the radar and positive if it moves away from the radar. The X-Band Polarimetric DWR can track targets with a Doppler velocity range of -12 m/s to 12 m/s. Fig.3.9 and Fig.3.10 show the Doppler velocity and Spectrum width computed using Fourier, Pulse pair, and Bispectrum methods up to a range of 60km for azimuths of 65 and 70 degrees, respectively. We can observe that Doppler velocity and spectrum width profiles obtained by the three methods are almost the same, as shown in Fig. 3.9(a)-(b) and 3.10(a)-(b). It can be observed that the fluctuations are reduced in velocity and spectrum width obtained from the bispectral method compared to other conventional methods. The spectrum width range is about 0 to 7 m/s. The spectrum width is useful for the study of the turbulence characteristics of the atmosphere.

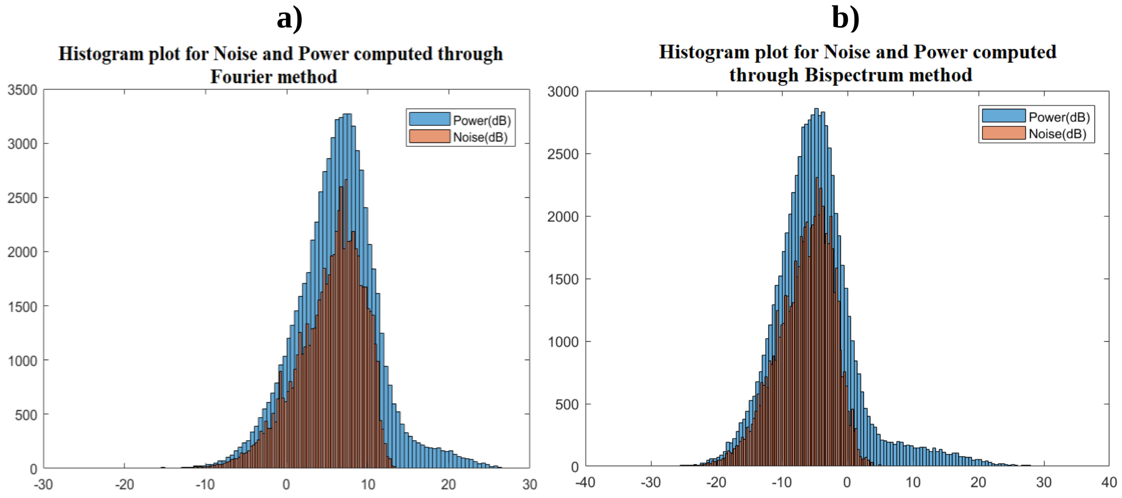

Fig.3.11: The Histogram plot of Noise and Power is computed through a). Fourier method b). Bispectrum

Fig.3.11(a)-(b) shows the histogram plots of the noise levels and the power computed through Fourier and Bispectrum methods. The noise power range in Fig. 3.11(a) is -12 to 13 dB, whereas in Fig.3.11(b), the noise power range is about -22 to 5dB. It can be seen from both figures there is a significant reduction of close to 10 dB in the noise level corresponding to the Bispectrum plot as compared to the conventional method because of the Gaussian noise elimination in the process of bispectrum estimation. From these observations, it can be concluded that the Bispectrum works effectively under noisy conditions and improves signal identification.

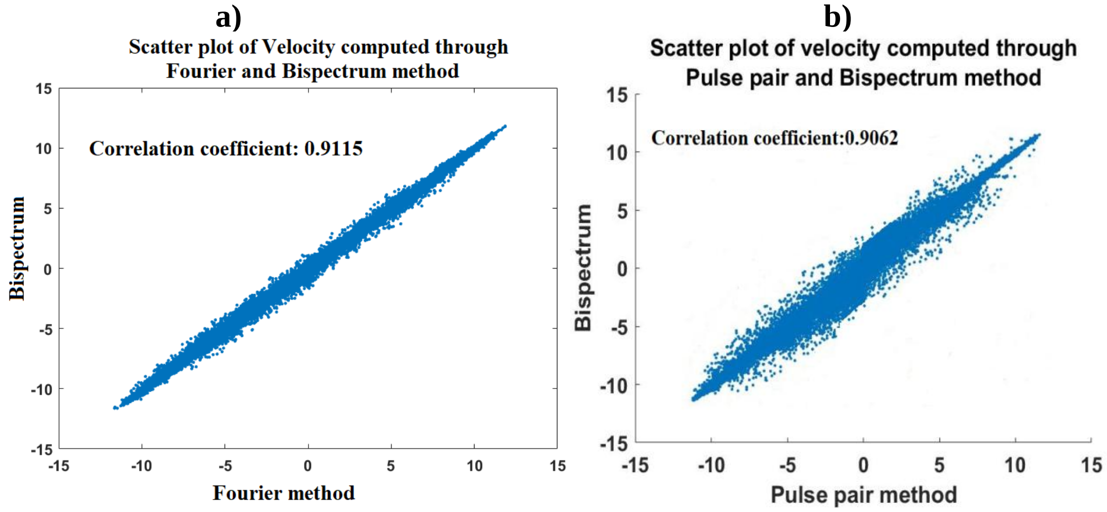

Fig.3.12: The Scatter plot of velocity is computed through the conventional method using a) the Fourier method and Bispectrum b) the Pulse pair method and Bispectrum.

Fig.3.12(a)-(b) shows the scatter plot of the velocity, which is computed by the three techniques, namely the Fourier, Pulse pair and Bispectrum methods. It can be observed that the correlation is high, which shows that the bispectral process essentially gives the same result as the conventional method based approach.

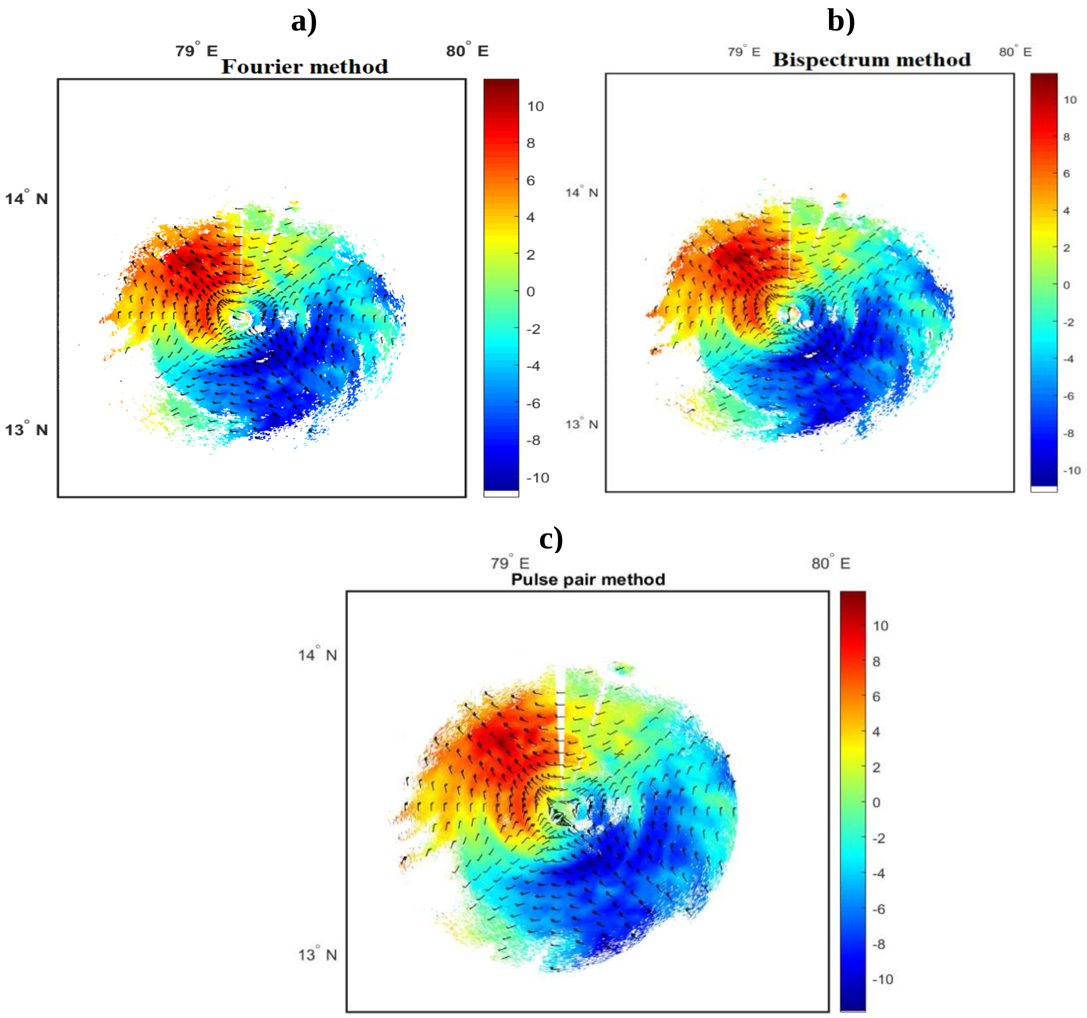

Fig.3.13: Feather plots of wind speed and direction are computed through a). Fourier method b).Bispectrum c). Pulse pair method

To study the effect of bispectrum method on the wind estimation as compared to the conventional methods, the wind speed estimation extracted by the three techniques is presented. Fig.3.13 (a)-(c) shows the feather plots of the wind speed and direction plotted on Velocity PPI plots. It can be seen clearly that in three cases, the wind direction and speed on the velocity plots arethe same. This shows that parameter extraction is not disturbed by the bispectral process. The horizontal wind speed and direction extracted by both techniques are presented by using a linear wind model (Browning,1968). The wind barbs/feather is plotted on velocity plots, representing the horizontal winds' speed and direction. The maximum wind speed observed in both cases is 12 m/s, and the wind direction is -180^0 to 180^0.

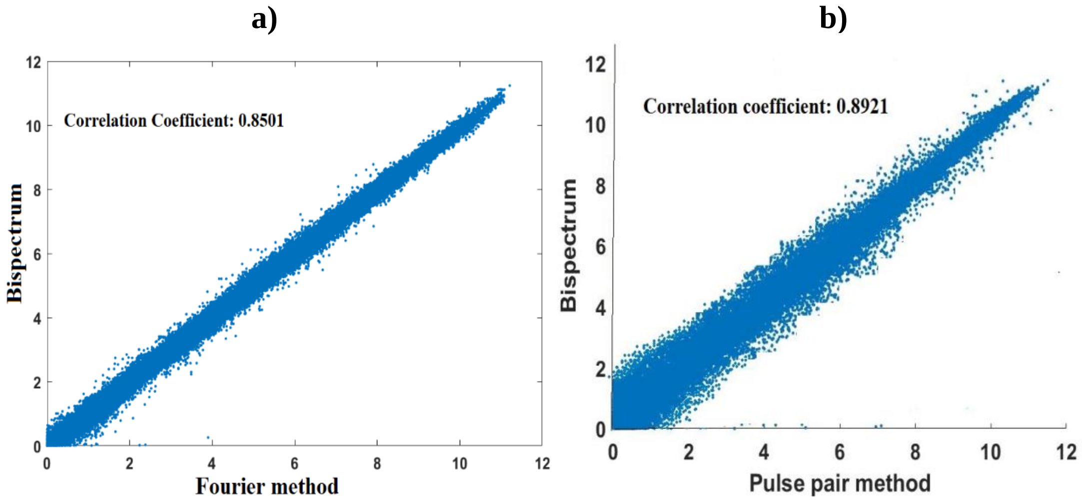

Fig.3.14: Scatter plot of Wind Speed computed through a) Fourier and Bispectrum method b) Pulse pair and Bispectrum method.

Fig.3.14(a)-(b) shows the statistical comparison of wind speed obtained from the Fourier, Pulse pair and Bispectrum based methods. It can be observed that the correlation is high, which shows that the bispectral process essentially gives the same result as the conventional method based approach. The comparison of velocity azimuth display (VAD) obtained from the three methods has been shown in Fig.3.15.

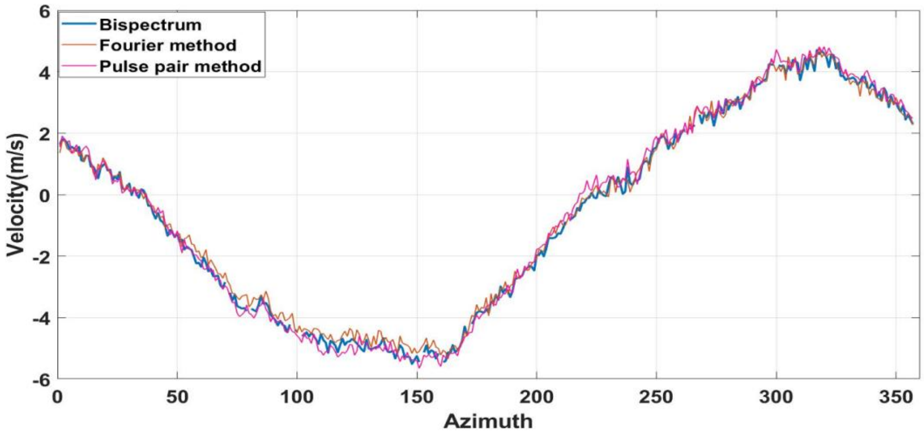

Figure 3.15: Comparison of wind velocity azimuth display obtained from the Pulse pair method, Fourier method and Bispectrum method.

In Fig.3.15, it can be observed that the three methods follow the same profile. The radial velocity is shown as a function of azimuth, which resembles the sine wave (Browning,1968). The amplitude and phase of the sine wave give the wind speed and direction, respectively.

The VAD method assumes uniform wind over the region and expects radial velocity to follow a sine curve over azimuth.

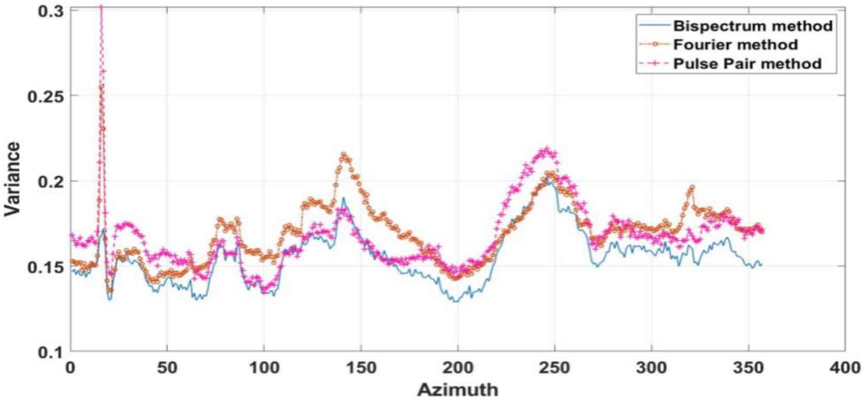

Fig.3.16: Variance profile of all azimuths estimated through conventional Fourier, Pulse pair, and Bispectrum methods.

From Fig 3.16, it can be seen that the variance plot is associated with the Fourier, Pulse pair and Bispectrum methods. The second moment gives information about variance. All azimuth scans have been considered for the variance analysis to check the relative consistency of the three methods. Fig.3.16 shows that the variance associated with Bispectrum is less compared to the conventional methods like Fourier and Pulse pair methods.The power values obtained from the bispectrum technique, Fourier and Pulse pair processing are shown in Table 3.4. The power obtained from the pulse pair technique is always high compared to the other methods. Whereas in the case of the Bispectrum,the power values obtained were almost the same as those obtained from the Fourier method. In some cases, less than 1 dB was observed in the Bispectrum approach because of the elimination of Gaussian components during the process.

Table 3.4: Power values in (dB) estimated from the Fourier method, Pulse pair method and Bispectrum

	Pulse Pair method	**Fourier Method**	**Bispectrum method**
Power Values (in dB) for a few Range	19.8065	19.7031	18.5762
	21.7483	20.4368	19.0001
	17.6456	16.6577	16.4010
	20.3248	20.2426	19.3645
	17.9864	17.4055	17.0012

bins	17.5843	16.7416	15.9635
	17.1909	16.5895	15.4023
	18.2007	17.7092	16.9521
	16.8404	16.2192	15.8771
	16.9927	15.8467	14.9675

3.8. Chapter Conclusion

From the results, it can be concluded that slight deviations occur from the Gaussianity observed from the Doppler power spectra. Therefore, the Bispectrum method significantly reduces the Gaussian noise components compared to conventional techniques like Pulse pair and Fourier methods, and this method is efficient when working under noisy conditions. This helps in improving the signal-to-noise ratio, which in turn improves the detectability of the weather signal returns. The improvement in the SNR leads to a more consistent estimate of the target velocity, especially in a noisy environment. It proves that the bispectral process improves parameter estimation. The simulation analysis considers Gaussian Mixture Models of the Doppler power spectrum with different SNR conditions. To quantify the advantage of the bispectrum approach, root mean square error (RMSE) has been estimated. It indicates that the Bispectrum decomposes the actual spectra (skewed spectra) in high SNR conditions. The results show that the bispectrum method significantly worked well for the weather signals and improved the SNR in noisy regions.

Chapter 4

Atmospheric Turbulence measurements using Higher order Spectral Analysis

Prelude: In this chapter, we discuss the Novel approach for the measurement of turbulent energy dissipation rate (ε) from Nonlinear index (NLI) based measurements using the Higher Order Spectral Estimation (HOSE) technique. This Chapter provides an overview of atmospheric turbulence and methods using both radar and radiosonde-based measurements. This chapter also briefly discusses data analysis and describes the results obtained and compares the results obtained through the proposed method with the existing approaches and gives the conclusion.

4.1 Atmospheric Turbulence: An overview

Turbulence can be considered as a nonlinear process and chaotic in behaviour that may occur in various regions of the atmosphere. The size and intensity of atmospheric turbulence may be defined by fundamental factors such as eddy dissipation rate, diffusivity, and length scales (Ghosh et al., 2003; Das, 2010). The turbulence parameters are depends on the atmospheric variables such as temperature, wind speed, and vertical shear of horizontal winds, which change with season and latitude (the parameters of both the atmosphere and the turbulence fluctuate with season and latitude). Turbulence consists of eddies of different time and length scales. The mean shear and buoyancy produce large scales in the atmosphere.

These eddies are unstable and eventually break down into eddies of smaller sizes during the inertial cascade process. During this process, eddies are folded and deformed by other eddies of similar scales. Squeezing and enlarging of eddies transfer energy into smaller ones, and so on, until eddies become so small that they work against viscous forces and convert kinetic energy into heat. Kolmogorov's theory explains the energy transportation from larger to smaller eddies. Kolmogorov's similarity hypothesis gives a simple representation of the turbulence model (Mac Cready, 1953; Batchelor, 1950).

The turbulent energy spectrum represents three different ranges of scales: energy production range, inertial subrange, and dissipation region. The shear or buoyancy mechanism produces turbulence, and the fluctuations caused by eddies have a characteristic size defined as an integral length scale. This scale for the convective boundary layer is approximately the depth of the boundary layer, while for shear, it is close to the wavelength of developing Kelvin Helmholtz waves. In the inertial subrange, turbulence can be isotropic and homogeneous (Doviak, 1984). The turbulent energy spectrum in the inertial subrange depends upon the wave number and turbulent energy dissipation rate (ε). In the dissipation region, the turbulent kinetic energy is dissipated into heat. The length scale depends only on the turbulent energy dissipation rate (ε) and kinematic viscosity (v), called the Kolmogorov microscale. This scale is typically around 1mm, at which eddies dissipate into heat and determines the size of the eddies.

In turbulent flow, quasi-random movements cause inhomogeneities in density temperature, humidity and pressure (Panchev, 1971; Rottger, 1980). Atmospheric turbulence is defined by irregularities in variables such as temperature, density, water vapour, and so on, over a wide variety of motion scales (in terms of space and time), as well as mixing characteristics. The variation in temperature and density produces small-scale inhomogeneity in the refractive index, which is responsible for the received backscatter of radio waves. Variations in the refractive index can be characterized as a spectrum with critical scales (such as the inner and outer scales of turbulence) (Tatarski, 1971). The ensemble average of the overall illuminated volume comprising scatterers with inhomogeneous volume distribution is the received backscattered power.

4.2 Turbulence generation

The generating mechanism will dictate the scale of the largest turbulent eddies; the lifespan of a turbulent flow is determined by the amount of energy supplied by its generation mechanism. The two main mechanisms of atmospheric turbulence formation are shearing and buoyancy. Static and dynamic instability (Sunil Kumar, 2015) generates atmospheric turbulence, which is related to buoyancy and shear mechanisms.

4.2.1 Shearing mechanism

Dynamic instabilities are formed by shearing forces at low viscosity, resulting in wave-like structures that eventually become unstable and leading to turbulence. Stull (1988) discusses such a destabilizing process. There is shear across a density interface, and when shear reaches a critical value, the flow becomes dynamically unstable. Then, on the interface, calm waves begin to develop. These waves' crests are normal to the direction of the shear. The amplitude of these waves continues to increase. When a wave reaches a specific point, it begins to spin up or break. A Kelvin Helmholtz wave is the name given to this breaking wave. Clear Air Turbulence (CAT) is normally associated with shear. CAT is the erratic air currents that occur in cloudless regions and cause violent aircraft buffeting. This turbulence is associated with wind shear commonly occurring at a higher altitude region from 7-12 km (John, 1967).

4.2.2 Buoyancy

In most cases, buoyant instabilities are caused by ground heating. Radiative cooling, such as at cloud tops, can also create buoyant instability by causing negative buoyancy or the release of latent heat. Convective turbulence is associated with buoyancy. Convective turbulence is commonly caused by the buoyancy mechanism, which has strong updrafts and downdrafts (Das, 2010; Sato, 1995). The existence of buoyancy as a turbulence-generating mechanism is questionable; the formation of turbulent eddies from a convective cell will emerge from the same shear-induced dynamic instabilities at small-scale shear (described in the prior section). Moving air near the edge of a convective cell is sheared by surroundings, resulting in very strong turbulent eddies.

The study of decaying homogeneous isotropic turbulence frequently starts by invoking a Fourier representation of the turbulence fields (Pope, 2000). Navier-Stokes (NS) equation (second order partial differential equation, which is useful to describe the flow of viscous fluids) contains one nonlinear term, called the convective term. After applying a Fourier transform, this term becomes nonlinear and nonlocal as it involves interactions of wavenumber triads. Pope (2000) provides a detailed description of the transport equation of turbulence in the spectral space. Triad interactions refer to the elementary momentum exchanges between Fourier components of the velocity field in wave vector space (Domaradzki, 1990). Discussions on nonlinear triad interactions of homogeneous turbulence in spectral space and detailed behaviour of the energy transfer function are reported by Orszag (1970), Domaradzki (1990), and Waleffe (1992). Various authors have reported the importance of considering local versus nonlocal triad interactions in simulations of isotropic turbulence (Yeung, 1995; Moffatt, 2013; Praskovsky et al., 1993; Domaradzki, 1990; Zhou, 1993a and b; Waleffe, 1992).

The conversion of kinetic energy into heat represents the eddy dissipation rate. It is an important parameter to understand the energy flow (which represents how the energy of eddies transfers from larger to smaller scales) within the atmosphere. Methods for estimating ε from VHF radar are discussed by Hocking (1983), Cohn et al. (1995), and Satheesan (2002). Various methods are available for estimating turbulence measurements; however, these approaches require additional in situ data. The spectrum width method is one of the most frequently used techniques for measuring the ε from the spectral moments. The major limitation of this approach is non-turbulent spectral broadening by the instrumental and meteorological sources, which need to be known and accounted for. According to Doviak (1984), five major spectral broadening mechanisms contribute to the spectrum width measurements. Spectral broadening includes beam broadening and wind shear broadening effects. The beam broadening is a consequence of the finite width of the antenna beam. Doppler spectrum narrowing and widening due to external contributions have been discussed by Koaly et al. (2002). Atlas (1964) observed that the finite beam width, wind shear, and atmospheric turbulence contribute to the spectrum width. Sloss (1968)studied shear broadening in the cross-beam motions of radar scatterers. A series of theoretical works have been reported on estimating ε from the Spectral width calculations (Frisch, 1974; Gossard, 1983; Gossard, 1998; Hocking, 1983; Hocking, 1985; Brewster, 1986; Nastrom and Eaton, 1997; Gage, 1980; Sato, 1985; Narayana et al., 1997; Delage, 1997; Ghosh, 2000; Furumoto, 2001; Narayana Rao et al., 1997; Li, 2016).

Several studies have proposed methods for spectral width corrections from radar measurements (Jacoby et al., 2002; Nastrom, 1997; Chu, 2002). In a method established by Hocking (1983), the effects of spectral broadening mechanisms have been considered and corrected to estimate the root mean square (RMS) velocity of clear air. For many years broadening effects on different targets have been examined, and many studies suggested a formula for the spectral broadening corrections to measure the ε (Frisch, 1974; Gossard, 1983; Hocking, 1983; Nastrom, 1997; Chu, 2002; Kumar, 2020). However, the turbulence measurements from the spectrum width method lead to filtered results. Some of these corrections will yield negative values of spectral widths and do not provide a consistent value of ε in the presence of strong winds (Satheesan, 2002; Doviak, 1984). Turbulence energy dissipation rate (ε) measurements from low-resolution signals are always affected by the instrument noise; some literature on instrument noise corrections is available. For example, Wilson et al. (2010, 2011) proposed a method based on optimal smoothing and statistical tests to remove the false overturns caused by the instrument noise. Waclawczyk et al. (2017) proposed a new method for estimating ε and preliminary tests of the new method performed on the data from Stratocumulants top measurement campaign (POST). He proposed two possible modifications of the zero crossing method, showing that the performance of the new methods was comparable with estimates from standard retrieval methods. The generation of turbulence in the atmosphere will create nonlinearity in the processes (Pope, 2000). This kind of nonlinear interaction among eddies can be studied using HOSE (Lii et al., 1976; VanAtta, 1979).

Here, we proposed a novel approach to estimating ε from the nonlinear index based measurements obtained from the Bicoherence (Choudhury, 2003), which provides characteristics of the turbulence in the atmosphere. Turbulence in the atmosphere causes spectral width enhancement in radar observations, making the process nonlinear. A new index has been formulated to determine the nonlinearities in the received backscattered signals. This index is called the nonlinear index (NLI), which can be calculated from the Bicoherence. It represents a measure of turbulent energy in the atmosphere for a given volume. An empirical relationship is generated using a nonlinear index to determine the turbulent energy dissipation rate (ε). Generally, spectrum width can measure the strength of turbulence since the spectrum width is a function of both meteorological and radar parameters (Doviak, 1984). Therefore, spectral broadening corrections must be done to measure the turbulence energy dissipation rate (ε). In the case of nonlinear index based estimation, the correction of parameters due to the system is not expected. This new approach is completely based on nonlinear statistics, which indirectly measures atmospheric turbulence. A large number of data sets have been considered for this analysis to ensure a good correlation exists in estimating ε between the two approaches (from the nonlinear index and spectrum width). Various literature experimentally studied the spectral energy transfer due to wavenumber interactions in a turbulent flow using Bispectrum measurements (Lii et al., 1976; Van Atta, 1979;Yamada, 2010; Hasselman, 1973; Helland, 1978; Yeh, 1973; Herring, 1980). This is one of the main reasons to consider the HOSE on atmospheric signals.

The regression analysis has been carried out, and we observed a good correlation between the estimated parameter (ε from the NLI approach) and the observed parameter (ε from the spectrum width approach). In this paper, we considered convective and clear-air event data sets to study the nonlinear interactions in the signals using HOSE. Empirically, we observed a power law relationship exists between the NLI and ε through regression analysis. Both variables are logarithmically correlated well with each other, and the observed correlation between these variables is above 75%.

4.3 Higher-order spectral analysis for nonlinearity identification

Nonlinearity identification in the system is generally based on input and output data. Such datasets can be generated for an ideally controlled system, but for most natural processes, control of the input is not possible to measure directly. Therefore, measurements are derived indirectly.

Whereas man-made structures are linear in design, they approach nonlinearity under severe load situations. The atmosphere is governed by generalized equations for thermodynamics and dynamics of the fluids.

Higher-order spectral analysis has been carried out on the backscattered atmospheric signals received from the MST radar to study the nonlinearities in the atmospheric signals caused by turbulence patterns. This new approach is completely based on the nonlinear statistics and observed in the signal regions (i.e. noise-free regions: the presence of noise generates many spurious peaks during Bicoherence estimation. These spurious peaks can be removed by following the approach of Choudhury et al. (2003)). This approach has been tested for various datasets of clear air and convective events and provides an indirect measurement of atmospheric turbulence.

Higher order spectral analysis or Bispectrum is one of the useful techniques in signal processing. The traditional signal processing tools use only first, and second-order statistics. These tools are mainly suitable for processing linear and Gaussian signals, which are not useful for finding nonlinearities in the process associated with it and the signals generated. In practice, some processes may exhibit nonlinear behaviour, i.e. the process deviates from linearity and Gaussianity. This type of behaviour can be studied using Higher-order statistics (HOS). Higher order spectrum utilizes tools such as Bispectrum and Bicoherence to identify and quantify the nonlinearities in the process. A detailed description of the Higher-order spectral analysis is given by Nikias and Mendel (1993), Nikias and Petropulu (1993), and Nikias (1987).

Bispectrum is a Fourier transform of the third-order cumulant function (Nikias and Mendel, 1993;Nikias and Petropulu, 1993). By definition, it is a 3-dimensional (3D) complex-valued function with both magnitude and phase. Therefore, the Bispectrum can be plotted against frequency variables f_1 and f_2 in a 3D plot. The interaction between frequency components f_1 and f_2 represents the nonlinear interactions in the signals and can be identified in the principal domain of Bicoherence. A detailed study of nonlinear interaction identification in the principal domain is given by Peter et al. (2006) and Jouny (1992). The Bispectrum function in discrete form is given by,

$$B(f_1,f_2)=X(f_1)X(f_2)X^*(f_1+f_2) \tag{4.1}$$

$B(f_1, f_2)=|B(f_1, f_2)|exp(j\theta(f_1, f_2))$, where f_1, f_2 are frequency indexes. X denotes the Fourier transform of the signal, and X^* is its conjugate. Bispectrum in the above equation (1) explains the three-wave interactions observed in f_1, f_2, and f_1+f_2.

We know complex signals do not have the same symmetric properties as real signals. The symmetry property of the Bispectrum of the complex-valued signals depends on the placement of the complex conjugate operator in the third-order cumulant function (Brillinger, 1967). Therefore, each moment spectra of different conjugation patterns have its own principal domain and symmetries (as shown in Table 1). The definition and symmetric properties of the Bispectrum of complex-valued signals have been discussed by Peter et al. (2006) and Jouny (1992). The bispectrum algorithm is already discussed in Chapter 3.

Anandan et al. (2001) applied Higher order spectral analysis on atmospheric signals and showed that the atmospheric signals could not be completely Gaussian in nature. Still, significant non-Gaussian components will also be present in the backscattered received signals. Conventional methods like the Fourier transform cannot identify features such as non-Gaussianity and nonlinearities of eddies in a turbulent flow.

Turbulence measurements from the spectrum width method require corrections for various radar dependent and meteorological parameters. However, the nonlinearity index does not depend on any radar system related parameters, which may help better estimate turbulence parameters in the atmosphere.

4.3.1 Spurious peaks removal

Small spurious peaks arise in the bicoherence plot occasionally, making interpretation difficult. These misleading peaks are caused by tiny values in the bicoherence denominator (Collis et al., 1998). To minimize this effect, we must add a small constant (C) to the denominator. The bicoherence denominator is comparable to the power spectrum of the original signal. If the signal includes one or more spectral peaks at specified frequencies, the denominator possesses these qualities as well.

Choosing the right value of C will aid in the removal of spurious peaks. C may be generated automatically by taking the maximum of the Pth percentiles of the estimated values of $D(f_1, f_2)$. If 25% of the values in $D(f_1,f_2)$ are assumed to represent the peaks, then P can be selected as the 75th percentile.

$$BIC^2(f_1,f_2)=\frac{|\frac{1}{M}\sum_{i=1}^{M}X_i(f_1)X_i(f_2)X_i^*(f_1+f_2)|^2}{[\frac{1}{M}\sum_{i=1}^{M}|X_i(f_1)X_i(f_2)|^2][\frac{1}{M}\sum_{i=1}^{M}|X_i(f_1+f_2)|^2]+C} \tag{4.2}$$

4.3.2 Nonlinear index measurement from Bicoherence based method

Bicoherence (BIC) is useful to provide the quantitative measure of nonlinearities in signals, and it can be obtained by statistical averaging of Bispectrum estimation and normalization procedure as given by,

$$BIC^2(f_1,f_2)=\frac{|\frac{1}{M}\sum_{i=1}^{M}X_i(f_1)X_i(f_2)X_i^*(f_1+f_2)|^2}{[\frac{1}{M}\sum_{i=1}^{M}|X_i(f_1)X_i(f_2)|^2][\frac{1}{M}\sum_{i=1}^{M}|X_i(f_1+f_2)|^2]} \tag{4.3}$$

Bicoherence (BIC) from the above (4.3) represents the squared version of the normalized Bispectrum. M is the number of data segments. Bicoherence is a dimensionless quantity that varies from 0 to 1.

The signal generation process is called linear if the signal is Gaussian (Rao and Gabr, 1980). The signal generating method should be evaluated for linearity if the signal is non-gaussian. The amplitude of the squared bicoherence for a non-gaussian and linear signal will be a non-zero constant for all bifrequencies in the principal domain. We may readily check the consistency of squared bicoherence by analyzing and observing the flatness of the 3-D squared bicoherence plot. If the magnitude of the squared bicoherence is constant at all bifrequencies in the principal domain, the variance of the calculated bicoherence should be zero.

Hinich (1982) constructed a statistical hypothesis test to identify the linearity in the signals by examining the Bicoherence at each frequency in the principal region. A limitation of this approach is that it overestimates the number of bi-frequencies in the principal domain.

Choudhury et al. (2004) constructed a nonlinearity measure by comparing the highest squared bicoherence with the average squared bicoherence plus two times the standard deviation of the estimated squared bicoherence to test the flatness or constancy of the squared bicoherence.

Later, Choudhury (2003) developed a new Nonlinear Index; to test nonlinearity in the signals. The estimation of the nonlinear index from the Bicoherence is given by,

$$NLI=BIC^2_{max}-(\overline{BIC}^2_{robust}+2\sigma_{BIC^2,robust}) \tag{4.4}$$

Where BIC^2_{robust}, $\sigma_{BIC^2,robust}$ are the robust mean and robust standard deviation, respectively. The term robust statistics refers to the measurements that are not affected by outliers in the data. They can be calculated by excluding the largest and smallest Q% of the bicoherence. A good value of Q can be chosen as 10 (Choudhury et al., 2004).

Nonlinearities can be identified and analyzed in the principal domain of Bicoherence (Peter et al., 2006; Jouny, 1992). The magnitude of this index is bounded from -1 to 1.The NLI is always less than or equal to zero for the linear signal process. For nonlinear signal processes, NLI is greater than zero.

4.4 Data Analysis and Method

4.4.1 MST radar

The MST radar is located at Gadanki (13.5^{0}N, 79.2^{0}E), Tirupati, operating in the VHF band (53MHz). This radar can detect the backscattering atmospheric echoes resulting from the small-scale inhomogeneities in the refractive index fluctuations due to variations in humidity and temperature. The data used in this analysis are collected during the convective event (on 16 March 2006, between the period of 12:00 to 17:00 Indian Standard Time (IST)) and the clear air event (on 29 July 2004, between the period of 13:00 to 15:00 IST). Convective and clear air events are selected based on observations from the vertical velocity profiles. If the vertical velocity exceeds 1.2 ms^{-1}, then the system will be considered as a convective system. Rao et al. (1999) distinguished stratiform, convective, and clear-air

Doppler profiles from the vertical velocities. Radar uses four obliques (off-vertical beams) and a vertical beam. The complete details of the system description and signal processing techniques can be found elsewhere (Rao et al., 1995). The analysis has been carried out in the height range of 3.6 to 20 km with 150 m vertical resolution along the beam direction. Experiments have been conducted in both vertical and off-vertical directions with a range resolution of 150 m. The backscattered echoes in time series are stored in the form of in-phase and quadrature phases for offline processing. Here in this paper, various data sets have been considered for HOSE analysis. Fig.4.1 shows the process steps of the proposed method.

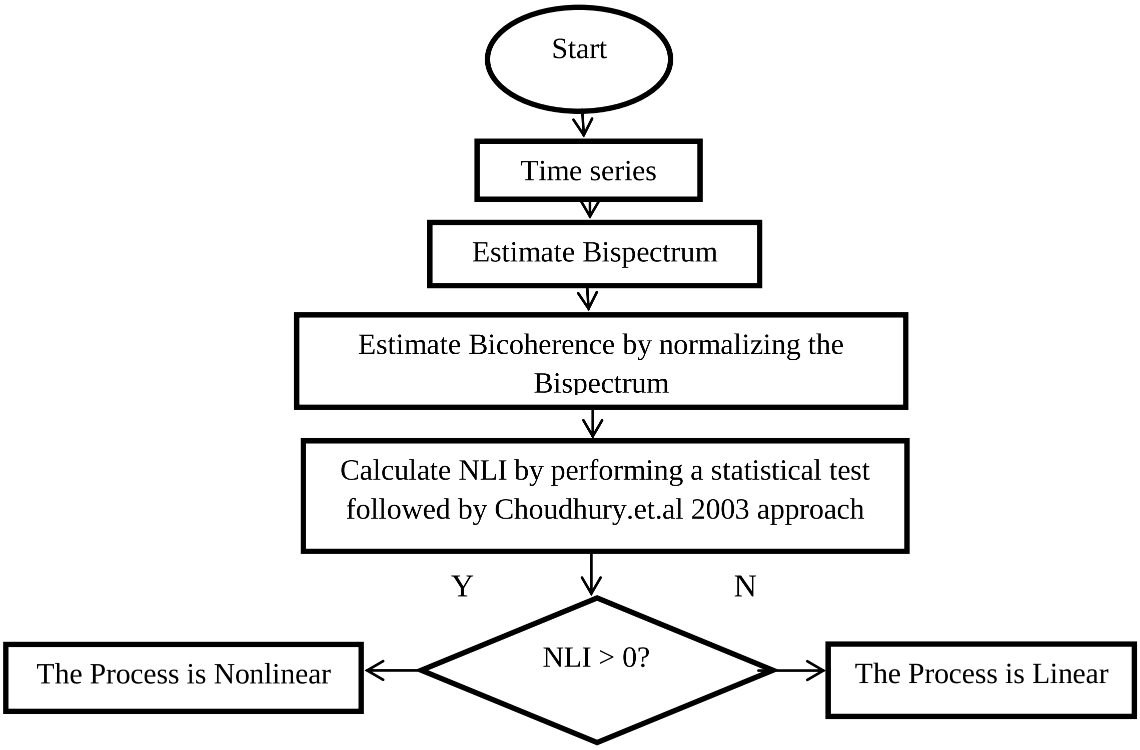

Fig. 4.1: Flow chart of process steps of the proposed approach.

4.4.2 Radiosonde

To check the accuracy of the nonlinear index based approaches, we used radiosonde data to compare the turbulence energy dissipation rate (ε) obtained from the nonlinear index (NLI) and spectral width (SW) based method. The radiosonde will be launched every day at Gadanki around 17:00 IST. In this paper, we used the Thorpe method (Thorpe and Deacon, 1977) on radiosonde data (observed on 29 August 2008, around 17:00 IST) to measure the turbulence energy dissipation rate (ε).

4.5 Results and Discussions

The Bispectrum algorithm has been applied to the atmospheric signals received from the MST radar. From Bicoherence, a nonlinear index has been calculated for each range bin. The Doppler power spectrum is computed for backscattered radar signals using Fast Fourier Transform (FFT). The mean noise level is calculated for each range bin (Hildebrand, 1974) and removed from the power spectrum, after that; moments are computed (Woodman, 1985). The spectrum width can be obtained from the second moment, which gives information about turbulence. Spectral broadening corrections have been done, followed by Das (2010) and Hocking (1983). We followed Cohn (1995) method for measuring turbulence energy dissipation rate (ε), as discussed in Chapter 2.

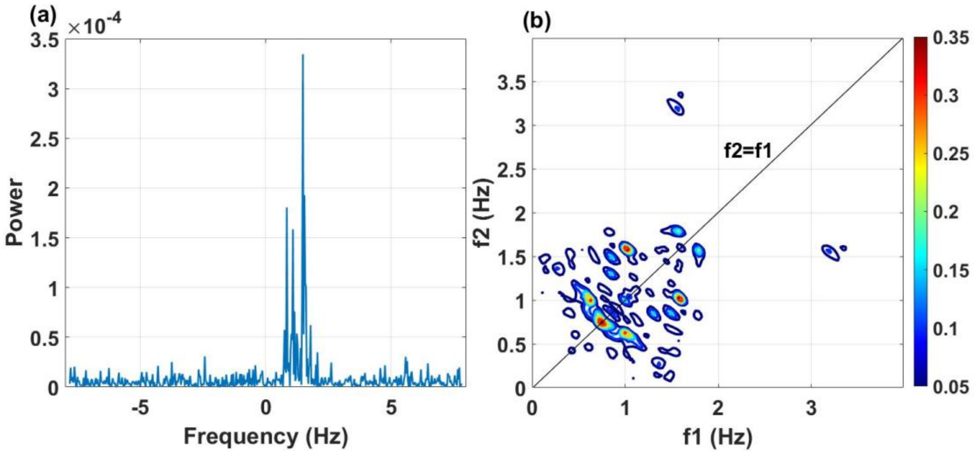

Fig. 4.2: a) Sample power spectra computed through FFT, and b) Bicoherence plot of the off-vertical beam on a clear air day

Fig. 4.2(a) shows the power spectrum obtained for one range bin (before the noise level estimation). The main atmospheric signal peak is observed from 0 to 2 Hz. Since atmospheric signals are contaminated with noise, and most of the time, their fluctuations influence the analysis. Sometimes, spurious peaks occur in the bicoherence plot due to noise in the signal; therefore, noise removal is an important part of signal processing to get the best estimation.

The noise level should be removed from the power spectrum to analyze nonlinear statistics in the signals. Fig. 4.2(b).Shows the nonlinear interactions between frequency components in the principal domain of the Bicoherence plot. A maximum bicoherence value of 0.3575 is observed at frequencies of (1.575 Hz, 1.024 Hz). Fig. 4.3(a)-(c) shows the spectrum width, turbulent energy dissipation rate (ε), and nonlinear Index (NLI) observed during a clear air day. The maximum value of 10^{-1} m^2s^{-3} turbulence energy dissipation rate is estimated at 15-20 km height, as shown in Fig. 4.3(b). At this height, there is always a large disturbance in the atmosphere associated with the shear mechanism. It can be seen from Fig. 4.3(a) and Fig. 4.3(c) that a significant enhancement in the value of the nonlinear index is observed along with a large value of spectral width at the same region. The characteristic of this enhancement resembles that of ε estimated. The maximum spectrum width is observed around 3 ms^{-1}, and the maximum nonlinear index is around 0.75 between the 15-20 km altitude region. Fig. 4.4(a)-(c) shows the spectrum width, turbulent energy dissipation rate (ε), and nonlinear Index (NLI) for the observation conducted during the convective system prevailing over the radar site. Here also, it is observed that the profiles of the nonlinear index, spectrum width, and turbulence energy dissipation rate almost follow the same pattern. In Fig. 4.4(c), the maximum nonlinear index is observed to be around 0.23 at the height of 10-12 km; the same is observed in the spectrum width and turbulent energy dissipation rate at this height, as shown in Fig. 4.4(a) and Fig. 4.4(b).

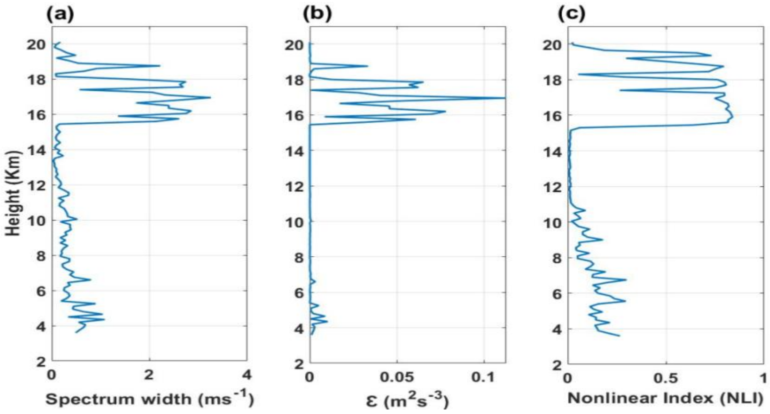

Fig. 4.3: Height profiles of a) Spectrum width (ms^{-1}), b) Turbulent energy dissipation rate, ε (m^{2}s^{-3}) and c) Nonlinear index observed on a clear air day.

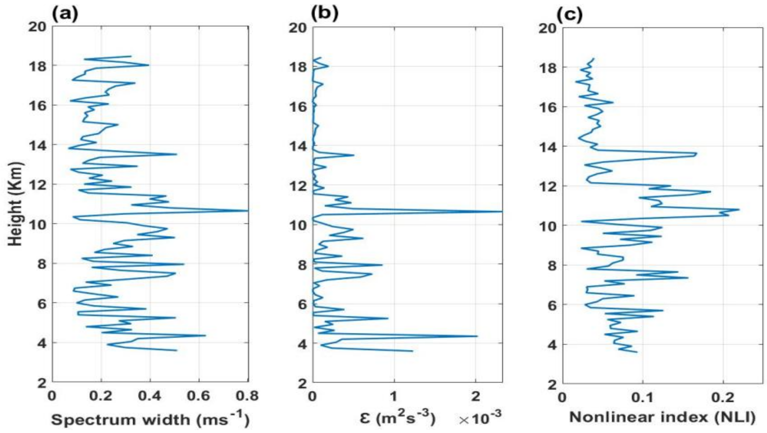

Fig. 4.4: Height profiles of a) Spectrum width (ms^{-1}), b) Turbulent energy dissipation rate, ε (m^2s^{-3}) and c) Nonlinear index observed on a convective day.

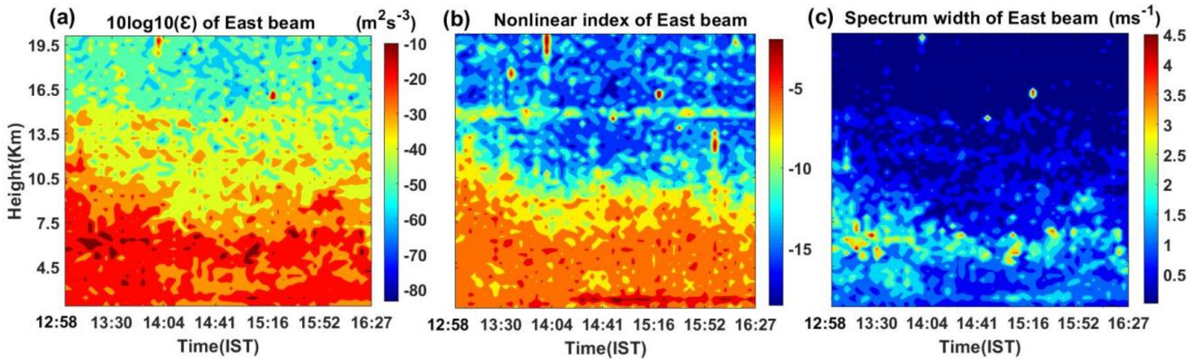

Fig. 4.5: The height and time contour plots corresponding to a) Turbulent energy dissipation rate, ε (m^2s^{-3}) in log scale, b) Nonlinear index (NLI) in log scale, c) Spectrum width in ms^{-1}, of the off-vertical beam (East beam) of the convective system observed on 16 March 2006.

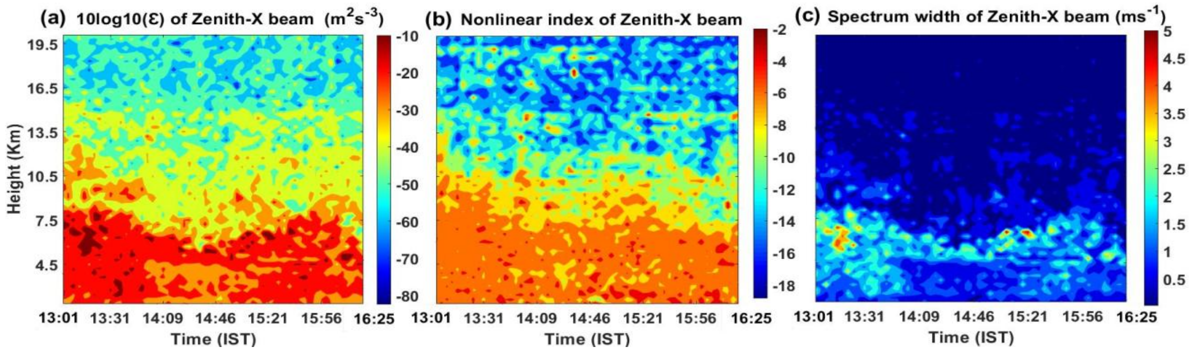

Fig. 4.6: The height and time contour plots corresponding to a) Turbulent energy dissipation rate, ε (m^2s^{-3}) in log scale, b) Nonlinear index (NLI) in log scale, c) Spectrum width in ms^{-1}, of the vertical beam (Zenith-X) of the convective system observed on 16 March 2006.

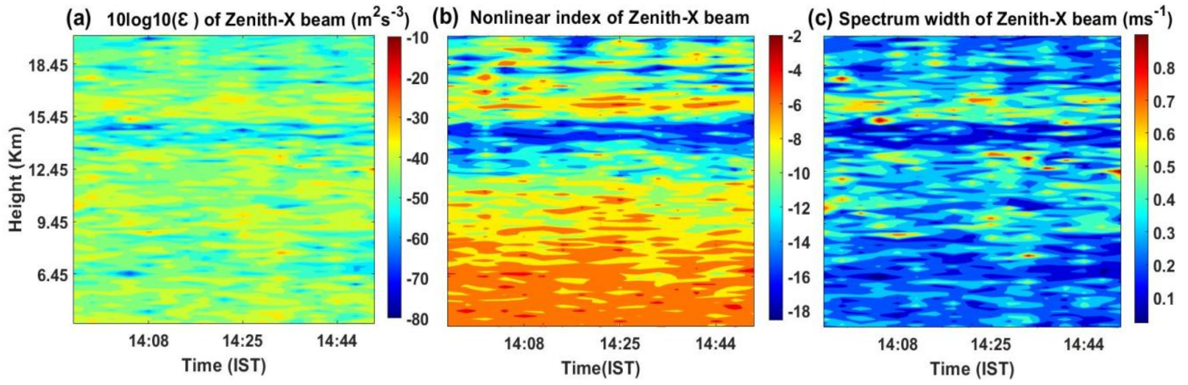

Fig. 4.7: The height and time contour plots corresponding to a) Turbulent energy dissipation rate, ε (m^2s^{-3}) in log scale, b) Nonlinear index (NLI) in log scale, c) Spectrum width in ms^{-1}, of the vertical beam (Zenith-X) of clear air system observed on 29 July 2004.

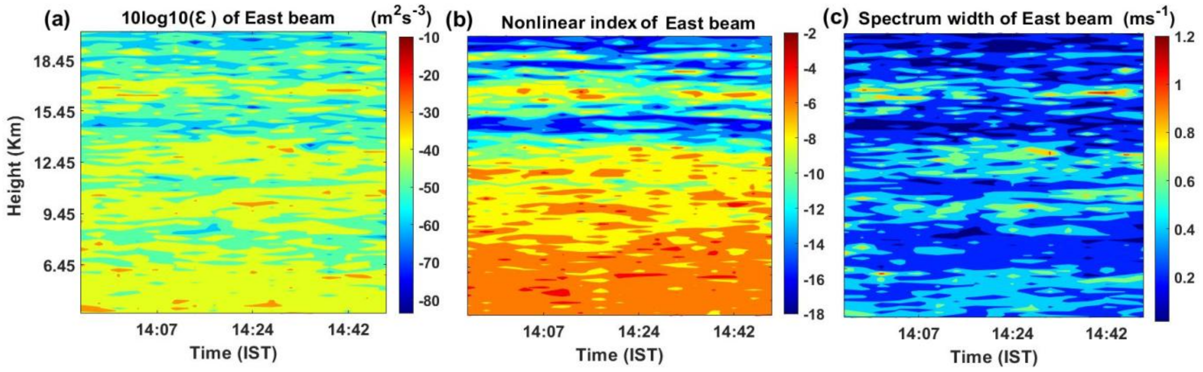

Fig. 4.8: The height and time contour plots corresponding to a) Turbulent energy dissipation rate, ε (m^2s^{-3}) in log scale, b) Nonlinear index (NLI) in log scale, c) Spectrum width in ms^{-1}, of the off-vertical beam (East beam) of clear air system observed on 29 July 2004.

4.5.1 Case 1: Convective system (16 March 2006)

Analysis has been carried out in many data sets for better understanding and quantifying these two approaches (ε from the spectrum width and nonlinear index). A convective system was observed over the radar site on 16 March 2006 between the period of 12:00 to 17:00 IST. Both vertical and off-vertical beams have been considered for the analysis. Fig. 4.5(a)-(c) shows the range and time contour plots corresponding to the turbulent energy dissipation rate (ε), nonlinear index, and spectrum width.

Fig. 4.5(a) shows the contour plot of turbulence energy dissipation rate (ε) plotted in a log scale from 1.5 to 20 km. The turbulent energy dissipation rate range is observed from 10^{-1} to 10^{-8} m^2s^{-3}.Maximum values of turbulence energy dissipation rate (-15 to -30 m^2s^{-3}) are observed at the lowest altitude, up to 12 km, and the minimum values (-40 to -60 m^2s^{-3}) are found above 13.5 km. These values may vary depending on the season (Nastrom, 1997). Strong turbulence can occur in the lower regions of the atmosphere due to the convection process, where we can expect a maximum number of nonlinear interactions among eddies in this region. Therefore the index of nonlinearity will be more in this turbulence region. It can be observed from Fig. 4.5(b) that the nonlinear index indirectly gives an indication of turbulent energy dissipation rate (ε), as it has a maximum value of the nonlinear index at lower height regions up to 10.5 km, similar kind of enhanced values of turbulence energy dissipation rate and spectrum width observed at the same region. Therefore, it can be observed clearly that there exists a good similarity between the nonlinear index and turbulent energy dissipation rate (ε). Fig. 4.5(c) shows the spectrum width values vary between the range of 0 to 5 ms^{-1}, the maximum spectrum width of 2 to 4.5 ms^{-1} is observed at lower heights (~10 km), and minimum values are found above 13 km with a magnitude around 0.5 ms^{-1}. Fig. 4.6(a) shows the strong turbulence (-10 to -30 m^2s^{-3}) that occurred in the regions of the lower layer (up to 10 km height); correspondingly, we can observe the maximum values in nonlinear indexes and spectrum width (2 to 4.5 ms^{-1}) at the same region, as shown in Fig. 4.6(b) and Fig.4.6(c).

4.5.2 Case2: Clear Air system (29 July 2004)

Radar observations during clear air day (on 29 July 2004, between the period of 13:00 to 15:00 IST) were also considered for the higher order spectral analysis to identify the nonlinear interactions between the eddies in a turbulent flow caused by wind gradients/wind shears. It is expected that strong wind shear regions have more turbulence. Fig. 4.7(a) and Fig. 4.8(a) show the contour plot of turbulent energy dissipation rate corresponding to vertical and off-vertical beams plotted in a log scale from 3.6 to 20 km. The lower regions have strong turbulence (-35 to -45 m^2s^{-3}) up to an altitude of 12.5 km; also, we can observe the maximum value of the nonlinear index at the same region, as shown in Fig. 4.7(b) and 4.8(b). From Fig. 4.7(a) and Fig. 4.8(a), a strong turbulence peak is observed between the region of 15 to 18.5 km; this may be due to the presence of temperature sheets near the tropopause region. These sheets are commonly formed in regions of higher static stability (Luce, 2001; Jayarao, 1994; Lane et al., 2003; Trier et al., 2020; Sharman et al., 2012; Ko and Chun, 2019; He et al., 2022; Nath, 2009). The study of temperature sheets is detailed given in Chapter 6. We can see that similar enhanced values of the nonlinear index are also observed at the same altitude (15 to 18.5 km), as shown in Fig. 4.7(b) and Fig. 4.8(b). From Fig. 4.7(c), the spectrum width is found to be in the range of 0 to 0.9 ms^{-1}, with a maximum value of 0.5 to 0.9 ms^{-1} found near 9.45 to 12 km and above 15 to 18.45 km. Fig 4.8(c) shows the maximum values of spectrum width observed at the height of 15 to 18.45 km with a magnitude of 0.5 to 1.2 ms^{-1}.

4.6 Regression Analysis of Variables

We established an empirical relationship between the nonlinear index (NLI) and turbulent energy dissipation rate (ε) through regression analysis. It is observed that the turbulence energy dissipation rate is proportional to the nonlinearity index raised to a power. Therefore, we considered the power regression model for this analysis. Since power regression is a nonlinear model, thus we calculate the logarithms of the parameters to obtain a linear regression. A perfect fit regression has been established using a log regression model and tested for various data sets. We observed that the correlation coefficient between the two approaches is approximately 0.80, as given in Table 3.

The empirical relationship between turbulence energy dissipation rate measured from spectrum width and nonlinear index in the power model is given by

$$\varepsilon=A(NLI)^{B} \tag{4.5}$$

To obtain a linear regression model, apply log10 in the above equation on both sides.

$$log10(\varepsilon)=log10(A(NLI)^{B}) \tag{4.6}$$

After transforming variables into the log-log regression model, the (4.6) can be written as

$$log10(\varepsilon)=p1(log10(NLI))+p2 \tag{4.7}$$

Where A and B are nonlinear regression coefficients, and p1 and p2 are log-transformed linear regression coefficients. The values of corresponding R^2 and correlation coefficient for different data sets of convective and clear air systems have been given in Table 3. From the analysis of various data sets, we observed that the values of $p1$=5.4, $p2$=-0.9415, A≈0.1144, and B=5.4. The values of $p1$, $p2$, A, and B closely match with the values obtained from various data sets. These values have been checked for different data sets and found to have a good correlation between NLI and ε.

Therefore (4.7) can be summarized empirically, and it is given by

$$log10(\varepsilon)\approx 5.4*(log10(NLI))-0.9415 \tag{4.8}$$

$$\varepsilon \approx 0.1144*(NLI)^{(5.4)}$$

$$NLI\approx 1.4940*(\varepsilon)^{(1/5.4)} \tag{4.9}$$

The above (4.9) is valid for both convective and clear air systems.

Fig. 4.9(a) and 4.9(b) show the turbulence energy dissipation rate (ε) computed from the spectrum width (SW) and nonlinearity index (NLI) observed during convective (16 March 2006) and clear air events (29 July 2004). It can be seen that the turbulent energy dissipation rate follows almost the same for both techniques.

Fig. 4.10(a)-(d) shows the statistical comparison of turbulence energy dissipation rate estimated from spectrum width (ε_{SW}) and from nonlinearity index (ε_{NL}) observed from the corresponding datasets of 16 March 2006, 29 July 2004, 29 August 2008, and 23 June 2007 respectively. The correlation coefficients observed from these figures are above 0.7.

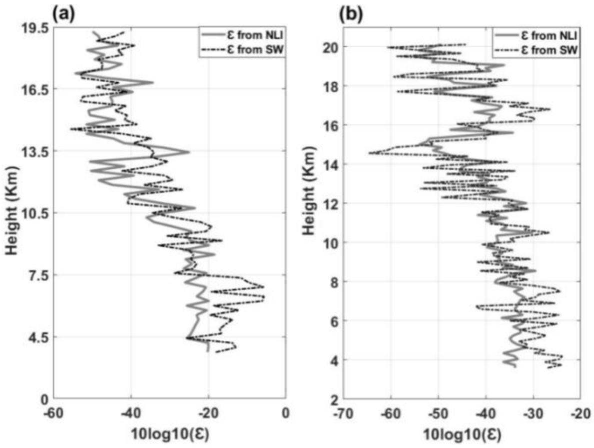

Fig. 4.9: Height profiles of turbulence energy dissipation rate, ε (m^2s^{-3}) computed from spectrum width (SW) (dotted line) and Nonlinearity index (NLI) (Solid line) in log scale for the data sets of, a) 16 March 2006, and b) 29 July 2004.

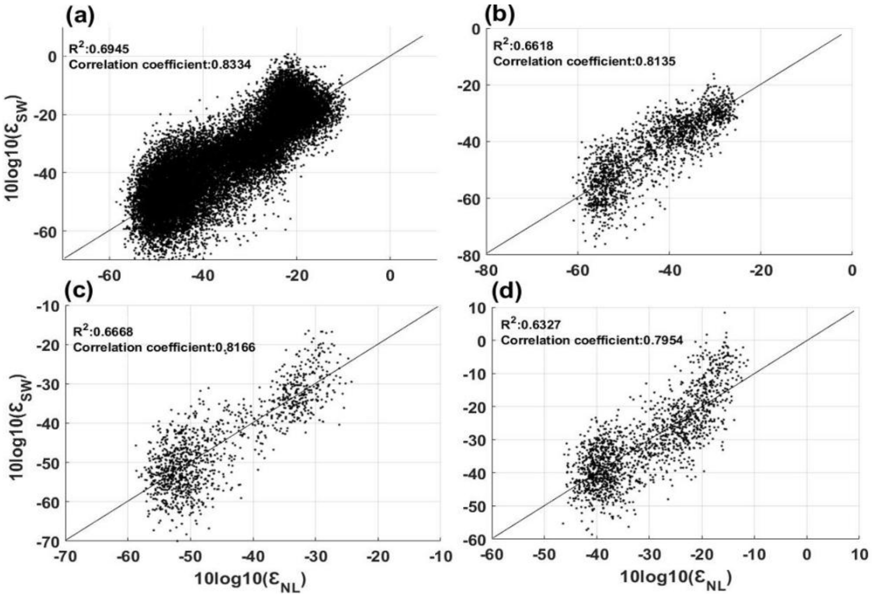

Fig. 4.10: Scatter plot of turbulence energy dissipation rate, ε (m^2s^{-3}) measured from spectrum width and nonlinearity index in log scale for different data sets of a) 16 March 2006 b) 29 July 2004 c) 29 August 2008, and d) 23 June 2007.

4.7 Error analysis

Table 4.1: Standard Error values of regression model for different data sets.

Data sets	Standard Error (SE)	P value
16 March 2006	0.1412	2e-37
29 July 2004	0.181	5e-29
19 June 2020	0.24	0.25e-34
24 April 2019	0.112	3.5e-40
29 August 2008	0.38	6e-39
23 June 2007	0.290	5.5e-39
09 October 2009	0.100	4.2e-25
21 September 2009	0.172	3.1e-22

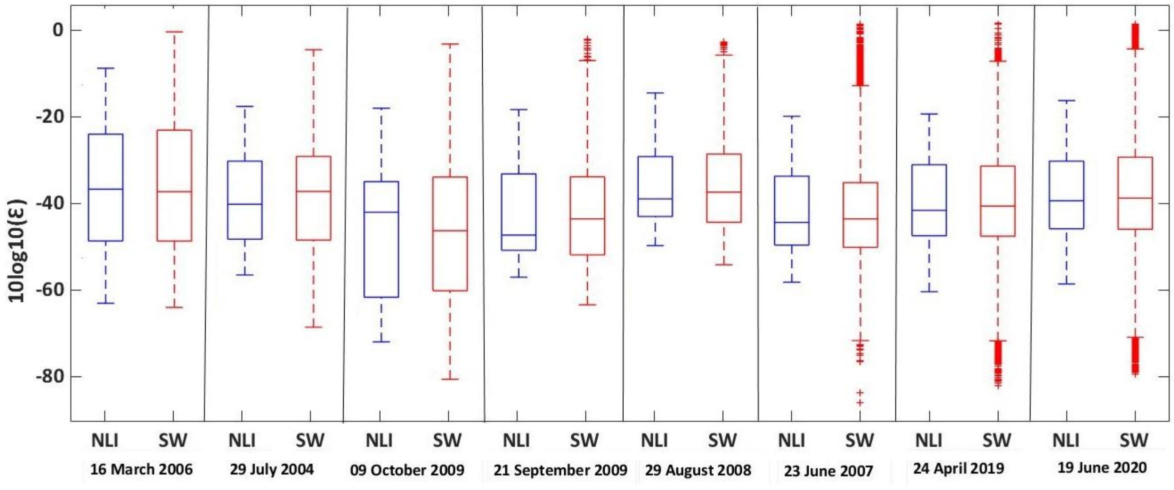

Fig. 4.11: Boxplot of turbulence energy dissipation rate, ε (m^2s^{-3}) obtained from the NLI and SW (in log scale) for various data sets

Fig.4.11 shows the boxplot of ε obtained from the NLI and SW method for the various data sets of 16 March 2006, 29 July 2004, 09 October 2009, 21 September 2009, 23 June 2007, 24 April 2019, and 19 June 2020, respectively. The Middle line of each box represents the median value, and it is observed between the range of 10^{-3} to 10^{-5} m^2s^{-3}. We can see from the boxplots the spread of data is less in NLI based approach compared to the spectrum width based approach. The corresponding standard errors of the estimates of each data set have been listed in Table 2.

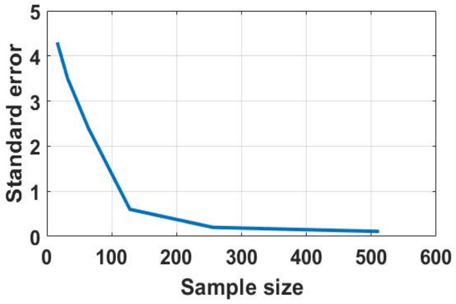

Fig. 4.12. Standard error of the estimates with different sample sizes

To assess the accuracy of estimations and to check the error in the third-order statistics, we considered different sample sizes for the analysis. We calculated the standard error of the estimates. Fig. 4.12 shows the standard error as a function of sample size. It shows that Bispectrum produces consistent results as the sample size increases; thus, the standard error decreases, indicating that the observations are closer to the fitted line.

4.8 Turbulence Parameters estimation from Radiosonde and Radar observations and its comparison

Atmospheric turbulence parameters such as eddy dissipation rate, diffusivity, inner scale, and outer scale of turbulence can be measured using radiosonde instruments. The transformation of turbulence energy from larger scale to smaller scale eddies is called inertial subrange. In an isotropic, homogeneous turbulence, the eddy dissipation rate equals the spectral energy flux or the cascade rate within the inertial subrange. Eddy dissipation rate can be estimated by integrating the wave number space of kinetic energy loss due to molecular viscosity per unit mass. Thorpe method (Thorpe and Deacon, 1977) has been utilized to estimate the turbulence eddy dissipation rate, as discussed in Chapter 2.

4.8.1 Turbulence length scales

Length scales are useful to represent the size of the eddies. The buoyancy scale represents the largest eddies that can be obtained from ε and N.

$$l_0=7.4\eta \tag{4.10}$$

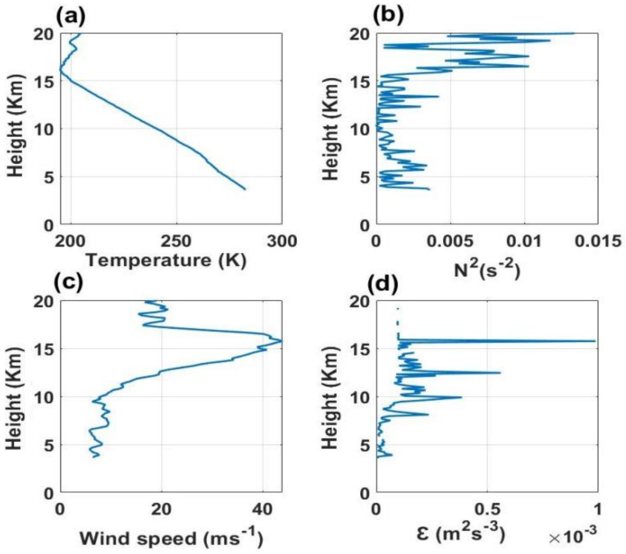

Fig. 4.13. Profiles of a) Temperature (K), b) Stability parameter (s^{-2}), c) Wind speed (ms^{-1}), and d) Turbulence energy dissipation rate, ε (m^2s^{-3}) obtained from the Radiosonde data on 29 August 2008 (05:00 IST).

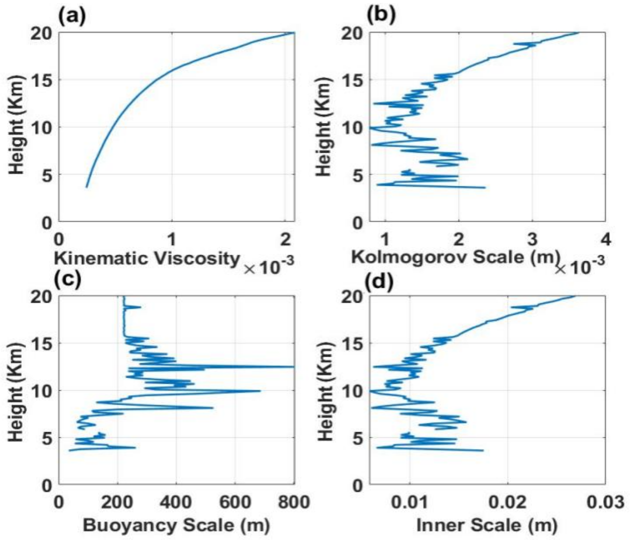

Fig. 4.14. Profiles of a) Kinematic Viscosity, b) Kolmogorov Scale, c) Buoyancy Scale, and d) Inner scale obtained from the Radiosonde data on 29th August 2008 (05:00 IST)

Fig.4.13(a)-(d) shows the vertical variation of temperature, stability parameter, wind speed, and ε, respectively. The variation of the stability parameter is observed in the order of $0.01s^{-2,}$ as shown in Fig. 4.13(b).

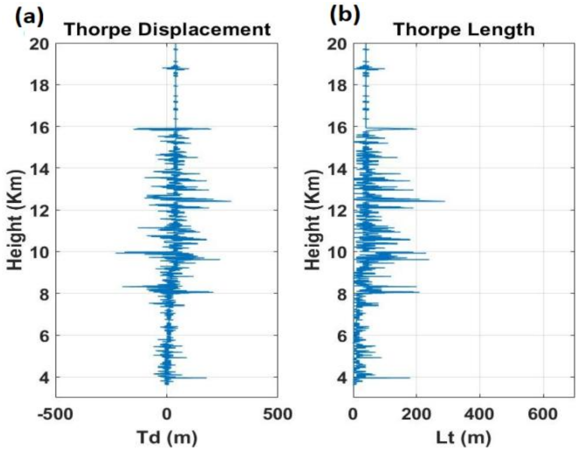

Fig. 4.15. Thorpe Displacement and Thorpe length obtained from the radiosonde.

From Fig. 4.13(c), the maximum wind speed is observed between the region of 10 to 18 km. The maximum values of ε (~ 0.001 m^2s^{-3}) are observed above 8 km, 12 km, and 15 km (Fig. 4.13(d)). Fig. 4.14(a)-(d) shows the vertical variations of kinematic viscosity, Kolmogorov scale, buoyancy scale, and inner scale. It can be seen from Fig. 4.14(a), the variation of kinematic viscosity increases with height. Fig. 4.14(b) shows the Kolmogorov scale, varying from ~0.001 to 0.004 m. The buoyancy scale varies from 10 to 800 m (in Fig. 4.14(c)). Variations of inner scales are observed in the order of 3×10^{-2} m, as shown in Fig. 4.14(d), with smaller values occurring at lower altitudes and larger values at higher altitudes. Fig. 4.15 shows the vertical profiles of Thorpe displacement and Thorpe length, respectively. The Thorpe length is the root mean square of the Thorpe displacement.

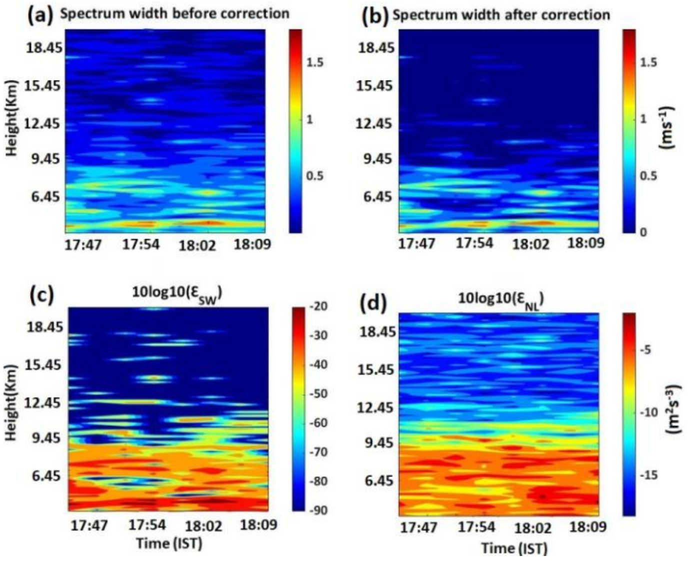

Fig. 4.16. Contour plots of Spectrum width (ms^{-1}) a) before and b) after corrections and turbulence energy dissipation rate, ε (m^2s^{-3})obtained from the c) SW, and d) NLI (in log scale).

Fig.4.16(a)-(d) shows the contour plots of spectrum width before and after spectral broadening corrections followed by Das (2010) and Hocking (1983), and ε obtained from the spectrum width (after corrections) and nonlinear index. The maximum values of ε (-20 to -45 m^2s^{-3}) in the log scale are observed between the region of 3.6 to 9.5 km, as shown in Fig. 4.16(c). We can observe that maximum values of the nonlinear index are also found at the same region of 3.6 to 9.5 km, as shown in Fig. 4.16(d). Therefore, the nonlinear index indirectly indicates turbulent energy dissipation rate (ε),

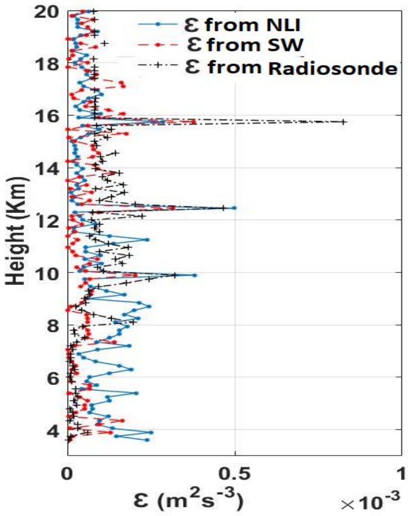

Fig. 4.17. Comparison profiles of turbulence energy dissipation rate, ε (m^2s^{-3}) obtained (in log scale) from the GPS Radiosonde, NLI, and SW

4.9 Frequency distribution of Turbulence energy dissipation rate

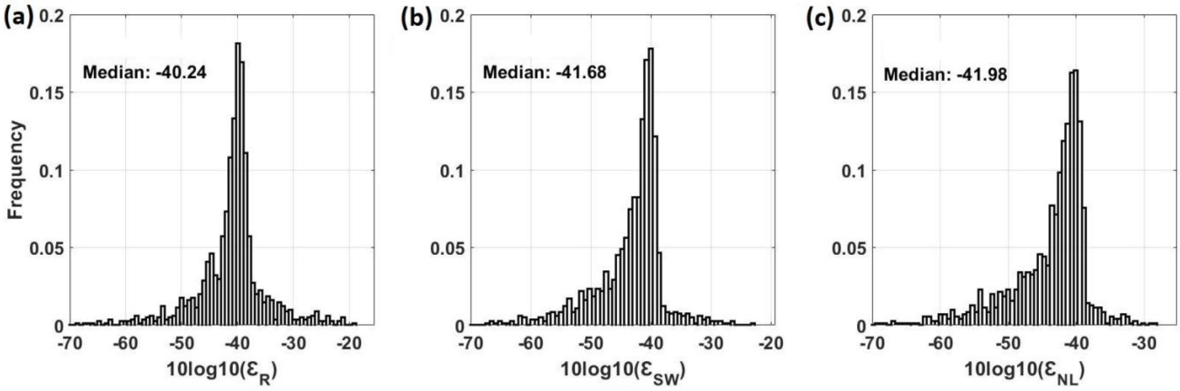

Fig. 4.18: Histogram plots of turbulence energy dissipation rate, ε (m^2s^{-3}) obtained (in log scale) from the a) GPS radiosonde, b) SW, and c) NLI

Fig. 4.17 shows the comparison profiles of ε obtained from the radar (NLI and SW) and radiosonde measurements (using the Thorpe method). The variation of ε obtained from the radiosonde measurement agreed well with that of the NLI and SW method. In all estimates, large values of ε are observed from 9 to 10 km, 12 to 13 km, and 15 to 16 km. Kohma et al. (2019) assumed that the distance between the radiosonde and the radar slightly affects the statistics, and the radiosonde did not always measure the same volume as the radar. Earlier studies compared ε estimation from radar and radiosonde based measurements and observed the difference in the order of magnitude of 1 (Kohma. et al., 2019). Previous research (Kantha and Hocking, 2011; Li et al., 2016) revealed that due to the high degree of intermittency and spatial variability of turbulence in the free atmosphere, a one-to-one connection between radar and radiosonde estimations is challenging. As a result, many earlier research concentrated on the statistics of the two estimations, despite the fact that some papers detailed case studies of turbulent layers from simultaneous radar and radiosonde observations (Wilson et al., 2014). In the next Section, the current study compared radar and radiosonde-based estimations.

Fig. 4.18 (a)-(c) shows the frequency distribution of ε obtained from the radiosonde and radar based measurements (such as spectrum width and nonlinearity Index). Turbulence energy dissipation rate (in log scale) variability is observed from 10^{-7} to 10^{-2} m^2s^{-3}, with the median values of ~ 8×10^{-5} to 3×10^{-4} m^2s^{-3}. It shows that all quantities approximately follow the log-normal distribution, but radar based estimations show a slightly skewed distribution. Estimating ε from the radar and radiosonde have different approaches; furthermore, there are height ambiguities between the proportionality constant in Thorpe scale length and the Ozmidov scale (Clayson and Kantha, 2008). Comparisons between all are reasonable when all of these criteria are considered.

4.10 Comparison with previous studies on turbulence eddy dissipation rates

To check the accuracy of this algorithm, the turbulence energy dissipation rate obtained from both (NLI and SW) approaches have been compared with the previous results published by Kumar et al. (2020). The experiment was conducted on 24 April 2019 (09:43-18:33 Indian

Standard Time (IST) and on 19 June 2020 (10:36-19:22 IST), and considered these datasets for the HOSE analysis. The MST radar has been operated in vertical and two 10-degree off-vertical towards east and south directions with parameters: number of FFT points-256, Inter pulse period-160 µs, number of coherent integrations-256, pulse width-8 µs and range resolution-150 m.

Case 1: 24 April 2019

Weak to moderate winds with a magnitude of 10 ms^{-1} have been observed during this experiment. Kumar.et al.(2020)uses various antenna configurations for the spectrum width corrections (in this paper, we considered the variance values obtained from 32✕32 antenna configuration) and showed that the values of observed variance vary for east and south beams in a larger magnitude for smaller and larger configurations at 7.65 km. The correlation coefficient of the ε measurements, obtained from the NLI and SW, is around 0.79. Fig.4.19 shows the vertical profiles of temperature and brunt vaisala frequency (N) observed from the radiosonde on 24 April 2020 at 17:30 IST from Gadanki.

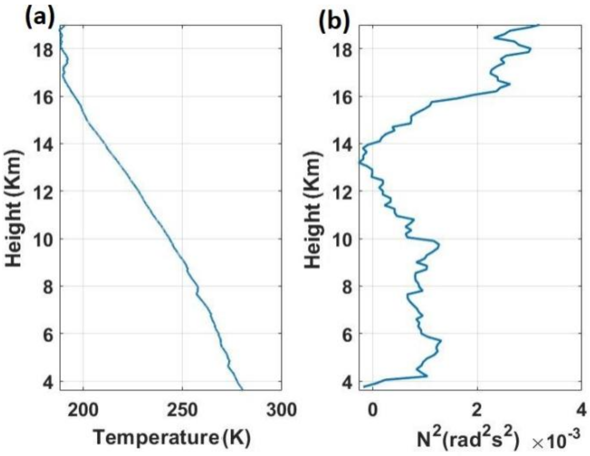

Fig. 4.19: Temperature and Stability parameter profiles obtained from the GPS radiosonde on 24 April 2019.

Fig. 4.20(a)-(c) shows the Contoured Frequency by Altitude Diagrams (CFAD) profiles of ε estimated from the NLI and SW. The values of turbulence energy dissipation rate (ε) vary between 10^{-8} to 10^{-1} m^2s^{-3} in the region of 3.6 to 18 km (in log scale), with the mean values varying from 10^{-4} to 10^{-3} m^2s^{-3} in both approaches (ε from SW and NLI). The values of ε obtained in the present study compared very well with those available in the literature (Kumar et al., 2020). Several field campaigns were conducted during this experiment to compare the ε obtained from radar and in-situ measurements. In those studies, they observed the mean values of ε vary in the range of 10^{-4} to 10^{-3} m^2s^{-3} in the lower and middle atmosphere. The present study also shows the mean value of ε approximately varies from 10^{-4} to 10^{-3} m^2s^{-3} between the region of 3.6 to 18 km, which matches well with those stated by the in-situ measurements.

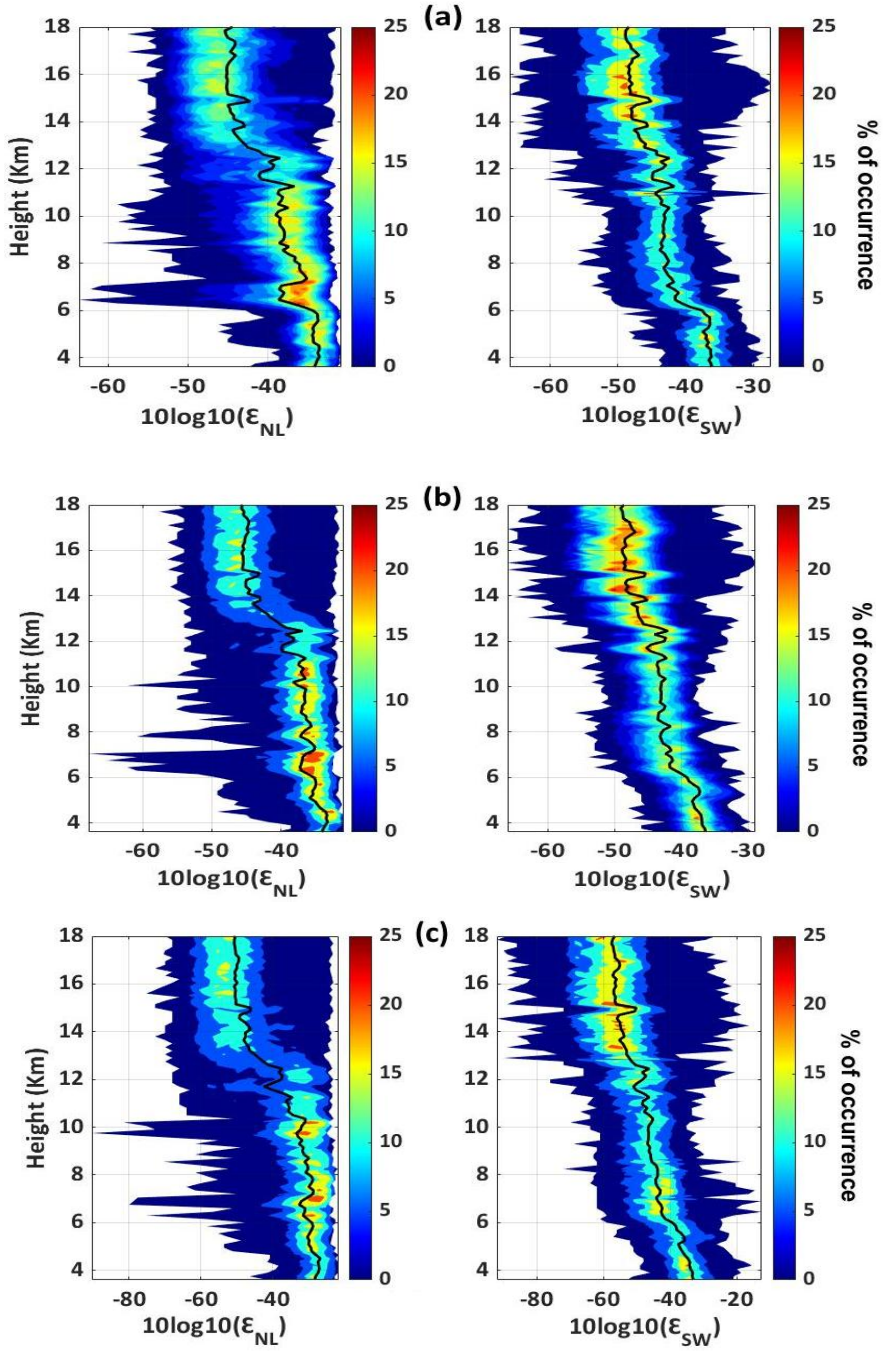

Fig. 4.20: CFAD profiles of turbulence energy dissipation rate, ε (m^{2}s^{-3}) estimated from the nonlinear index and spectrum width (in log scale) for a) East, b) South, and c) Zenith beams, respectively, on 24 April 2019 (09:43-18:33 IST).

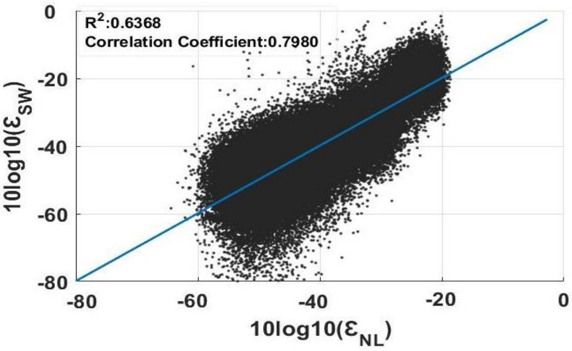

Fig. 4.21: Scatter plot of turbulence energy dissipation rate, ε (m^{2}s^{-3}) measured from spectrum width and nonlinear index (in log scale) for the data set of 24 April 2020 (09:43-18:33 IST).

Fig. 4.21 shows the statistical comparison between turbulence energy dissipation rate (ε) obtained from the spectrum width and nonlinear index (in log scale), showing a correlation coefficient of 0.7980.

Case 2: 19 June 2020

To check the efficiency of the proposed method, we considered strong wind events observed on 19 June 2020. The wind speed of more than 30ms^{-1} has been observed during this experiment due to the prevailing tropical easterly jet during the monsoon season (June-September). The corresponding plots of zonal and meridional wind components (u and v) have been shown in the literature (Kumar et al., 2020).

Fig. 4.22(a)-(c) shows the Contoured Frequency by Altitude Diagrams (CFAD) profiles of ε estimated from the NLI and SW. The range values of 10^{-6} to 10^{-1} m^{2}s^{-3} turbulence eddy dissipation rate (ε) are observed between the region of 3.6 to18 km, with the mean values of 2×10^{-4} to 8×10^{-4} m^{2}s^{-3} are observed in both approaches (ε from SW and NLI). The values of ε obtained in the present study compared very well with those available in the literature Kumar et al. (2020). Several field campaigns were conducted during this experiment to compare the ε obtained from radar and in-situ measurements. In those studies, they observed the mean values of ε vary between the range of 0.2×10^{-3} to 0.8×10^{-3} m^2s^{-3} in the lower and middle atmosphere. The present study also shows that the mean values of ε approximately vary from 0.2×10^{-3} to 0.8×10^{-3} m^2s^{-3} between the region of 3.6 to 18 km, which matches well with those stated by the in-situ measurements.

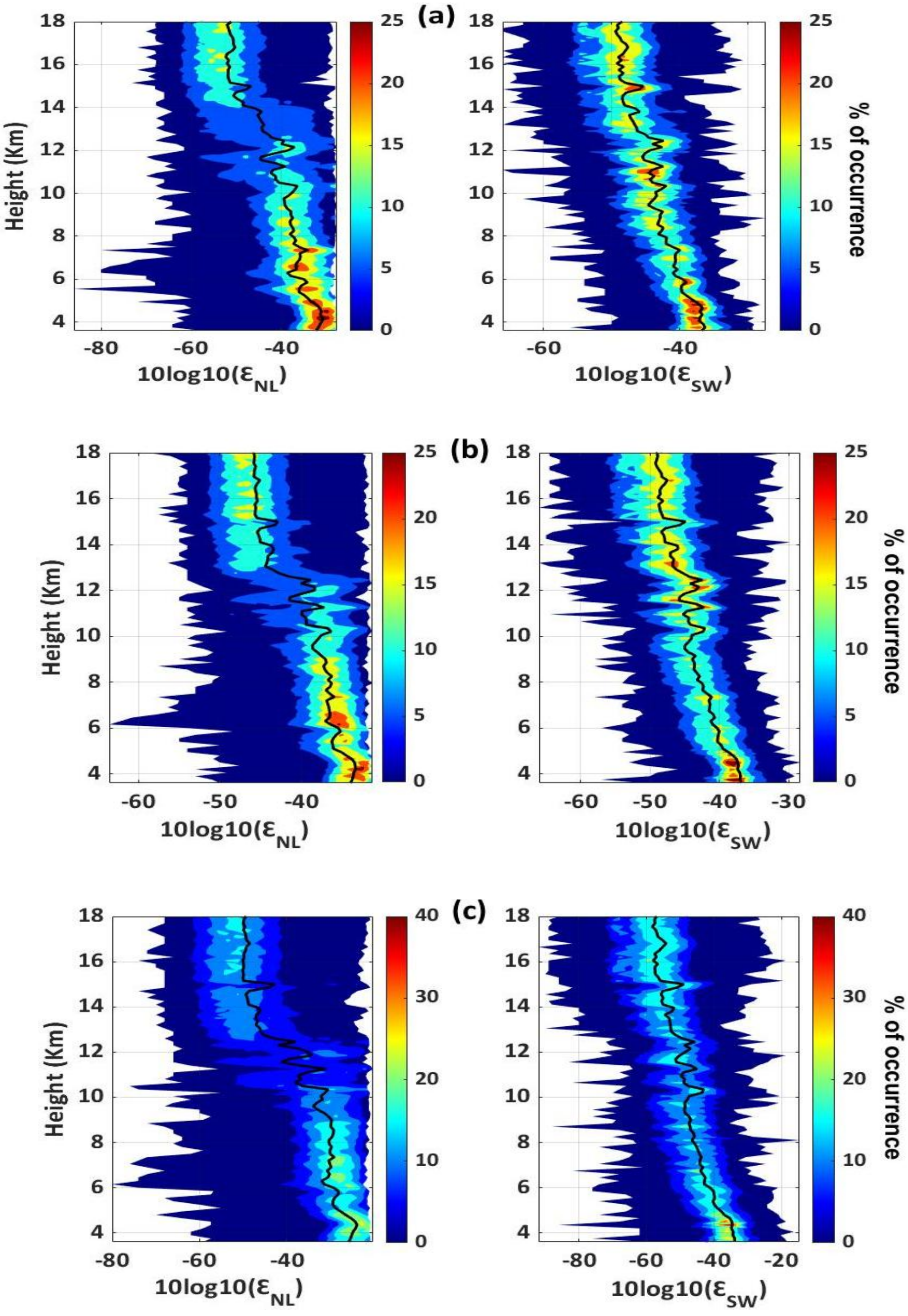

Fig. 4.22: CFAD profiles of turbulence energy dissipation rate, ε (m^2s^{-3}) estimated from the nonlinear index and spectrum width (in log scale) for a) East, b) South, and c) Zenith beams, respectively, on 19 June 2020 (10:36-19:22 IST).

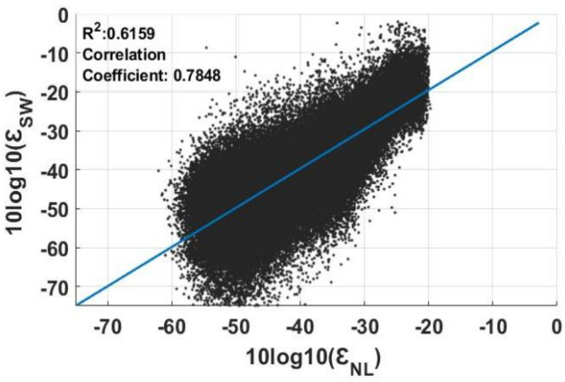

Fig.4.23: Scatter plot of turbulence energy dissipation rate, ε (m^2s^{-3}) measured from spectrum width and nonlinear index (in log scale) for the data set of 19 June 2020 (10:36-19:22 IST)**.**

Fig. 4.23 shows the statistical comparison between ε obtained from the spectrum width and nonlinear index (in log scale), showing a correlation coefficient of 0.7848.

Table 4.2: Values of correlation coefficients for different data sets.

		DD-MM-YY	**Correlation Coefficient(CC)**
Different data sets of Clear air and convective observations	Convective system	(16 March 2006)	R^2: 0.6945, CC: 0.8334
	Clear air system	(29 July 2004)	R^2 : 0.6618, CC:0.8135
	Clear Air system	(29 August 2008)	R^2 : 0.6668, CC:0.8166
	Convective system	(09 October 2009)	R^2 : 0.7150, CC:0.8456
	Convective system	(21 September 2009)	R^2 : 0.5875, CC:0.7663
	Clear Air system	(23 June 2007)	R^2 : 0.6139, CC:0.7835
	Clear Air system	(24 April 2019)	R^2 : 0.6368, CC:0.7980
	Clear Air system	(19 June 2020)	R^2 : 0.6159,CC:0.7848

4.11 Chapter Conclusion

Higher-order spectral analysis has been applied to the atmospheric radar backscattered signals to detect the nonlinearities present in the atmospheric signals. Both convective and clear air events data have been considered for the analysis. The empirical relationships are established between NLI and ε through regression models. The turbulent energy dissipation rate (ε) estimated from the Nonlinear index matches fairly well with ε measured from the spectral width method in both clear air and convective system with a good correlation of around 0.8. A better correlation index may be possible by tuning the parameters; however, more attempts have not been made because spectral width based approaches also implement system-dependent corrections. Therefore, the possibility of estimation errors needs to be quantified in greater detail. NLI doesn't apply any correction on computed value. From the above results, we can observe that the nonlinear index shows the existence of turbulence in the backscattered signals, which means that it measures the turbulence intensity. To check the accuracy of this algorithm, a comparison has been made with the radiosonde observations and with previous studies published and found to be in good agreement. One of the limitations of this approach is that this analysis needs to be carried out on time series data having a reasonable number of sample points to capture the statistical properties, and the analysis is computationally intensive. From the above results, one can say that higher-order spectral analysis effectively identifies and characterizes the nonlinearities in the atmospheric signals, which can be used for estimating one of the important atmospheric parameters, such as turbulence energy dissipation rate.

Chapter 5

Empirical Mode Decomposition (EMD) on Weather Radar signals

Prelude: This chapterprovides an overview of various EMD denoising techniques based on threshold criteria. This chapter discusses the weather radar simulation analysis using various EMD denoising techniques in the presence of ground clutter and noise. We also discussed the limitations of the existing approaches. This chapter presents a new EMD denoising approach for removing noise and clutter in weather signals. This chapter gives the results obtained from EMD denoising techniques and provides the conclusion derived from the results.

5.1. Introduction to Empirical Mode Decomposition

The empirical Mode Decomposition (EMD) is a time domain technique that can decompose any signal into a small number of components termed as Intrinsic Mode Functions (IMF). This technique is convenient for dealing with nonlinear and non-stationary data (Huang et al., 1998). First, IMF always contains high-frequency components, which can be considered as noise. EMD-based denoising algorithms are widely used in various applications such as speech signal processing (Molla, 2007), seismic data processing, biomedical (Donoho, 1994; Hadjileontiadis, 2007; Jing-Tian, 2007; Zhang, 2007; Zhang, 2020), acoustic signals (Boudraa, 2007; Kopsinis,2008; Molla, 2007; Mao, 2007) and image processing (Ning et al., 2007; Tsolis, 2011).

Several efforts have been made to understand the performance of the EMD or enhance its performance in various applications. However, it still needs a solid mathematical theory and is, in essence, regarded as an algorithm. Some studies have proposed EMD based denoising methods using threshold criteria (Boudraa, 2004, 2006; Byung, 2004; Donoho,1994, 1995; Huang, 2000; Lagha,2013; Tsolos, 2011). However, using wavelet thresholding to IMFs directly might result in incorrect conclusions for signal continuity (Kopsinis, 2009, 2008). The hard threshold function causes certain high-frequency coefficients over the threshold to be lost. To address the shortcomings of traditional EMD threshold-based approaches, the EMD interval-based threshold was created (Kopsinis, 2009, June 2008; Yang et al., 2015).

Several EMD denoising techniques have been developed and applied in various applications. Inspired by standard wavelet thresholding techniques, a series of novel EMD-based denoising methods were developed (Kopsinis, 2009; June 2008). These methods use thresholding in the EMD domain to remove noise from the first IMFs. EMD partial reconstruction and EMD Direct threshold method have been discussed (Kopsinis, June 2008; Zhang et al., 2020), but these techniques have some limitations in reconstructing the signal. Compared to the EMD-DT technique, the EMD-IT approach significantly overcomes the denoised signal's discontinuity by considering the whole zero crossing interval of the IMF. Li et al. (2015) provide EMD denoising technique based on multiple iterations, which needs random change of the samples of the noisy regions of all IMFs. Still, one of the limitations of this approach is its computational complexity as the increase in the number of iterations.

Wu et al. (2004) used the EMD approach to expose the statistical properties of additive white Gaussian noise. They categorised each IMF according to its energy-density spread function. Boudraa et al. (2004) later suggested a denoising approach based on partial reconstruction of the relevant modes. Peng et al. (2005) established correlation-based thresholding algorithms to distinguish between relevant and irrelevant IMFs. However, because the correlation between the noisy signal and the first IMF is very strong, this technique is particularly unstable for noisy signals with varying SNRs (Ayenu, 2010; Tang, 2010). To address this issue, the relevant modes are chosen based on the similarity between the probability density function (pdf) of the noisy signal and that of each IMF mode (Komaty, 2012,2014; Yang, 2015). However, if the hurst component of the Gaussian noise (fGn) approaches 1, this technique will fail. Qu et al. (2010) presented a unique EMD-based mode cell filtering (MCF) approach in which the threshold is determined by analyzing the statistical properties of the mode cell amplitudes using EMD. This strategy, however, fails to identify the appropriate, relevant modes; regardless of the EMD-based denoising method used, it is important to distinguish which IMFs are pure signal, pure noise, or contain both. Even though many methods have been proposed to identify the noisy IMF, the performance is unsatisfactory when these techniquesare directly applied to the weather signal denoising. Therefore, to resolve the problems associated with previous existing approaches, we modified the correlation-based EMD-IT approach based on the first and last IMF energy, which we named as the correlation based EMDIT energy constraints (CR-EMDIT-EC).

In comparison to earlier approaches, the accuracy and efficiency are enhanced. Recently, Ramyakrishna et al.(2022) applied higher-order spectral analysis on weather signals during a convective event to investigate how the bispectrum performed well under noisy conditions and showed significant improvement in the low signal-to-noise ratio (SNR) conditions.

Nowadays, the Fourier-based approach has been extensively used to analyse the random processes. But the main limitation of these methods is that it is based on the assumption of linearity and stationarity. EMD is an adaptive time-frequency data analysis method that decompose the data into a number of Intrinsic Mode Functions (IMFs) along with a residue component. The EMD can reveal important characteristics of the waves with a few IMF components. The pulse pair processing method degrades significantly at low SNR conditions and produces biased estimates in the presence of clutter regions (Doviak, 1984).

In this paper, we made an attempt to develop a denoising and clutter removal algorithm for weather signals using the EMD method, which is simple and easy to implement. This method significantly recovers the signal from clutter and noisy conditions. This method will check the presence of clutter during the partial reconstruction based on the last IMF energy. In this method, we will check the correlation plot between the original signal with that of each IMF mode. Later we will identify the decreasing trend of the IMF from the first local maximum value of the last IMF that will be considered as the k_{th} mode. From the first IMF to k_{th} mode IMF will be considered as the useful modes, remaining IMFs will be considered as the relevant modes. Now reconstruct the signal with useful modes by discarding the relevant modes during partial reconstruction. In this paper, we use various Empirical Mode Decomposition denoising techniques based on threshold criteria on weather radar signals to check which method is efficient for denoising the weather signals and removing ground clutter.

5.2. A Brief Description of EMD

The EMD method is based on the assumption that all data consists of several simple intrinsic modes of oscillations which have a corresponding number of extrema and zero crossings. As far as the local mean is concerned, those oscillations will be symmetrical.

5.2.1. EMD Algorithm

The EMD decompose the signal into a number ' n' of IMF components.

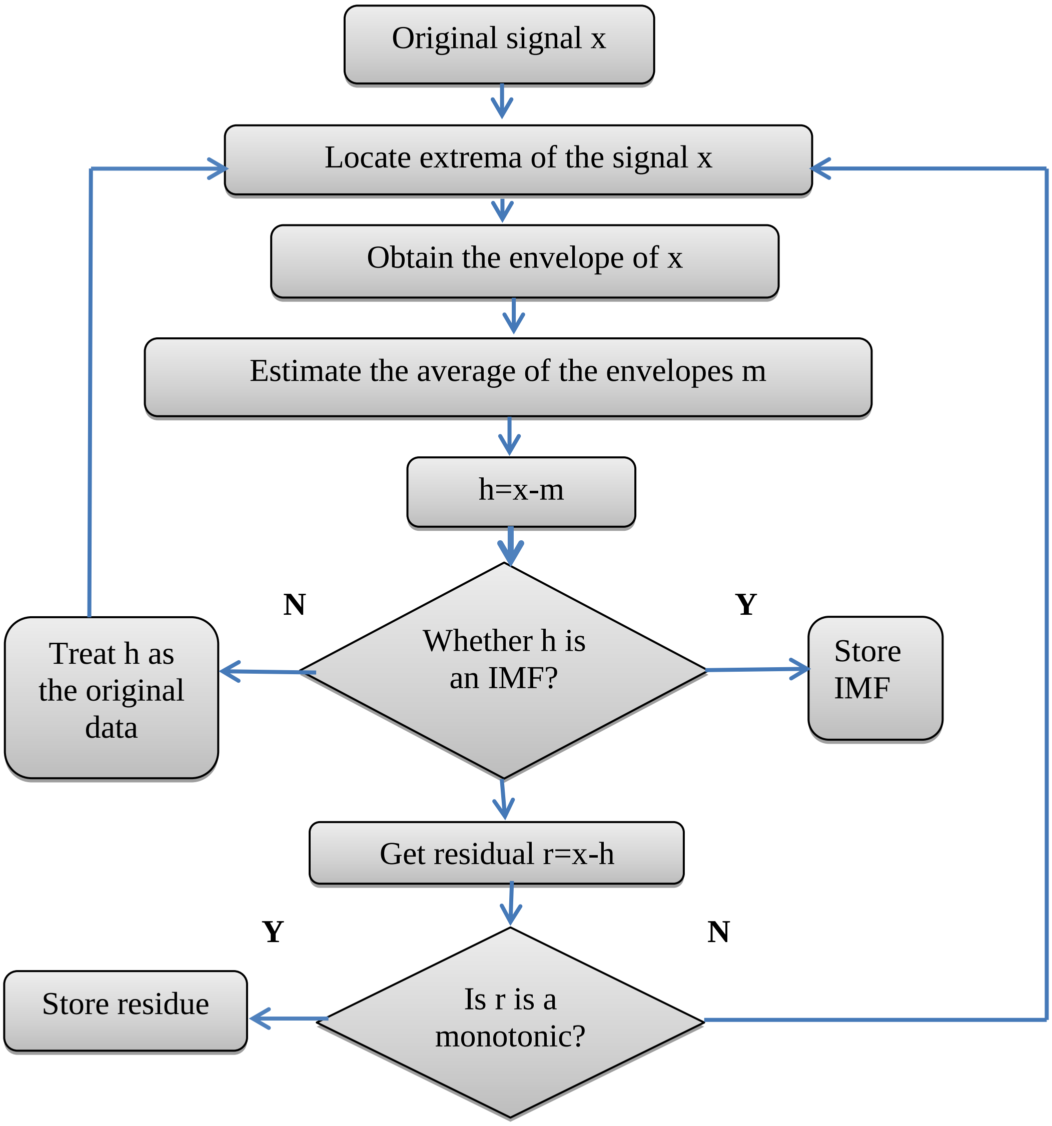

Fig. 5.1: Flow Chart diagram of Empirical Mode Decomposition

An IMF function satisfies two conditions (Huang., 1998).

1. In the whole data set, the number of extrema and zero crossings must either equal or differ by at most one.
2. The mean value of the envelope defined by the local maxima and the envelope defined by the local minima is zero at any point.

The first condition will be identical to that of the usual narrowband requirement for a static random process. The second condition is capable of changing the global requirement to local one. The local mean of the envelope is defined by the local maxima and the local minima to force the local symmetry. Fig.5.1 shows the flow chart of the EMD algorithm.

We briefly discussed the EMD algorithm (Rilling et al., 2003) in the following steps. Let us consider x(t) as a non-stationary signal.

1) Locate the local maxima and minima of the signal x(t) and get the upper envelope $x_u(t)$ and the lower envelope $x_l(t)$, respectively.
2) calculate the local mean value $M_1(t)=(x_u(t)+x_l(t))/2$ of data x(t), then remove the mean value from original signal x(t) and get the difference: $H_1(t)=x(t)-M_1(t)$.
3) Consider $H_1(t)$ to be a fresh dataset and repeat the above steps (1) and (2) for k number of times, $H_1k(t)=H_1(k-1)(t)-M_1(t)$, where $M_1k(t)$ is the mean value of $H_1(k-1)(t)$ and $H_1k(t)$.

   Step (3) is repeated until the resultant data meets the two requirements of an IMF, which are specified as $c_1(t)=H_1k$. The residual data $r_1(t)$ may be calculated as $r_1(t)= x(t)-c_1(t)$.
4) consider $r_1(t)$ as new dataset, and repeat the above steps (1-3) to extract all the IMFs. Now stop sifting process until the n^{th} residue $r_n(t)$ is smaller than a predetermined number, or the residue becomes monotonic.
5) The sifting process can be terminated based on Standard Deviation (STD), which can be calculated using the two successive sifting results provided in equation (5.1).

   $$\mathrm{STD}=\sum_{t=0}^{T}\frac{|H1(k-1)(t)-H1k(t)|^2}{H1^2(k-1)(t)} \qquad (5.1)$$
6) STD values ranges from 0.21 to 0.3.
7) Steps (1-4) should be repeated until the residual includes no relevant frequency information. The total of the original signal's IMFs equals the original signal. If we have 'n' IMFs and a final residual r_n (t), we may define the original signal x(t) as follows

   $$x(t)=\sum_{i=1}^{n} c_i + r_n \qquad (5.2)$$

EMD can be used as a denoising tool in various applications by knowing whether a specific IMF contains useful information or mostly noise. Therefore, significant IMF tests based on the statistical analysis of modes resulting from the decomposition of signals solely consisting of fractional and white Gaussian noise, respectively, were developed by both (Flandrin, 2005; Huang, 2005) and Wu et al.(2004). The above method separates the signal and noise, assuming that the first IMF always represents high-frequency composition and can be rejected during the reconstruction. But, if the signal is widespread in the observational bandwidth, there is a possibility that the signal also may get removed. That may lead to an incorrect estimation of signal parameters. Flandrin et al.(2004) show that, apart from the first IMF, which contains noise only, the IMF energies linearly decrease in a semilog diagram because of exhibiting self-similar characteristics (Kopsinis, June 2008).

Many studies have reported different denoising techniques in weather applications (Hildebrand et al., 1974; Ivic, 2010; Ivic, 2013; Lagha, 2013). The main reason to consider EMD denoising: To explore the effect of different thresholding techniques (EMD Interval Thresholding (IT), correlation-based EMD-IT, Iterative Interval Thresholding (IIT), and Adaptive thresholding based on 3σ criteria) on weather signals. These findings will help us to find the best thresholding-based EMD denoising technique to improve the detection of signals in noisy conditions.

5.3. Denoising based on IMF Thresholding

It was discovered that executing thresholding and locally eliminating the low-energy IMF parts regarded as noise was feasible to execute thresholding and locally eliminate the low-energy IMF parts regarded as noise, inspired by wavelet-based thresholding (Kopsinis, 2009, Aug 2008). EMD-DT is an application of direct wavelet thresholding to EMD denoising. This is followed by hard and soft thresholding operations, which keep signals that surpass the thresholding criterion. However, straight use of wavelet thresholding is, in principle, incorrect and may result in a discontinuity in the denoised signal. Unlike EMD-DT, EMD-IT performs the thresholding operation over the whole zero-crossing period, which overcomes the limitation of EMD-DT. The threshold level chosen has an impact on EMD's denoising capacity. The universal threshold is given by,

$$T_i = \sigma_i\sqrt{2\ln N} \qquad (5.3)$$

Where N is the data length, σ_i is the noise standard deviation, which can be obtained by using a robust estimate based on the IMFs' median, given by (Donoho, 1994)

$$\sigma_i = \frac{\text{median }(|h_i(n)|)}{0.6745} \quad , n=1,2,\ldots, N \qquad (5.4)$$

The power spectra of the remaining IMFs, except the initial noise-only IMF, show self-similarity features as a result of decomposition by EMD for additive white Gaussian noise. The energy of each E_i of each IMF decreases in a semilog manner as given by,

$$E_i = \frac{E_1^2}{\beta}\rho^{-i} \qquad i = 2,3, \ldots..L \tag{5.5}$$

Where E_1 is the energy of the first-order IMF and β, ρ is 0.7 and 2.01, respectively (Flandrin, 2004).

Based on the relationship between E_i and σ_i, T_i is given by,

$$T_i=\sigma_i\sqrt{2\ln N} = \sqrt{E_i\, 2\ln N} \qquad i=1,2\ ,3\ \ldots,\ L \tag{5.6}$$

The denoising using EMD in various applications is classified into two categories, based on relevant modes known as partial reconstruction using correlation coefficients and complete reconstruction without relevant modes based on filtered modes. In this paper, we used four methods to check the best performance of the denoising technique.

1. EMD Adaptive threshold based on 3σ criteria
2. EMD Interval threshold (EMDIT)
3. Correlation-based EMD Interval threshold (CR-EMDIT)
4. EMD Iterative interval threshold (EMD IIT)

5.3.1. EMD Adaptive threshold

The EMD adaptive threshold has been developed by Zhang et al. (2020)based on the 3 sigma (σ) criteria. This method will temporarily remove the non-noisy useful values in the IMFs that are larger than three-sigma. The remaining noise values are considered as the new 3 sigma, and this process will be repetitive until no values are removed. The last value of 3 sigma can be considered as a noise and can be used as a threshold and calculated adaptively for differentiating between actual signal and noise values. The procedure for the determination of the adaptive threshold method is as follows:

1.) Determine the IMF standard deviation:

$$\sigma_0 = \sqrt{\frac{1}{N-1}\sum_{n=1}^{N}\left(IMF(n) - \overline{IMF(n)}\right)^2} \tag{5.7}$$

2.) Discard the values larger than $3\sigma_0$ in $\mathrm{IMF(n)} - \overline{\mathrm{IMF(n)}}$. The remaining values can be considered as the new noisy signal $\mathrm{IMF}^1(\mathrm{n})$, with the length N_1.

3.) Determine the new noisy signal $\mathrm{IMF}^1(\mathrm{n})$ standard deviation.

$$\sigma_1 = \sqrt{\frac{1}{\mathrm{N}_1-1}\sum_{\mathrm{n}=1}^{\mathrm{N}_1}\left(\mathrm{IMF}^1(\mathrm{n}) - \overline{\mathrm{IMF}^1(\mathrm{n})}\right)^2} \tag{5.8}$$

4.) Finally, discard the values in $\mathrm{IMF}^{\mathrm{i}-1}(\mathrm{n}) - \overline{\mathrm{IMF}^{\mathrm{i}-1}(\mathrm{n})}$ that are larger than $3\sigma_{\mathrm{i}-1}$. Then again remaining values will be regarded as the new noisy signal $\mathrm{IMF}^{\mathrm{i}}(\mathrm{n})$, which has a length of N_{i}. The standard deviation of $\mathrm{IMF}^{\mathrm{i}}(\mathrm{n})$ is:

$$\sigma_{\mathrm{i}} = \sqrt{\frac{1}{\mathrm{N}_{\mathrm{i}}-1}\sum_{\mathrm{n}=1}^{\mathrm{N}_{\mathrm{i}}}\left(\mathrm{IMF}^{\mathrm{i}}(\mathrm{n}) - \overline{\mathrm{IMF}^{\mathrm{i}}(\mathrm{n})}\right)^2} \tag{5.9}$$

5.) Repeat the above step (4) until no value exceeds $3\sigma_{\mathrm{i}}$. Therefore $3\sigma_{\mathrm{i}}$ is the final threshold that can be denoted by the T.

$$\mathrm{T}=3\sigma_{\mathrm{i}} \tag{5.10}$$

6.) In this process, the value of 3σ in each step will decrease gradually.

5.3.2. EMD Interval Threshold (EMD-IT)

The intrinsic mode functions obtained from the EMD decomposition look like AM and FM sine waves with zero mean. Because of this property of the IMFs, the EMD-DT method produces discontinuities in the denoised signal (Hadjileontiadis, 2007). Therefore the amplitude of the IMFs does not provide information on whether IMF contains noise or signal. Only extreme point between specific zero crossing intervals can determine whether IMFs contains noise or signal. The extreme value will be below the predefined threshold if IMF contains only noise and vice versa. This method has applied a threshold on the zero crossing interval z_j^i and z_{j+1}^i; thus, it is called Interval thresholding.

The denoising method based on the extrema value in the corresponding interval is given by (Kopsinis, 2009, Aug 2008).

$$\hat{\mathrm{h}}^{i}\left(\mathrm{z}_{\mathrm{j}}^{\mathrm{i}}\right)=\begin{cases}\mathrm{h}^{\mathrm{i}}\left(\mathrm{z}_{\mathrm{j}}^{\mathrm{i}}\right), & \left|\mathrm{h}^{\mathrm{i}}\left(\mathrm{r}_{\mathrm{j}}^{\mathrm{i}}\right)\right| > \mathrm{T}_{\mathrm{i}}\\ 0, & \left|\mathrm{h}^{\mathrm{i}}\left(\mathrm{r}_{\mathrm{j}}^{\mathrm{i}}\right)\right| \leq \mathrm{T}_{\mathrm{i}}\end{cases} \tag{5.11}$$

For j=1, 2, 3,….., where $h^i\left(z_j^i\right)$ Indicates zero crossing interval samples from z_j^i and z_{j+1}^i of the ith IMF. The above equation resembles wavelet thresholding.

5.3.3 Correlation-based EMD Interval Threshold (EMD-IT)

This method selects relevant modes based on the correlation between the original signal and each mode. In this paper, we followed the approach of Zhang et al.(2015) for selecting the relevant modes.

Partial reconstruction of the signal using relevant modes is given by,

$$\tilde{x}(t) = \sum_{i=k_{th}}^{L} h^{(i)}(t) + r_L(t) \tag{5.12}$$

Here k_{th} can be determined by calculating the correlation between original signals and each IMF. $\tilde{x}(t)$can be rewritten as

$$\tilde{x}_m(t) = x(t) - \sum_{i=1}^{m} h^{(i)}(t) \tag{5.13}$$

Correlation between $x(t)$ and $\tilde{x}(t)$ is given by,

$$\rho(m) = \sum_{t=1}^{N} x(t)\, \tilde{x}_m(t) / \left(\sqrt{\sum_{t=1}^{N} x^2}\,(t)\sqrt{\sum_{t=1}^{N} \tilde{x}_m^2(t)}\right) \tag{5.14}$$

Where N is the length of the data, m is the one when $\rho(m)$ starts smaller than some constant C. C lies between [0.75, 0.85]. We used a C value of 0.80 in this paper [46]. The k_{th} is given by,

$$k_{th} = arg\,\mathrm{last}_{1 \le m \le L}\{\rho(m) > 0.8\} + 1 \tag{5.15}$$

Where "last" stands for the last value in $\rho(m)$ bigger than 0.8. However, this method is sensitive to noisy signals with different SNR conditions; this is one of the limitations of this method.

5.3.4. EMD Iterative Interval Threshold (EMD-IIT)

This method was inspired by the translation invariant wavelet thresholding method (Kopsinis, Aug 2008).

This method is summarized as follows.

1. Apply the EMD decomposition method on the original signal x, which contains noise.

2. Then reconstruct the signal by using the partial reconstruction method followed by Kopsinis(2009)approach.

3. Alter the sample positions of the first IMF randomly.

4. Construct a different noisy version of the original signal.

5. Apply EMD on the new altered signals.

6. Perform the EMD interval threshold on the IMFs to obtain the denoised version of thesignal $\tilde{x}_1(t)$ of the original signal.

7. Repeat the above 3-6 steps K-1 times, where K is the number of averaging iterations to obtain the k-denoised versions of x, i.e., $\tilde{x}_1$,$\tilde{x}_2 \ldots . \tilde{x}_{K.}$

8. Finally, take the mean of the denoised the signals

$$\tilde{x}(t) = \frac{1}{K}\sum_{k=1}^{K} \tilde{x}_k(t) \tag{5.16}$$

5.4. Limitations of Existing EMD denoising Techniques

Since threshold based method depends on the energy of the first IMF, assuming that the first IMF contains most of the noise energy. But in real-time applications, this assumption may not be valid. We observed from the correlation plots that in some cases, the first IMF strongly correlates with the original signal (as shown in Fig.5.2). Therefore, thresholding the first IMF using the above techniques may lead to losing the information of the signal. Therefore we should be careful, particularly in the case of the first IMF, when it strongly correlates with the signal information. The above methods will not be valid for denoising. In this paper, we discussed the limitations of the existing approaches and the advantages of the new approach clearly through simulation analysis.

5.5. Proposed Method (Correlation-based EMDIT energy constraints)

In this paper, we modified the existing correlation-based EMD Interval thresholding approach based on the energy of the first and last IMF. The required steps of the proposed method are described in detail as follows,

1. Apply the EMD decomposition method on the original signal x, which contains noise and clutter.

2. To identify the clutter, check whether the last IMF strongly correlates with the original signal (this can be easily identified from the correlation plot if there is a rapid increase in the correlation of the last 2 IMFs). If the last IMF has a strong correlation, then check for the k_{th} mode, which is a decreasing trend of IMF from the first local maximum value of the last IMF. From the first IMF to the k_{th} mode, IMF will be considered as useful, and the remaining IMFs will be considered as relevant modes.Then we can discard the relevant modes for clutter removal. Then the partial reconstructed signal is given by

$$x(t) = \frac{1}{K}\sum_{k=1}^{k_{th}} x_k(t) \tag{5.17}$$

3. Apply EMD–IT to all IMFs (If the correlation of the original signal with the first IMF is greater than all other IMFs),

$$\hat{h}^{i}(z_j^i) = \begin{cases} h^i(z_j^i), & |h^i(r_j^i)| > T_i \\ 0, & |h^i(r_j^i)| \leq T_i \end{cases} \qquad \text{for } i=2,3\ldots, N \tag{5.18}$$

Otherwise,

$$\hat{h}^{i}(z_j^i) = \begin{cases} h^i(z_j^i), & |h^i(r_j^i)| > T_i \\ 0, & |h^i(r_j^i)| \leq T_i \end{cases} \qquad \text{for } i=1, 2, 3,\ldots, N \tag{5.19}$$

The advantage of the proposed EMD denoising approach is that it significantly removes the noise components and ground clutter. This method effectively works for weather signals. We checked the efficiency of this approach through simulation analysis and real data analysis.

5.6. Simulation analysis of Weather signal denoising using EMD

5.6.1. Signals with Noise Simulation Analysis

A simulation study of weather signals has been conducted to perform EMD denoising on weather signals and how these methods perform well under noise-varying conditions. Simulation with the realization of weather signals having different SNRs has been performed. A Gaussian Model of Doppler power spectra have been considered for this analysis and generated the time series of complex-valued weather signals using Zrnic et al. (1975)

approach with different SNR conditions. The power spectrum of weather signals can be modelled by using Gaussian Model.

$$S(f)=\frac{P}{\sigma_f sqrt(2*pi)} exp\left[-\frac{(f-f_d)^2}{2\sigma_f{}^2}\right] \qquad (5.20)$$

Where P is the total signal power, σ_f and fare the spectrum width and mean velocity, and f_d is the Doppler shift.

In this section, a known Gaussian power spectrum model in each realization is simulated with a 1000 realization process and simulated weather echoes by the procedures Zrnic et al., 1975, which are used as the input of the proposed method. Calculated the velocity and spectrum width using both various denoising methods using EMD and Fourier method, also calculated Root Mean Square Error (RMSE) to verify the advantage of the proposed EMD denoising method. At last, the real-time series obtained from the Doppler weather radar has been considered for EMD analysis to verify its performance.The values of SNR are 5, 7, 10, 17, and 25 dB considered for every 200 realizations, respectively. Five realizations are selected and applied to various denoising techniques for different SNRs.

Fig.5.2 shows the simulated power spectrum where the main peak is observed between 450-550 Hz. Fig.5.3(a)-5.3(b) shows the real and imaginary components of the IMFs observed in the time domain. Fig.5.4(a)-5.4(b) shows the power spectrum of corresponding IMFs. The power spectrum of the first IMF shows similar characteristics to the main signal, as shown in Fig.5.2. The EMD decomposes the signals from higher frequencies to lower frequencies. We assume that always the first IMF contains most of the noise information, but where in practical applications, it is not valid. Here, the first IMF exhibits the main signal characteristics with maximum amplitude, whereas the remaining IMFs have very less amplitude. Fig.5.5 shows a corresponding correlation between each IMF and the original signal. The first IMF has a strong correlation of almost 0.98, which means that the IMF has most of the signal information, whereas other IMFs correlate less than 0.2. Therefore first IMF is enough to reconstruct the whole signal.

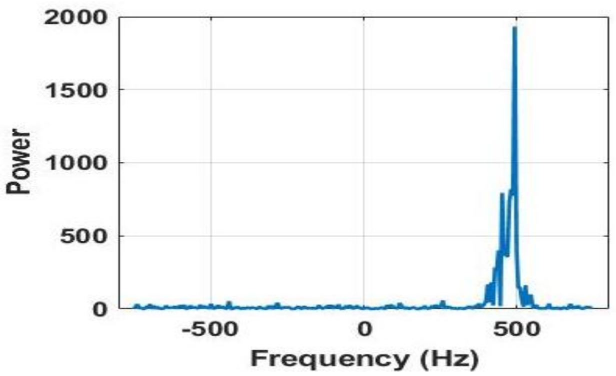

Fig.5.2: Simulated Power spectrum

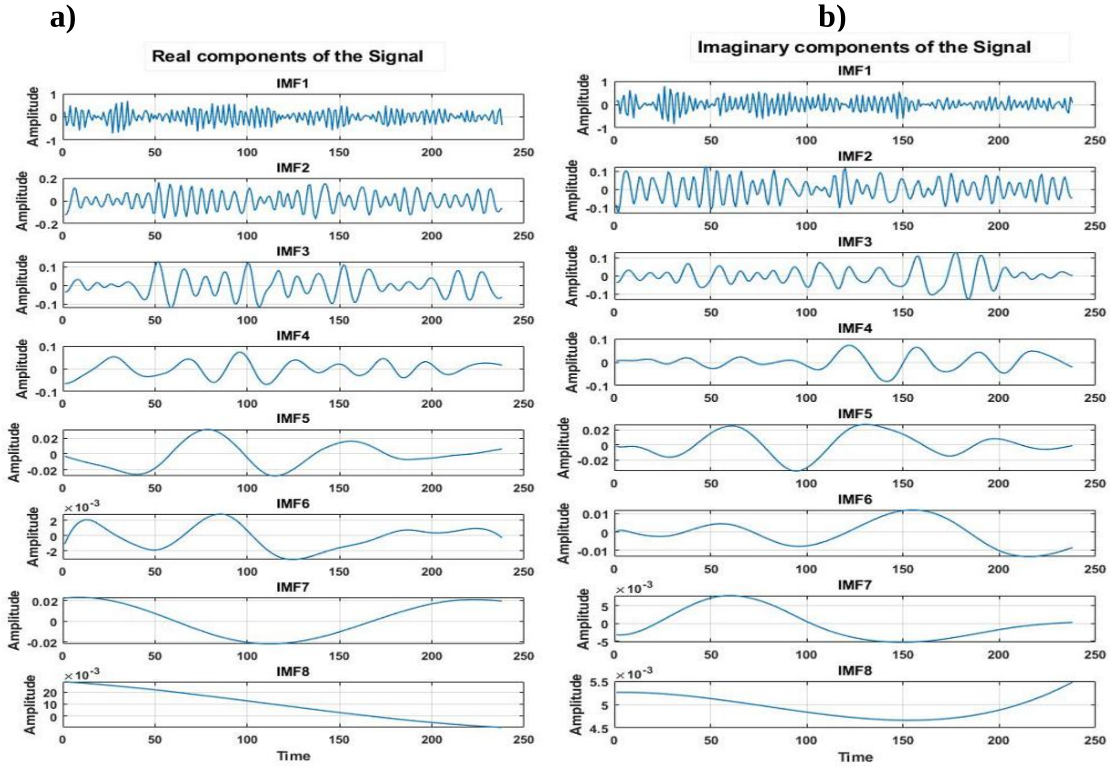

(a) **(b)**

Fig.5.3: a) Real and b) Imaginary parts of the IMFs of the simulated signal in time domain.

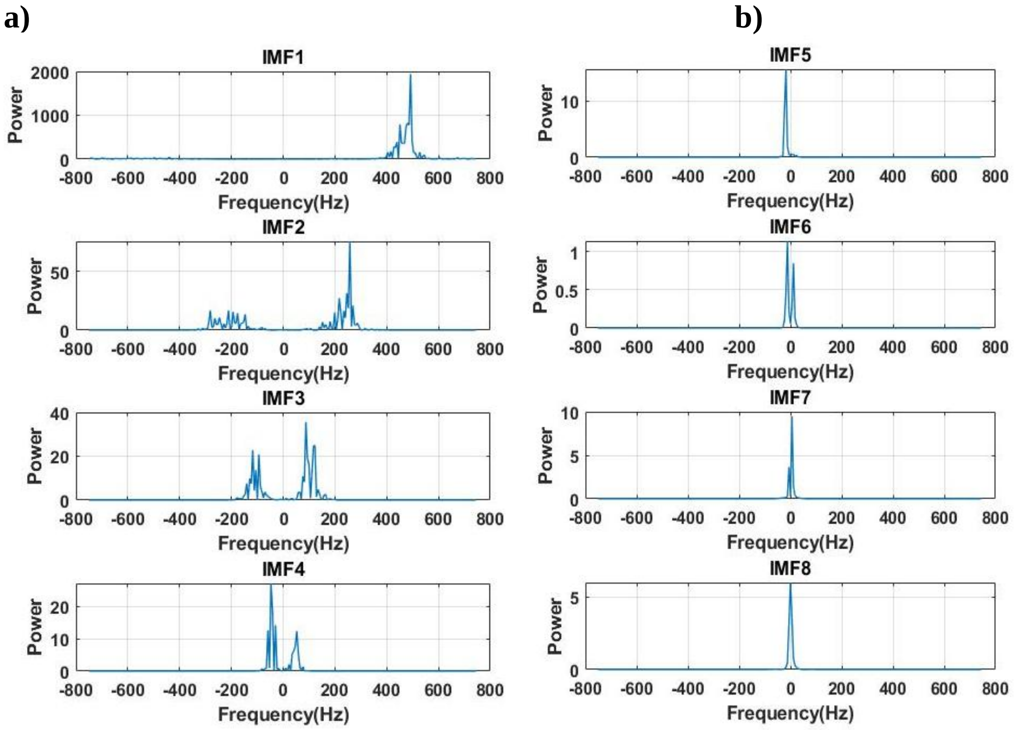

Fig.5.4: a) Real and b) Imaginary parts of IMFs in the spectral domain

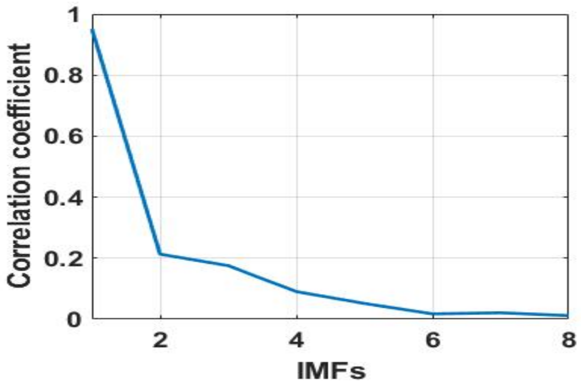

Fig. 5.5: Correlation plot between each decomposition mode (IMF) and the original signal.

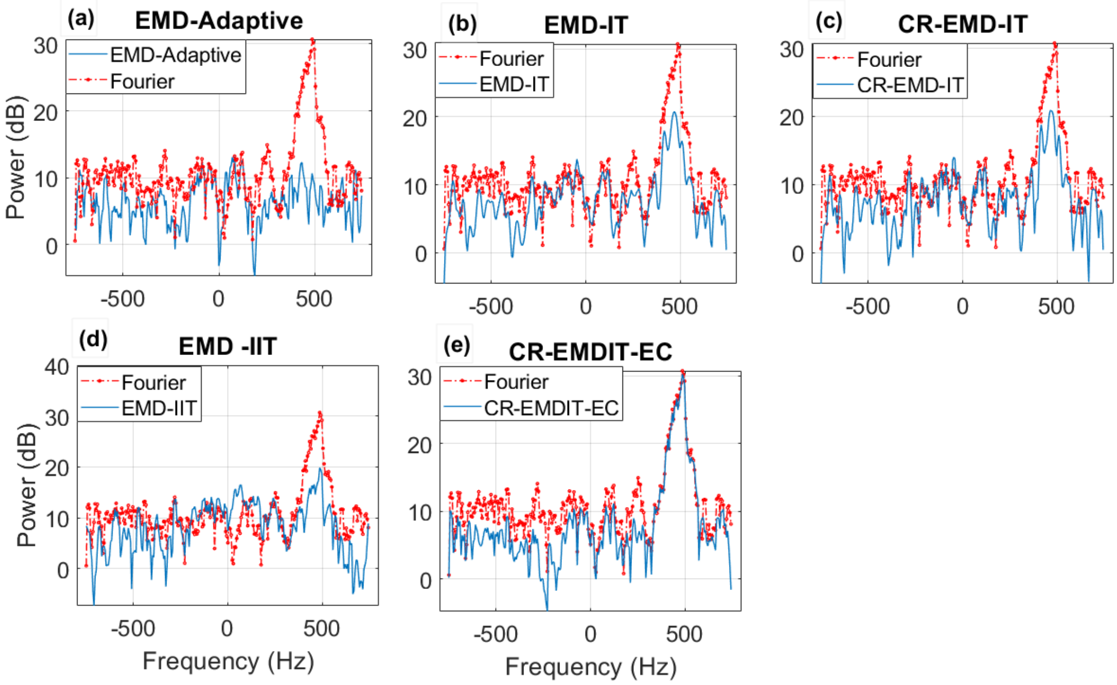

Fig 5.6: Power spectrum of the reconstructed signal obtained using various denoising techniques. Such as a) EMD-Adaptive, b) EMD-IT, c) Correlation-based EMD-IT, d) EMD Iterative Interval threshold and e) Proposed method (CR-EMDIT-EC).

Fig.5.6 shows the power spectrum obtained using different denoising methods (such as EMD-Adaptive, EMD-IT, correlation-based EMD-IT, EMD-IIT and CR-EMDIT-EC). We can observe from Fig. 5.6(a)-5.6(d) that the existing approaches consider the first IMF (which has most of the signal information) for thresholding, where most of the information of the signal has been lost and fail to reconstruct the whole signal. Fig.5.6(e) shows the result of the power spectrum obtained through the proposed method (without considering the first IMF for thresholding). We can see clearly that the proposed method significantly removed the noise components without disturbing the main signal information. Therefore before doing the EMD interval thresholding, first calculate the correlation of IMFs with its original signal; if the first IMF has a strong correlation with the signal, then the first IMF should not consider for thresholding.

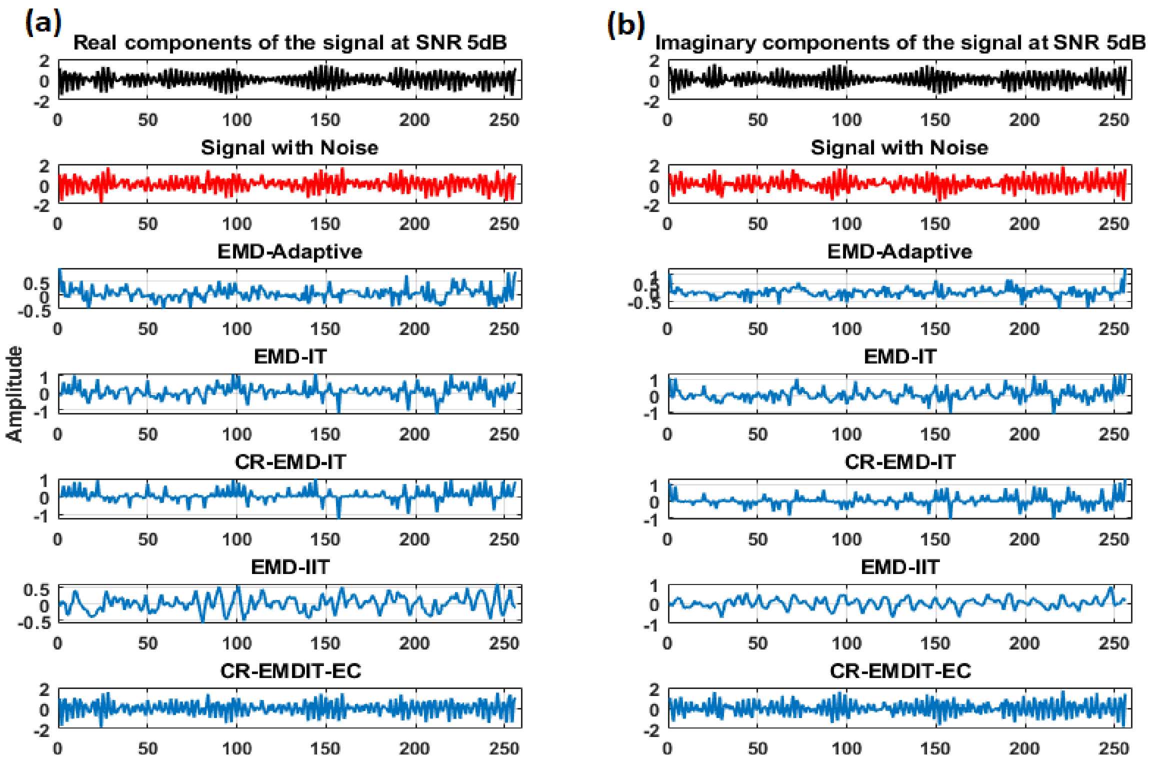

Fig. 5.7: Denoised versions of a) Real and b) Imaginary components of the signals using different EMD based denoising techniques and CR-EMDIT-EC with SNR of 5dB.

Fig. 5.7 shows the denoised version of the signals obtained from different EMD denoising techniques with the SNR of 5db. The noiseless signal has been shown by a black line, noisy signal, and reconstructed signal (using various denoising techniques such as EMD-Adaptive, EMD-IT, correlation-based EMD-IT (CREMDIT), EMD-IIT with 4 iterations, and CR-EMDIT-EC) have been shown by red and blue colour respectively.

It can be seen that the proposed method of CR-EMDIT-EC (Modified Correlation-based EMD Interval thresholding (IT)) has a better performance compared to the other methods, which significantly removes the noise components and reconstruct the signal without losing the signal information. The Velocity and Spectrum width with different SNR of five realizations is listed in Table 5.1.

Table 5.1: Values of velocity and spectrum width obtained from various EMD denoising techniques compared with the theoretical values.

	SNR(dB)					
Methods	Moments	5dB	7dB	10dB	17dB	25dB
EMD	Velocity (ms^{-1})	1.1331	1.1247	1.1124	1.1712	1.2186

Adaptive	Spectrum width(ms^{-1})	1.2014	1.3047	1.3521	1.4686	1.4852
EMDIT	Velocity(ms^{-1})	1.1430	1.1853	1.1710	1.1825	1.1907
	Spectrum width(ms^{-1})	1.6567	1.4287	1.4504	1.5003	1.5514
CREMDIT	Velocity(ms^{-1})	1.1424	1.1558	1.1924	1.1918	1.1910
	Spectrum width(ms^{-1})	1.5273	1.4709	1.3066	1.5238	1.5630
EMDIIT	Velocity(ms^{-1})	1.1460	1.1623	1.1910	1.1889	1.1900
	Spectrum width(ms^{-1})	1.5054	1.4839	1.5142	1.5536	1.5494
Proposed method	Velocity (ms^{-1})	1.1582	1.1711	1.1890	1.1895	1.1901
	Spectrum width(ms^{-1})	1.5050	1.5123	1.5102	1.5006	1.5308
Theoretical values	Velocity(ms^{-1})	1.19				
	Spectrum width(ms^{-1})	1.5				

The number of samples is 256, and the maximum unambiguous velocity is 12ms^{-1} with a number of realizations of R=1000.

To check the performance of the EMD denoising techniques, Root Mean Square Error (RMSE) has been estimated between true values and estimated values obtained from the various EMD denoising methods (as shown in Fig. 5.8), and it is given by,

$$RMSE = \sqrt{\frac{1}{N}\sum_{t=1}^{N}(x(t)-\tilde{x}(t))^2} \tag{5.21}$$

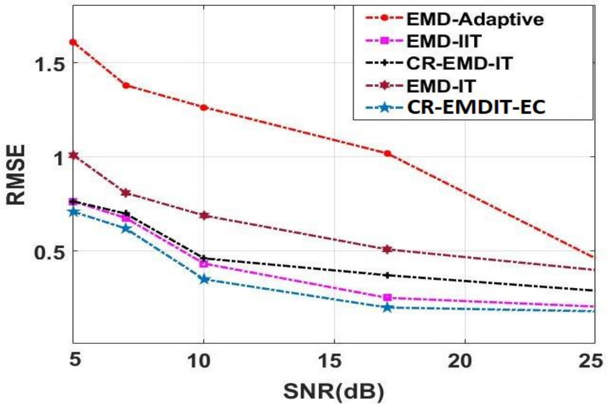

Fig.5.8: Root Mean Square Error (RMSE) plot between the true and estimated values obtained using various EMD denoising methods.

From Fig.5.8, it can be seen that the proposed approach (CR-EMDIT-EC) of EMD denoising performs better than other techniques; also, we can observe that the EMD-IIT threshold has a better performance. This is expected because of multiple iterations, but one of the limitations of EMD-IIT is more computational complexity compared to the existing methods. The adaptive method based on the 3 sigma threshold does not improve much in the low signal-to-noise ratio conditions.

5.6.2. Signals with Clutter Simulation Analysis

Both clutter and signals have been considered to model the power spectrum for the simulation of weather signals, followed by (Dong, 2022; Yu et al.,2009).

The power spectrum of weather signals can be modelled by using Gaussian Mixture Model (GMM) (Dong, 2022; Yu et al.,2009).

$$S(f)=\sum_{k=1}^{K}\frac{w_k P}{\sigma_{fk} sqrt(2*pi)} exp\left[-\frac{(f-f_k)^2}{2{\sigma_{fk}}^2}\right] \tag{5.22}$$

Where P is the total signal power, K is the number Gaussian shaped spectra contained in a power spectrum, w_k are the weighting coefficients ($0<w_k<1, \sum_{k=1}^{K} w_k = 1$), σ_{fk} and f_k are the spectrum width and mean velocity.

Fig.5.9(a)-5.9(b) shows the signal at 20-100 Hz and clutter at near zero frequency. These have been added, as shown in Fig.5.9(c) and considered for further analysis. Generally, the clutter is more dominant than precipitation with high reflectivity. Here we can see that clutter power is higher than the weather signal power. Therefore correlation plot in Fig. 5.9(d) shows the rapid change in correlation at the 6th and 7th IMFs. To identify the presence of the clutter, we need to identify the relevant modes to discard these IMFs during partial reconstruction. To do this, first check the k_{th} mode, which is the decreasing trend of the local maxima from the last IMF. Here we can see that the 6th IMF is the first local maximum, and the 5th IMF is the one which can be considered as k_{th} mode. The 6th and 7th IMFs are identified as relevant modes for discarding. Therefore, we can discard the 6th and 7th IMFs during partial reconstruction, producing clutter-free signals in the Doppler spectrum, and we can further proceed with the denoising analysis. Fig.5.10 shows the energy of each IMF mode in the spectral domain. Fig.5.11(a)-5.11(e) shows the power spectrum obtained through various EMD denoising techniques. We can observe that the existing approaches fail to reconstruct the signal in the presence clutter region; still, clutter peaks are discernible in the Doppler power spectrum, as shown in 5.11(a)-5.11(d). Correlation-based approaches (as shown in Fig.5.11(c) will consider the IMF with clutter information (which has a strong correlation) as a useful mode during reconstruction. This is the reason these approaches fail to give satisfactory results during reconstruction. Fig.5.11(e) shows the power spectrum obtained through a new method, which significantly removed the clutter signals and produced enhanced signal information capabilities.

Fig.5.12(a)-5.12(b) shows the power spectrum with signal and the power spectrum with clutter alone. These both have been added and produced the power spectrum that contains both clutter and signal, as shown in Fig.5.12(c). We can observe that clutter is more dominant than signal. The correlation plot in Fig.5.12(d) shows a high correlation at the 6th and 7th IMFs. The best way to differentiate between clutter and signal is by identifying the kth mode, which can be identified by the decreasing trend of IMF from the first local maximum of the last IMF using a correlation plot. Here 6th IMF is considered as the kth mode, as the 7th IMF has the first local maximum value and can be considered as the relevant mode. Therefore 7th IMF can be discarded during partial reconstruction, and the remaining IMFs can be considered for further denoising analysis. The IMF from where a rapid decrease in correlation after the first local maximum from the last IMF indicates the presence of clutter. Because the EMD decomposes the signal from higher frequency to lower frequency components, high-frequency components contain noise information, and low-frequency components contain clutter information. The correlation will be high for the last IMF (if clutter is present, then the correlation will be high at the final IMFs). To identify and remove the unwanted IMFs, the correlation will be helpful. This method is valid if there is no signal at higher IMFs (last IMF).

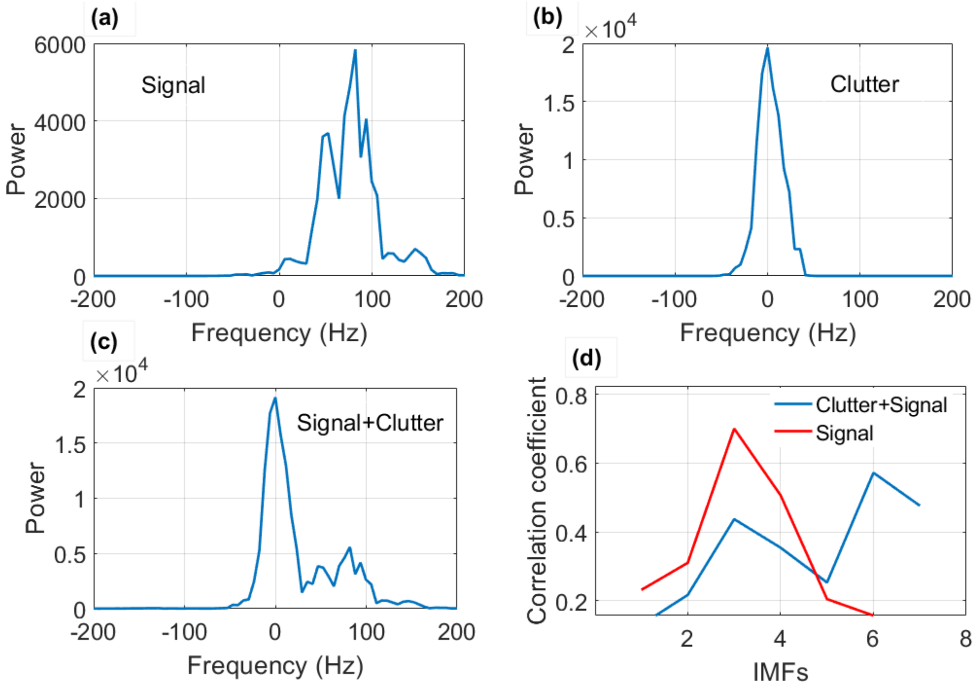

Fig. 5.9: Simulation of a) Signal alone b) Clutter alone c) Signal with Clutter using Dual Gaussian model using conventional method and EMD denoising at Doppler frequency 76.17Hz. and d) Correlation plot with and without clutter.

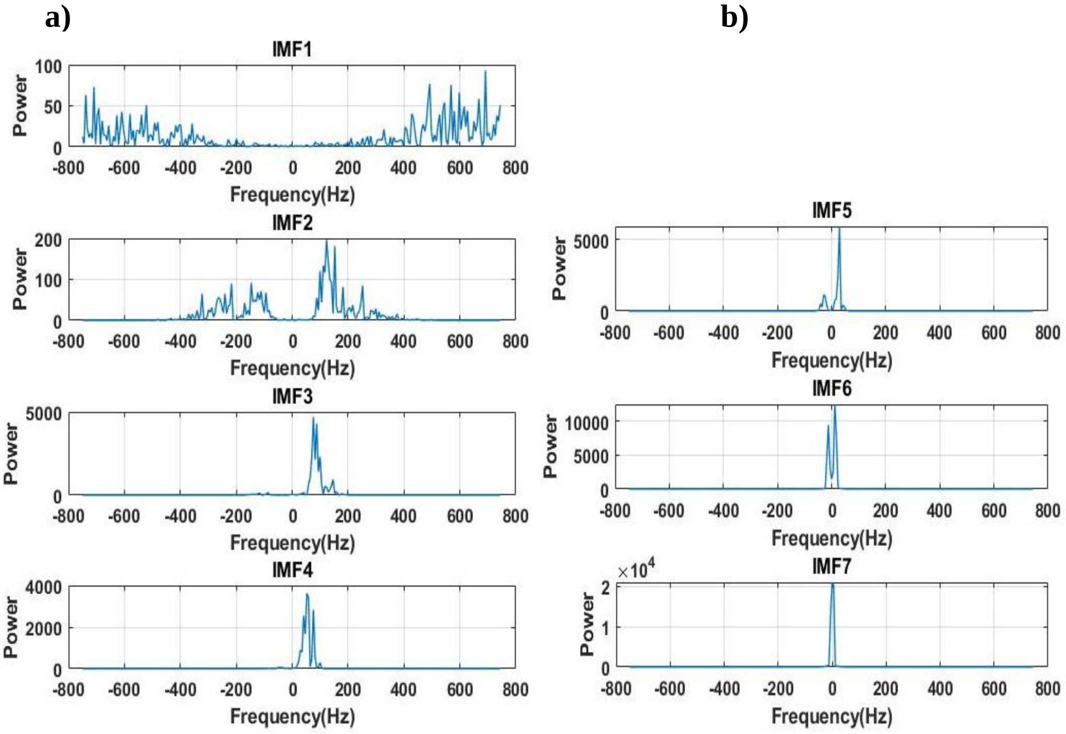

(a) **(b)**

Fig.5.10: The energy of each IMF in the spectral domain

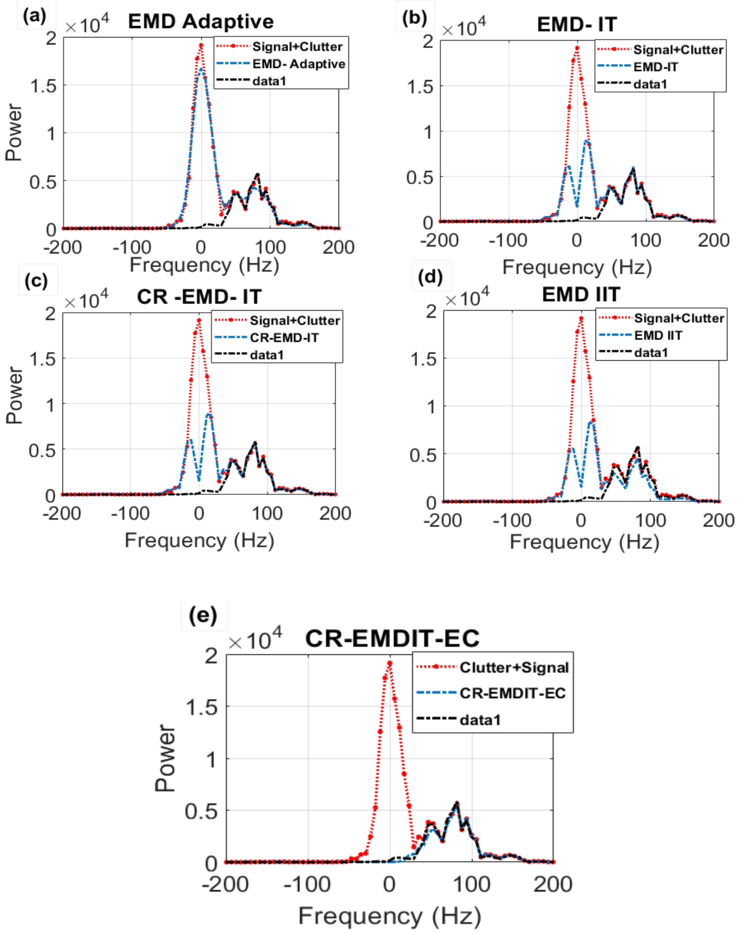

Fig.5.11: Reconstruction of the power spectrum using various EMD denoising techniques and a new approach.

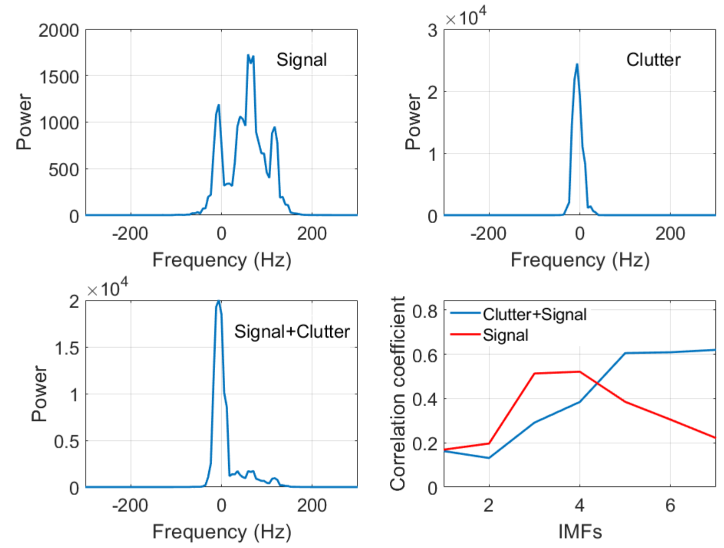

Fig.5.12: Simulation of a) Signal alone, b) Clutter alone, c) Signal with Clutter using Dual Gaussian model using conventional and EMD denoising at Doppler frequency 52.73Hz and d) Correlation plot with and without clutter.

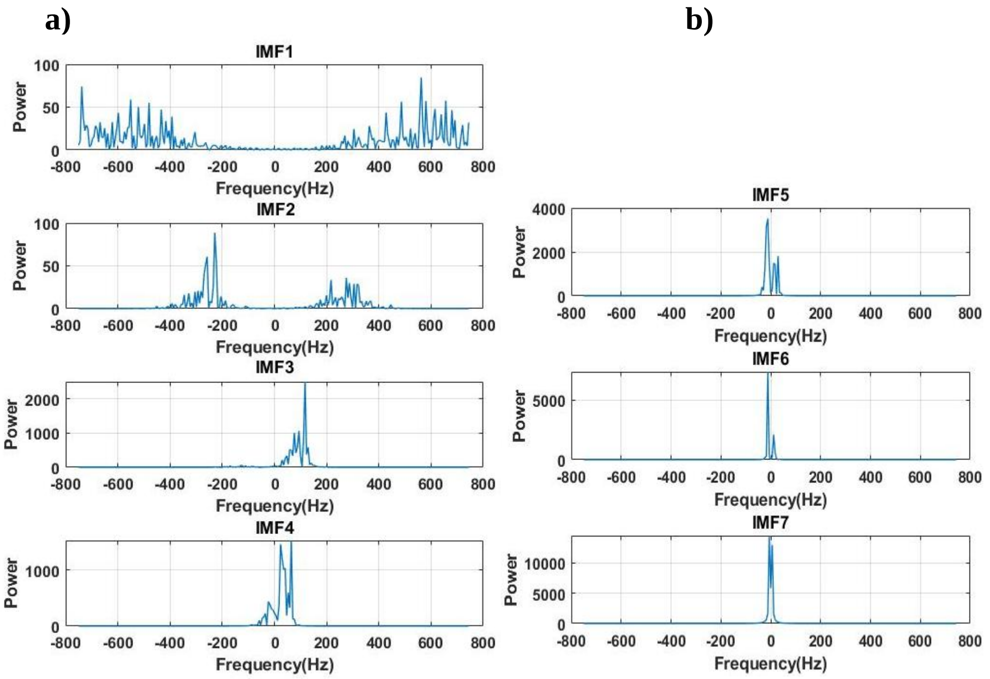

Fig.5.13: The energy of each IMF in the spectral domain

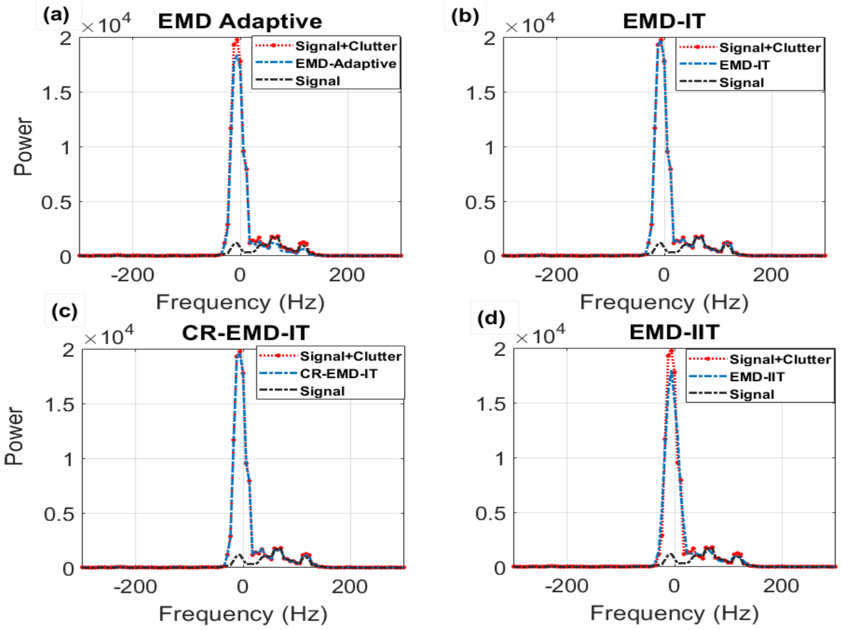

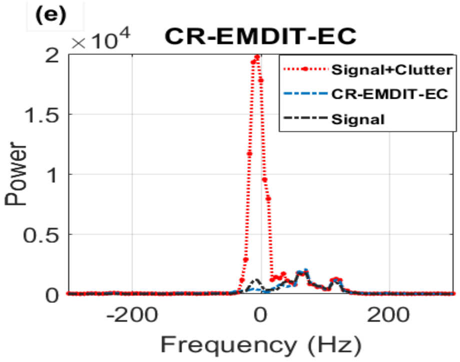

Fig.5.14: Reconstruction of the power spectrum using various denoising techniques and a new method.

Fig. 5.13 shows the energy of each IMF mode in the frequency domain. Fig.5.14(a)-5.14(e) shows the power spectrum obtained through various EMD denoising techniques. The existing approaches fail to reconstruct the signal in the presence of clutter region, as shown in 5.14(a)-5.14(d). Because these methods considered the IMF, which has a strong clutter of information, as a useful mode during reconstruction, this is the reason these approaches fail to give satisfactory results during reconstruction. Fig.5.14(e) shows the power spectrum obtained through a new method, which significantly removed noise components, and the clutter signals produced enhanced signal information capabilities.

5.7. Data Analysis

EMD-based denoising analysis has been applied to complex time series data of an X-band polarimetric Doppler weather radar located at Gadanki (13.5°N, 79.2°E) with a range resolution of 150 m and a sampling period of 1500 Hz. The backscattered signals are stored in the form of in-phase and quadrature-phase components. The complex time series data is subjected to Fourier and EMD analysis to obtain a Doppler power spectrum. A total of 238 samples were processed using a standard algorithm for deriving the power spectrum using Fourier and EMD-based denoising techniques.

5.8 Results and Discussions

To understand the performance of the EMD algorithms in the presence of noise and clutter regions. EMD algorithm has been applied to the weather signals observed from the Polarimetric X-band Doppler weather radar on 17th October 2019.

The First IMF is a high frequency component containing the most information about the noise and sometimes the signal parts. Therefore the noise fluctuations in the first IMF should be suppressed before reconstructing the signals. The presence of noise gives biased estimation and produces errors at the moment estimation. Fig.5.15 shows the sample power spectrum where the main peak is observed between 400-600 Hz. Fig.5.16 shows the corresponding power spectrum of IMFs. The first IMF power spectrum shows similar characteristics of the main signal with maximum amplitude, as shown in Fig.5.15. The EMD decomposes the signals from higher frequencies to lower frequencies. We assume that always the first IMF contains most of the noise information, but where in practical applications, it is not valid. Here it can be seen that the first IMF exhibits the main signal characteristics with maximum amplitude, whereas the remaining IMFs have very less amplitude. Fig.5.17 shows a corresponding correlation between IMFs and their original signal. The first IMF has a correlation of almost 99%, which means that the IMF has most of the signal information, whereas other IMFs correlate less than 10%. Therefore first IMF is enough to reconstruct the whole signal.

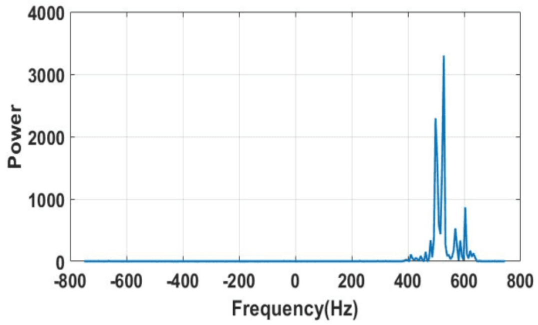

Fig. 5.15: Sample Doppler power spectrum of single range bin.

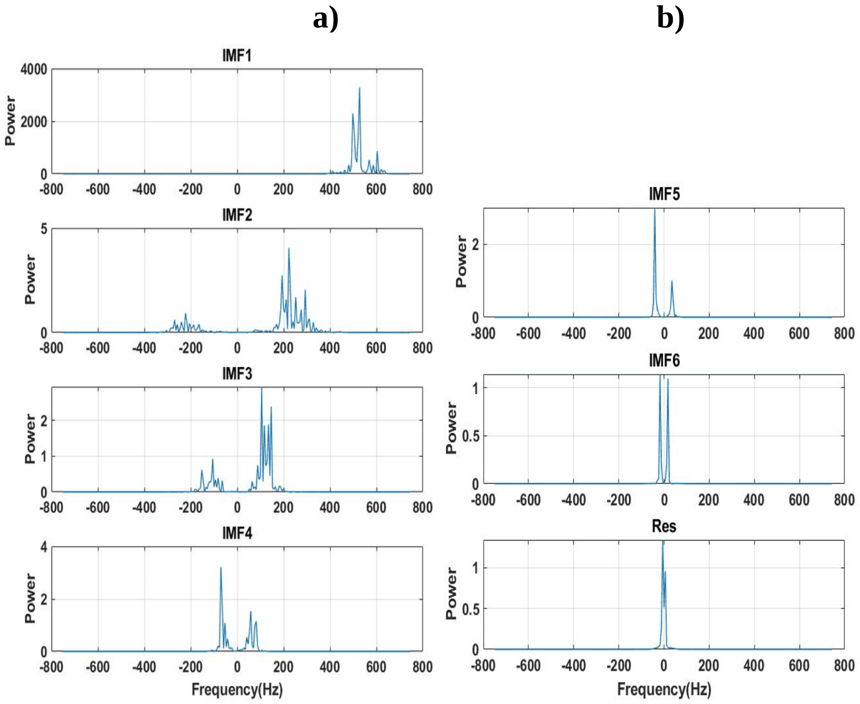

Fig.5.16: The energy of each IMF in spectral domain

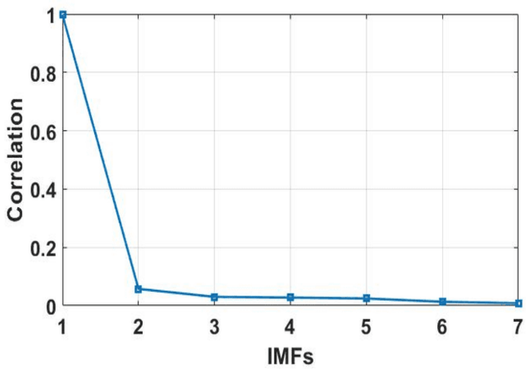

Fig.5.17: Curve of Correlation versus IMFs of a signal

Fig.5.18 shows the results of the power spectrum obtained through Fourier and EMD-based denoising techniques such as EMD-Adaptive, EMD-IT, correlation-based EMD-IT, EMD-IIT with 4 iterations and the CR-EMDIT-EC. Compared to other techniques proposed method (CR-EMDIT-EC) produced the enhanced denoising capabilities of EMD.

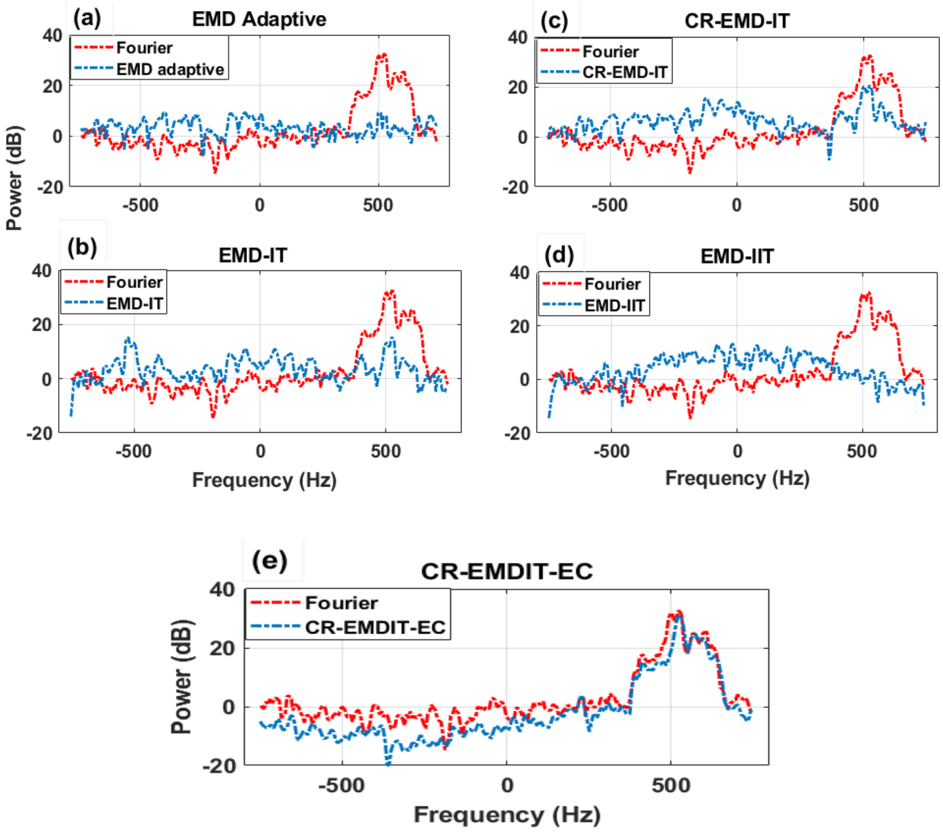

Fig.5.18: Power spectrum of EMD-based denoising results of the signals compared with the Fourier-based method using a.)EMD-Adaptive, b.)EMD-IT, c.)Correlation-based EMD-IT, d.)EMD-IIT and e.)CR-EMDIT-EC.

Fig.5.19 shows the results of the Power spectrum obtained through Fourier and EMD-based denoising techniques EMD-Adaptive, EMD-IT, correlation-based EMD-IT, EMD-IIT and CR-EMDIT-EC for fewer range bins. We can observe that the Proposed approach produced enhanced denoising capabilities of EMD compared to the other denoising techniques. Even though EMD-IIT performed well compared to the existing approach, its computational complexity is higher than other techniques and fails to give satisfactory results, especially when first and last IMF have strong energy.

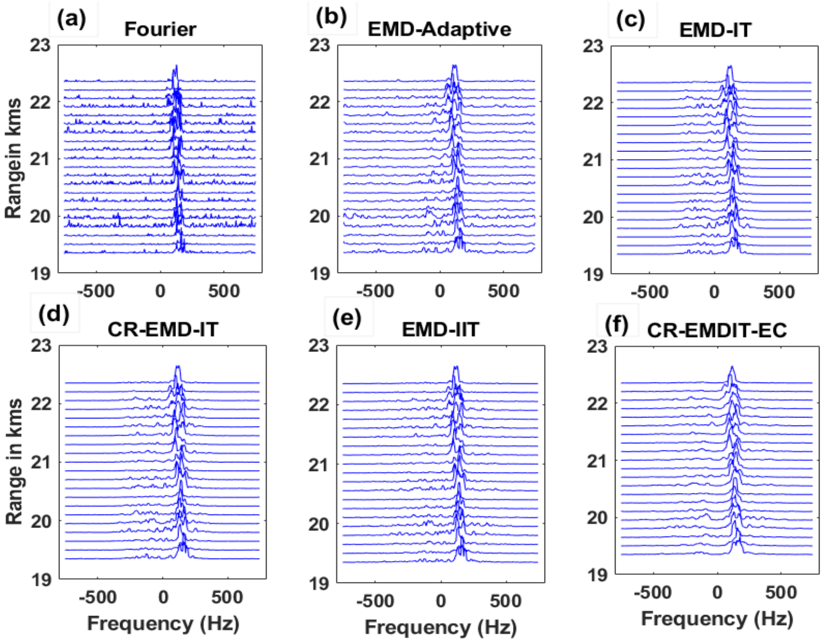

Fig.5.19: Power spectrum of EMD-based denoising results of the signals for few range bins compared with the Fourier-based method, EMD-Adaptive Threshold technique, EMD-IT, Correlation-based EMD-IT, EMD-IIT using 4 iterations and CR-EMDIT-EC.

Fig. 5.22-5.23 shows the range profiles of power, velocity, and spectrum width obtained from the EMD Adaptive, EMD-IT, Correlation-based EMD-IT, EMD-IIT, and CR-EMDIT-EC. These moments obtained from EMD denoising techniques have been compared with those obtained from the pulse pair processing. From the results, it can be observed that the proposed method has a better performance compared to other techniques. The adaptive method based on the 3sigma threshold did not improve the velocity plot much and produced severely biased moments estimation. Fig 5.24(a)-5.24(b) shows the range profiles of SNR computed from Fourier and EMD-adaptive based on 3sigma, EMD-IT, Correlation-based EMD-IT, EMD-IIT and proposed method. It can be observed that there is a slight improvement in SNR when using the proposed approach compared to the other methods.

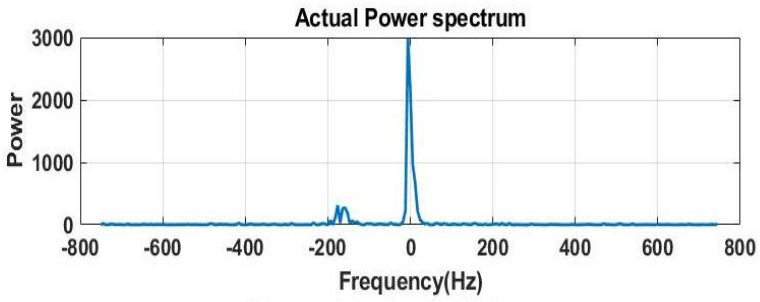

Fig. 5.20: Power spectrum of single range bin

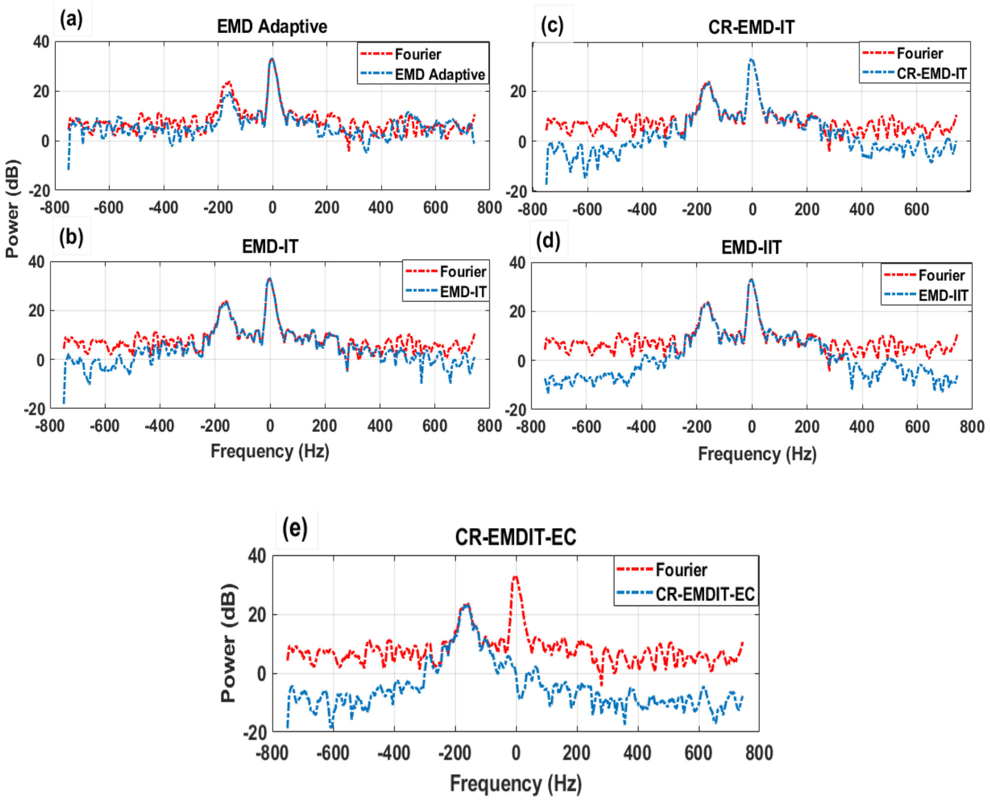

Fig.5.21: Power spectrum of EMD-based denoising results of the signals compared with the Fourier-based method using EMD-Adaptive, EMD-IT, Correlation-based EMD-IT, EMD-IIT and Proposed approach (CR-EMDIT-EC).

Fig.5.20 shows the power spectrum, which contains strong clutter near zero frequency and weather signal at -200 Hz. Fig.5.21(a)-5.21(e) shows the results of the Power spectrum obtained through Fourier and various EMD-based denoising techniques and CR-EMDIT-EC. We can observe that the proposed approach significantly removed the clutter signals and noise fluctuations compared to the other EMD denoising techniques, as shown in Fig.5.21(e).

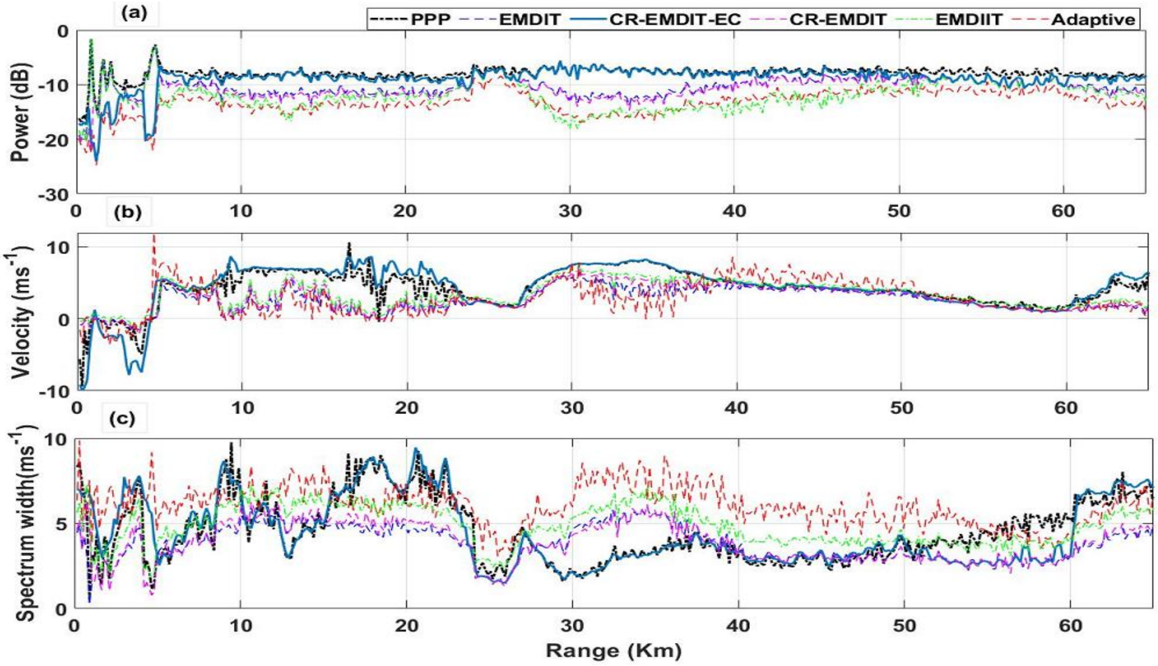

Fig.5.22: Range profiles of a) Power, b) Velocity, c) Spectrum width estimated through Pulse pair, EMD-adaptive based on 3sigma, EMD-IT, Correlation-based EMD-IT, EMD-IIT and proposed method obtained in Time domain processing. Azimuth: 90.

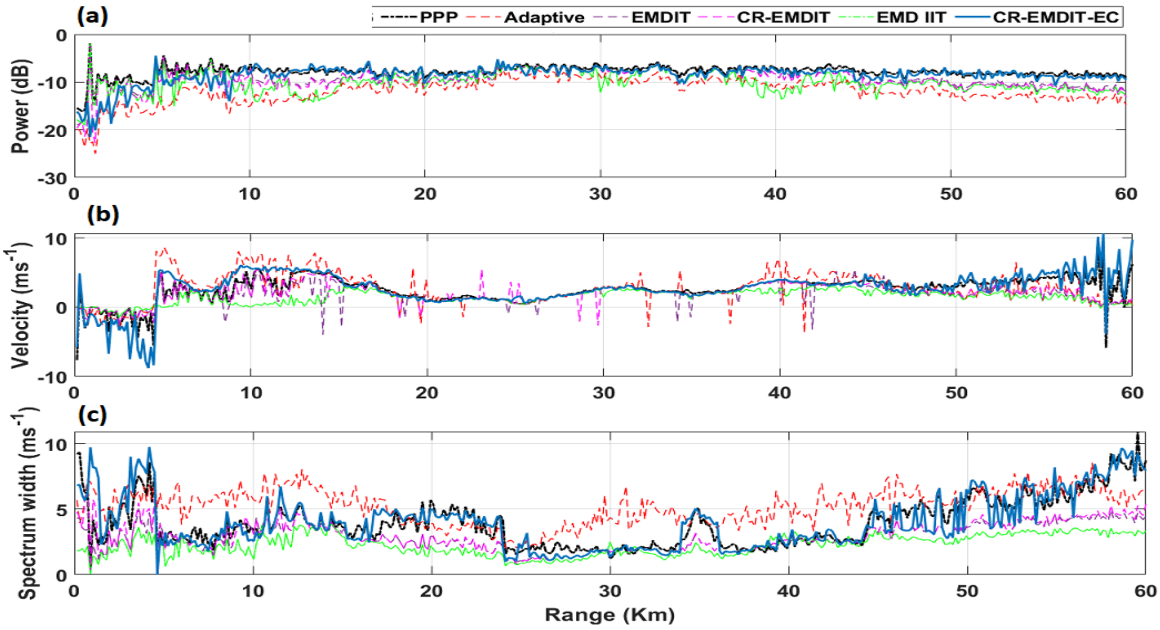

Fig.5.23: Range profiles of a) Power, b) Velocity, c) Spectrum width estimated through Pulse pair, EMD-adaptive based on 3sigma, EMD-IT, Correlation-based EMD-IT, EMD-IIT and proposed method obtained in Time domain processing. Azimuth: 60.

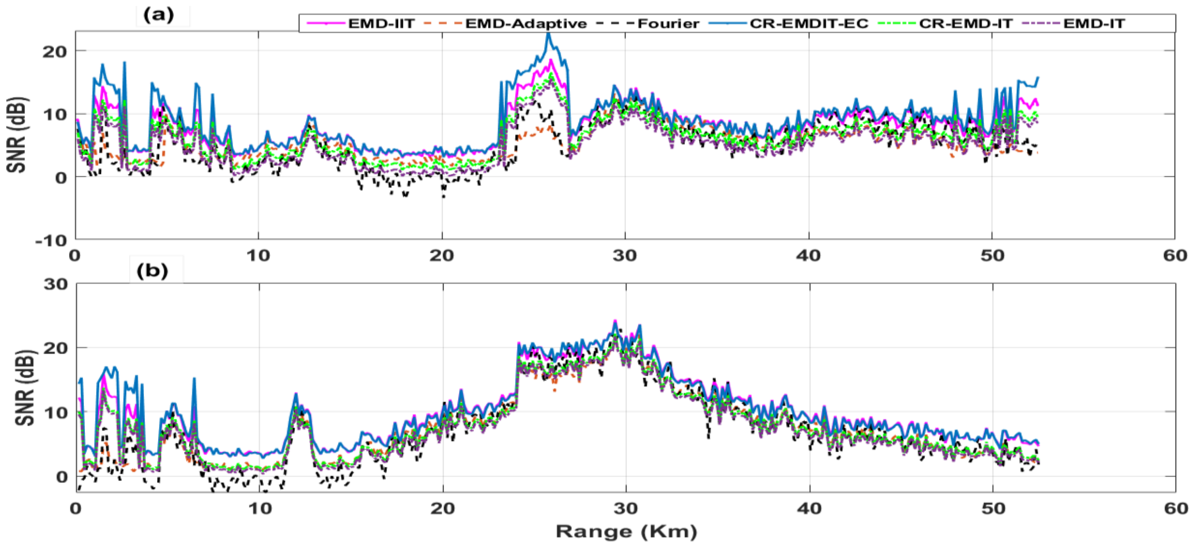

Fig.5.24: Range profiles of Signal to Noise ratio (SNR) obtained through Fourier, Correlation-based EMD-adaptive, EMD-IT, Correlation-based EMD-IT, EMD-IIT and proposed method a) Azimuth: 90 b) Azimuth: 60

To check the accuracy of the proposed method in the presence of clutter region, we compared it with the conventional moving average method.

Fig.5.25 shows the sample power spectrum obtained from both Fourier and EMD methods. It can be seen that the power spectrum obtained from the Fourier approach shows the presence of a DC component (due to ground clutter) near the zero frequency. The conventional method, like the 5-point or 3-point moving average method, removes the DC component by replacing the spectral power at zero frequency with the average of four adjacent points or 2 adjacent points. But in this case, it has been observed that the moving average method is not effectively working. It can be seen from Fig.5.25c EMD method effectively removes the DC component without disturbing the actual signal. The residue component obtained through EMD always contains the information of the DC component, which can be neglected during reconstruction. This is one of the advantages of the Empirical Mode Decomposition. Fig.5.26(a)-5.26(d) shows the Doppler profile obtained through the Fourier method and obtained through the EMD technique up to a range of 80km. It can be seen from Fig.26a-26d the proposed EMD denoising technique effectively works in the presence of ground clutter, as it is helpful to remove the ground clutter without disturbing signals present in that region.

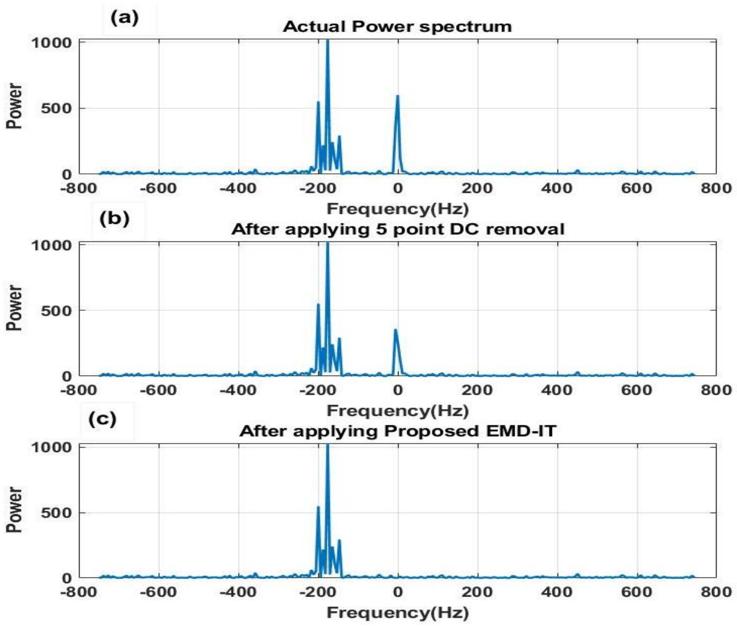

Fig.5.25: The sample Power spectrum obtained from both Fourier, conventional DC removal technique and Proposed method. a) rangebin: 25 b) rangebin:40

a)

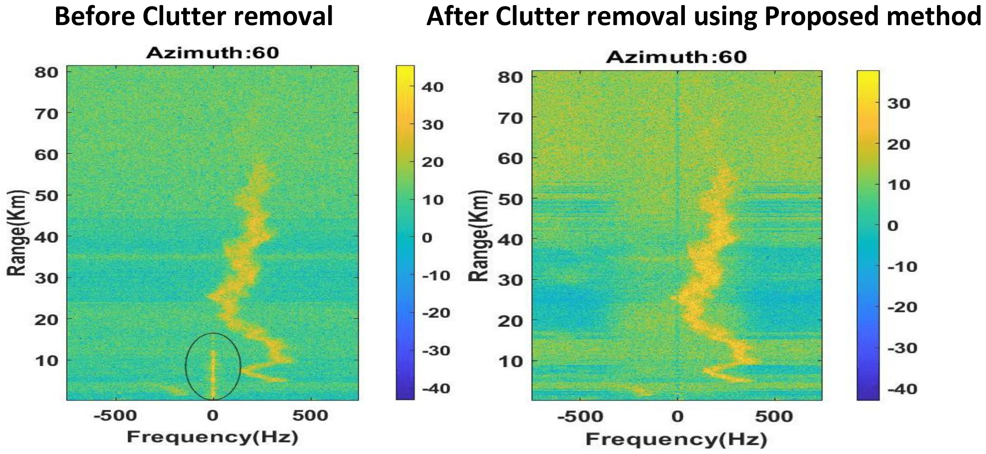

b)

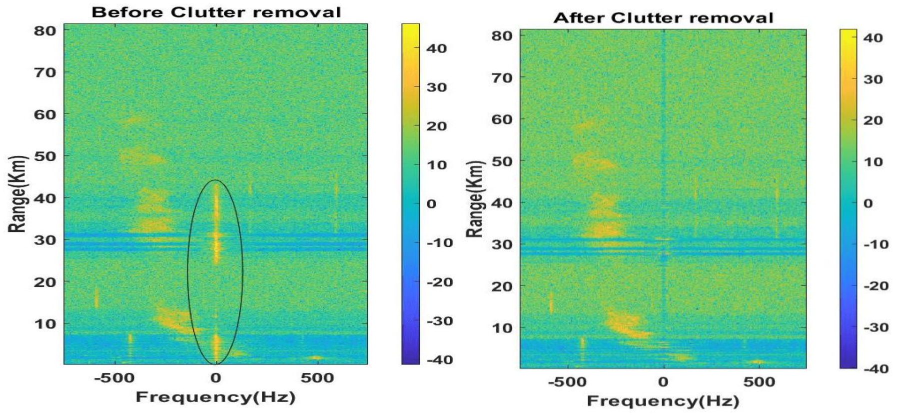

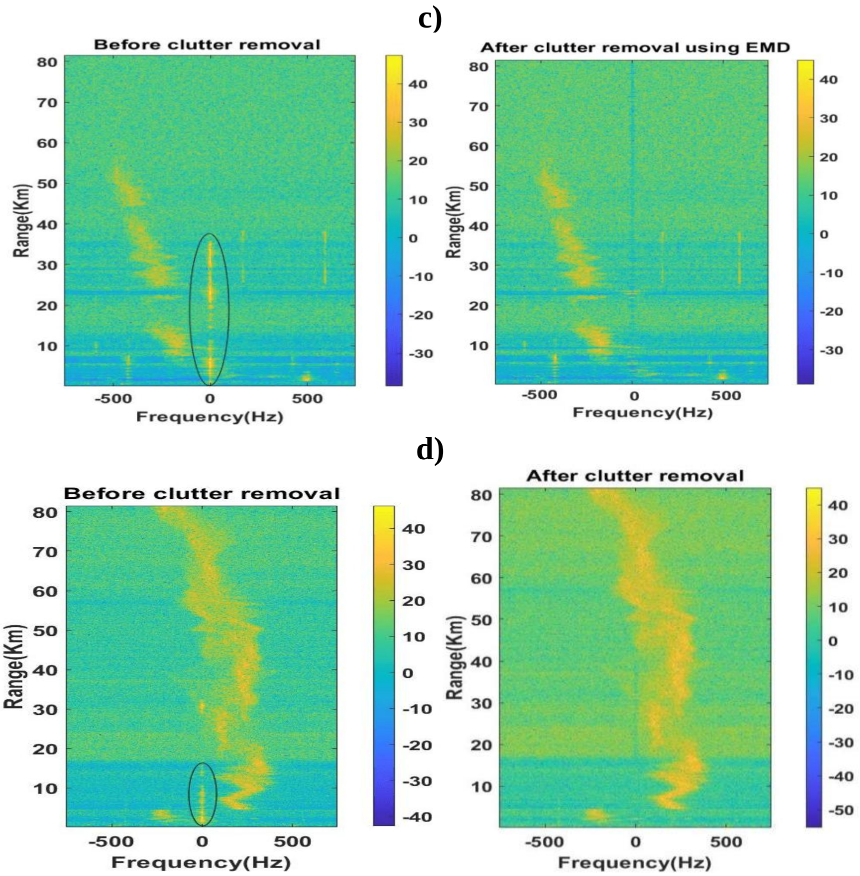

Fig.5.26: Doppler profile before and after clutter removal using EMD.

5.9 Chapter Conclusion

Various denoising techniques have been studied using the EMD approach on the weather radar signals to characterize and evaluate its performance. Even though the correlation-based EMD interval threshold method shows significant improvement in denoising the signal compared to the existing techniques, this approach fails during the reconstruction of IMFs when the first IMFs contain signal information and the last IMF contains strong clutter information than the signal. To overcome this problem, we modified the correlation-based approach with threshold criteria based on the energy of the first and last IMFs are integrated with the original analysis. The analysis is carried out with a large number of data sets, and it found that the new approach successfully removes the ground clutter and denoise the weather signal in all cases. The moment estimation and its comparison with other techniques demonstrate the effectiveness of the signal processing approach in a complex observational environment.

Chapter 6

Study of temperature sheets using Higher order spectral analysis

Prelude: This chapter discusses the existence of temperature sheets observed in the lower stratosphere up to 20km, with strong (positive) temperature gradients within very thin layers. These can be observed from vertical profiles obtained from the VHF radar. However, these sheets also formed in the troposphere and the middle stratosphere. The sheets tend to occur in groups and contribute to the regions of high static stability. To study the process associated with the formation of sheets, higher-order spectral analysis has been carried out on backscattered signals received from the MST radar.

6.1 Introduction

The two main echoing mechanisms for MST radar are Fresnel reflection/scattering from hydrostatically stable atmospheric areas and Bragg scattering as a result of variations in radio refractive index caused by clear air turbulence (CAT). For oblique beams, the radar echoes arise mainly because of CAT, which induces fluctuations in the radio refractive index. In contrast, for vertical beams, echoes are partly due to CAT and partly due to Fresnel reflection/scattering arising from sharp gradients in the radio refractivity index induced by stable layers.

Regarding scattering from the CAT induced refractive index fluctuations, radar echo power is directly proportional to the volume reflectivity, and turbulence intensity. Thus, high range and temporal resolution measurements of stable layers such as the tropopause or clear air turbulence are made possible by using VHF radars. It is still not possible to fully understand how these irregularities are created in different altitudes of the troposphere and low stratosphere.

In the tropopause region and lower stratosphere a number of multiple layer structures can be seen. These layers often called as sheets. It is shown that the key characteristics of multiple layers, which have been found at low altitude, are similar to those obtained at tropopause level.

The lowest altitude above 500mb level where the temperature lapse rate drops to 2K/km or less is the meteorological tropopause, which may be located using the radiosonde's measurement of air temperature. The average temperature lapse rate between this level to any level in the following two kilometres is 2K/km or less. Thus, comparing radar SNR measurements with radiosonde measurements would be interesting.

The specular form of echoes seen by VHF radar at vertical incidence come from areas with significant hydrostatic stability responsible for the intensity gradient in the radio refractive index. The atmospheric refractive index is given by,

$$M = -77.6 \times 10^{-6} \frac{P}{T} \frac{\partial ln\theta}{\partial z} \left[1 + \frac{15500q}{T} \times \left\{ 1 - \frac{1}{2} \left(\frac{\frac{\partial lnq}{\partial z}}{\frac{\partial ln\theta}{\partial z}} \right) \right\} \right] \tag{6.1}$$

$\frac{\partial ln\theta}{\partial z}$ is proportional to atmospheric stability.

Specular reflection; and Irregularities in anisotropic refractive indices are the two primary causes of aspect-sensitive radar backscatter.

The matter remains very controversial as to how these temperature sheets are generated; various authors have already discussed possible causes of these temperature sheets. Some research have suggested that Kelvin-Holm holtz instabilities (KHI) are the cause of this temperature differential. Wind shear causes the turbulence in a stable environment, which results in KHI. Strong gradients at the borders result from the turbulent layer being mixed.

Many experiments have reported the multiple layered structures at and around the tropopause regions, especially in the lower stratosphere. It is now well established that these layered structures are due to strongly negative and positive temperature gradients, commonly known as temperature sheets. As mentioned above, Fresnel reflection/scattering from stable layer structures is expected to cause the increased echo energy structures for vertical beams.

Experimental investigations confirmed that the parameter squared vertical gradient of potential refractive index M^2 (or squared Brunt Vaisala frequency (N^4) in the stratosphere) deduced from radiosonde measurements (such as pressure temperature, and humidity) replicated the backscattered received power at vertical incidence, showing a significant relationship between the vertical echo power and the medium's static stability. The correlation between vertical radar echo enhancement and temperature sheet position has been reported to be good. For example, it's striking that sheets with a horizontal echo enhancement look very much like those identified around the tropopause.

6.2.Generation of Temperature Sheets

A long time before the existence of these structures has been confirmed in the atmosphere, they were suggested to exist on temperature sheets that cause a partial reflection of electromagnetic waves. The statistical characteristics of the VHF radar echoes are responsible for balancing the generation and destruction of these structures. Additionally, it is incredibly interesting that the majority of the suggested generation mechanisms are likewise dependent on the action of turbulent mixing, despite the fact that the sole accessible destruction mechanism is diffusion (molecular or turbulent).

Nevertheless, a number of mechanisms do not directly result from turbulent mixing; nonlinear steeping gravity waves can cause temperature gradients as well. With the same period and at the same speed as the wave, these sheets will develop and spread. Viscosity or thermal conduction waves can also produce gradients in the temperature field (Hocking et al., 1991).

The beginning stage of a kelvin-Helmholtz billow growth is another process that might cause a high temperature gradient (Smyth, 2000). However, the sharp gradient is inextricably linked to a strong mixing zone that occurs nearby at the same height. It is also unknown if the created gradient would survive the billow's future evolution. In this situation, the sheet would be created and destroyed by the K-H billow.

Because of the existence of significant wind shear, the KHI is generated in the atmosphere. It is frequently observed during coastal front inversions, downslope win formations (Smyth,1991), and jet streams (VanZandt,1979). Several experimental and theoretical studies have also addressed the development, growth, and billow structure of the KHI, which are heavily influenced by the shear flow's Richardson (Ri) number. For Ri>0.25, the flows are unconditionally stable. Previous investigations using VHF radars suggest that KHI frequently occurs in the upper troposphere coupled with meteorological jet streams or at mesospheric heights (VanZandt, 1979).

Another mechanism suggested is irreversible modification of the temperature profile resulting from turbulence mixing, The primary feature of these mechanisms is that, on the boundary of a turbulence patch itself, temperature sheets are formed. (Coulman et al., 1995).

Specular reflectors in the stratosphere and mesosphere might be caused by viscosity and/or thermal conduction waves (Hocking, 1991). These waves would form as a result of partially reflected waves and gravity waves that become severely nonlinear and reach a critical point in time.

Direct observations of temperature sheets in the lower atmosphere and vertical echo power profiles at VHF clearly suggest that these structures contribute considerably near the zenith beams (Dalaudier et al., 1994; Luce et al., 1995). They demonstrated that the position of the chosen sheets closely correlate to the height of the enhanced vertical echo power.

6.3 Nonlinear Index from Bicoherence

The estimation of the nonlinear index from the Bicoherence is given by,

$$NLI = BIC^2_{max} - (\overline{BIC}^2_{robust} + 2\sigma_{BIC^2,robust}) \qquad (6.2)$$

Where $\overline{BIC}^2_{robust}$, $\sigma_{BIC^2,robust}$ are the robust mean and robust standard deviation, respectively. The term robust statistics refers to the measurements that are not affected by outliers in the data.

Nonlinearities can be identified and analyzed in the principal domain of Bicoherence (Peter et al., 2006; Jouny, 1992). The NLI is always less than or equal to zero for the linear signal process. For nonlinear signal processes, NLI is greater than zero.

6.4 Data Analysis and Method

6.4.1 MST radar

The MST radar is located at Gadanki (13.5^0N, 79.2^0E), Tirupati, operating in the VHF band (53MHz). This radar can detect the backscattering atmospheric echoes resulting from the small-scale inhomogeneities in the refractive index fluctuations due to variations in humidity and temperature. The data used in this analysis are collected during the clear air event (on 21 January 2023, between the period of 12:00 to 23:00 IST). Radar uses four obliques (off-vertical beams) and a vertical beam. The complete details of the system description and signal processing techniques can be found elsewhere (Rao et al., 1995). The analysis has been carried out in the height range of 3.6 to 20 km with 150 m vertical resolution along the beam direction. Experiments have been conducted in both vertical and off-vertical directions with a range resolution of 150 m. The backscattered echoes in time series are stored as in-phase and quadrature phases for offline processing.

6.5 Results and Discussions

Analysis has been carried out in many data sets for better understanding and quantifying the nonlinearities present in the temperature sheets. A clear air system was observed over the radar site on 21 January 2023 between the period of 12:00 to 23:00 IST.

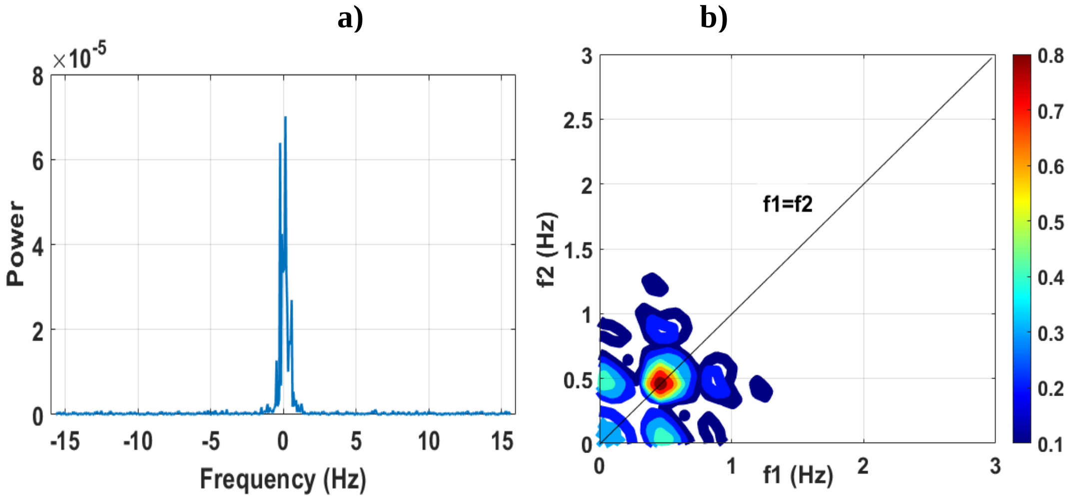

Fig. 6.1. a) Sample power spectra computed through FFT, and b) Bicoherence plot of the vertical beam on a clear air day (21 January 2023).

Fig. 6.1a shows the power spectrum obtained for one range bin (before the noise level estimation). The main atmospheric signal peak was observed from -1 to 1.5 Hz. Since atmospheric signals are contaminated with noise, and most of the time, its fluctuations influence the analysis. Sometimes, spurious peaks occur in the bicoherence plot due to noise in the signal; therefore, noise removal is an important part of signal processing to get the best estimation.

The noise level should be removed from the power spectrum to analyze nonlinear statistics in the signals. Fig. 6.1b.Shows the nonlinear interactions between frequency components in the principal domain of the Bicoherence plot. A maximum bicoherence value of 0.82 is observed at frequencies of (0.4587 Hz, 0.4587 Hz).

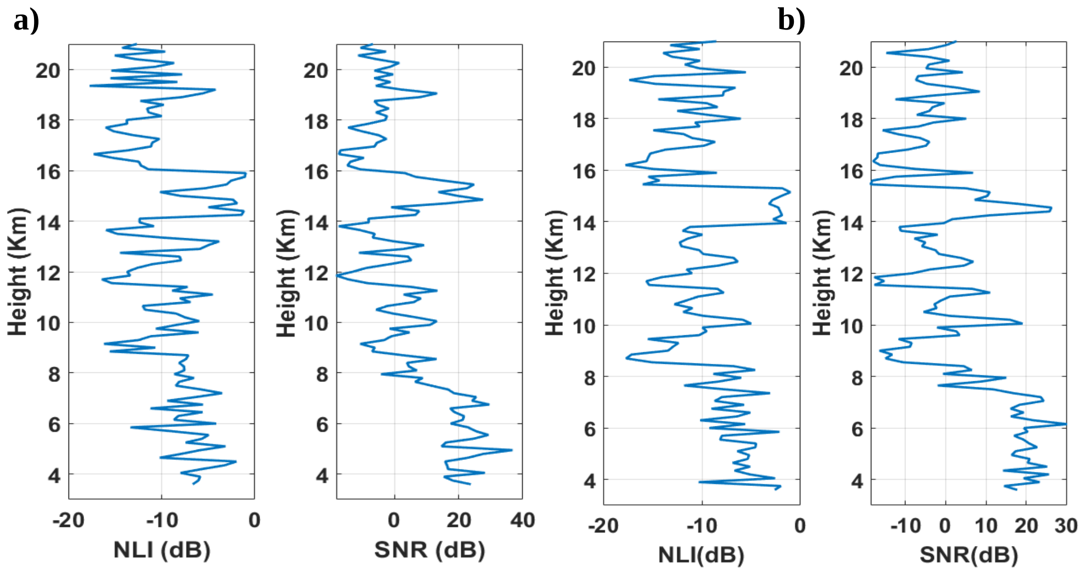

Fig. 6.2. Height profiles of Nonlinear index and SNR observed on a clear air day a) 129 rangebin b) 889 rangebin.

Fig. 6.2a-b shows the vertical profiles of nonlinear Index (NLI) and SNR plotted from 3-21 km observed during a clear air day. The maximum value of 28 dB SNR is estimated at 14-16 km height, as shown in Fig. 6.2a. This may be due to the presence of temperature sheets near the tropopause region associated with the wind shear mechanism. These sheets are commonly formed in regions of higher static stability (Luce, 2001; Jayarao, 1994; Lane et al., 2003; Trier et al., 2020; Sharman et al., 2012; Ko and Chun, 2019; He et al., 2022; Nath, 2009). It can be seen from NLI that a significant enhancement in the value of the nonlinear index is observed in the same region. The characteristic of this enhancement resembles that of temperature sheets that have been identified.

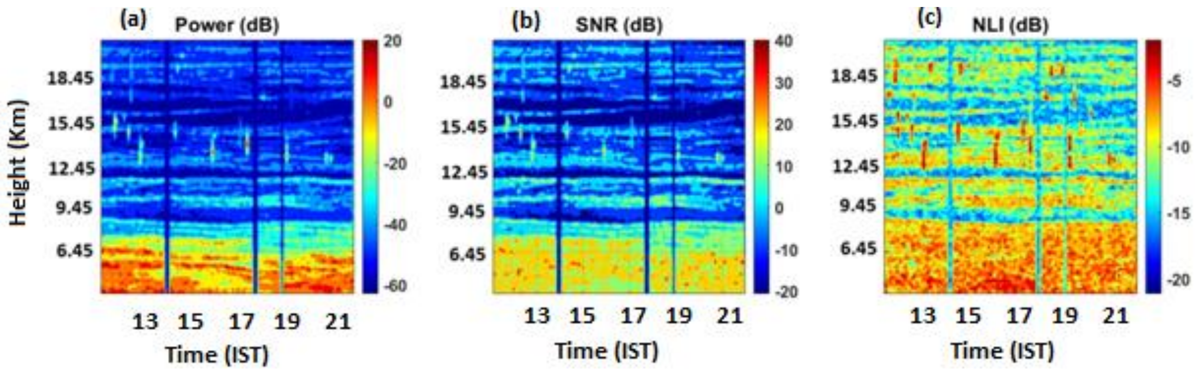

Fig. 6.3. The Height and time contour plots corresponding to a) Power, b) Nonlinear index (NLI), and c) SNR in log scale, of the vertical beam (Zenith beam) of the clear air system observed on 21 January 2023.

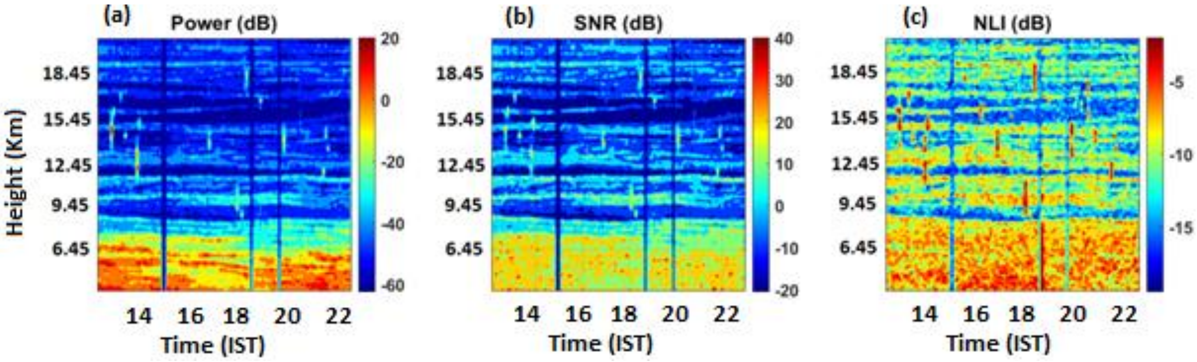

Fig. 6.4. The Height and time contour plots corresponding to a) Power, b) Nonlinear index (NLI), and c) SNR in log scale of the vertical beam (Zenith beam) of the clear air system observed on 21 January 2023.

Fig. 6.3a-c and 6.4a-c shows the Height and Time contour plot of NLI and SNR plotted in a log scale from 3.6 to 21 km. The NLI range is observed from -20 to 0 dB.Maximum values of NLI (-7 to 0 dB) are observed at the lowest altitude, up to 6 km, and the maximum values of -10 to -5 dB are found above 9 km. Strong SNRs have occurred in the lower regions of the atmosphere with maximum values of 20-40 dB. Stable layer structures have been found at 9-12 km with strong SNR that occurred with maximum values of 10-20 dB and above 11 km with 10-20 dB values. We can expect a maximum number of nonlinear interactions among eddies in this region; therefore, the nonlinearity index will be higher in this region. Therefore, clearly, we can observe a good similarity between the nonlinear index and SNR.

Fig.6.5a-f shows the vertical variation of temperature, Specific humidity,Pressure, wind speed, Lapse rate and Brunt Vaisala frequency, respectively. Fig. 6.5a shows the vertical profile of temperature, which shows the temperature gradients near the tropopause region above 15 km. The variation of the stability parameter is observed in the order of 0.01-0.04$s^{-2,}$ as shown in Fig. 6.5f. From Fig. 6.5d, the maximum wind speed is observed between the region of 10 to 15 km. The maximum values of specific humidity (~10g/kg) are observed below 5 km (Fig. 6.5b).

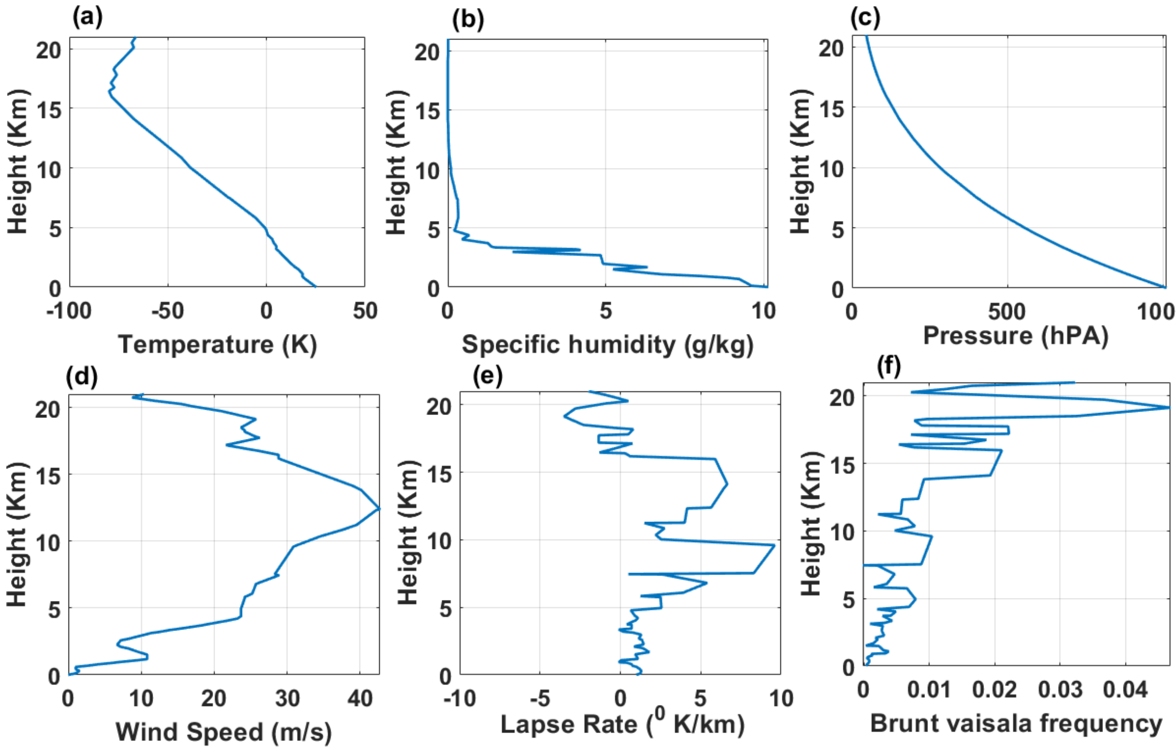

Fig. 6.5. Profiles of a) Temperature (K), b) Specific humidity (g/kg), c) Pressure (hPa), d) Wind speed (ms^{-1}),e) Lapse Rate (K/km) and f) Brunt Vaisala frequency obtained from the Radiosonde data on 21 January 2023 (05:30 IST).

6.6 Chapter Conclusion

Higher-order spectral analysis has been applied to the atmospheric radar backscattered signals to detect the nonlinearities associated with temperature sheets near the tropopause region. Clear air events data have been considered for the analysis from the above results. Enhancement of the radar signal in the vertical direction reveals the existence of the temperature sheets, which are clearly related to the occurrence and location of these gradients. The enhancement in the radar signal improves the SNR in the corresponding region. We can observe that the nonlinear index improvement in the same region shows the existence of temperature sheets due to the Fresnel reflection mechanism observed from the vertical profiles of the MST radar. From the above results, one can say that higher-order spectral analysis effectively identifies and characterizes the presence of temperature sheets present in the near tropopause region.However, this is one of the interesting subjects to study using Higher order spectral analysis. More data sets have to be considered to properly investigate these temperature sheets, and analysis should be carried out by using Higher-order statistics with corresponding location, date, and time of in situ measurements.

Chapter 7

Conclusions and Future Works

This chapter summarizes the overall observations and conclusions of the studies presented in the previous chapters of this thesis. Further, recommendations and future research directions in radar signal processing in turbulence studies are also presented in this chapter.

This thesis has investigated the statistical distribution of weather signals and the process associated with the weather and atmospheric signals and implemented efficient algorithms for estimatingradarparameters. This thesis proposed algorithms for noise and clutter removal in weather signals using Higher order spectral analysis and Empirical Mode Decomposition techniques alsodeveloped a new approach for the measurement of one of the important atmospheric parameters of turbulence eddy dissipation rate for atmospheric radars. Here we included the major conclusions of this thesis as chapter-wise below.

- In Chapter 3, the results from this chapter concluded that the bispectrum method is efficient when working under noisy conditions, as it significantly reduces the Gaussian noise components compared to conventional techniques like Pulse pair and Fourier methods.The remaining signal in the Doppler power spectrum is the non-Gaussian components that follow the non-Gaussian distribution characteristics. This helps in improving the signal-to-noise ratio (SNR), which in turn improves the detectability of the weather signal returns.
- In Chapter 4, we introduced a new approach for the measurement of turbulence eddy dissipation rates. Both convective and clear air system data have been considered for the analysis. The empirical relationship between NLI and ε established through regression models. The turbulent energy dissipation rate (ε) estimated from the Nonlinear index matches fairly well with ε measured from the spectral width method in both clear air and convective system with a good correlation of around 0.8. From the above results, it has been established that the nonlinear index shows the existence of turbulence in the backscattered signals, which means that it measures the turbulence intensity, and also observed that the estimation of the nonlinear index

efficiently identifies the multiple-layer structure around the tropopause region. From the above results, we can say that higher-order spectral analysis effectively identifies and characterises the nonlinearities occurring in the atmospheric signals, which can be used for estimating one of the important atmospheric parameters, turbulence energy dissipation rate.

- In Chapter 5, introduced a new approach, which is a modified version of EMD correlation based denoising method for removal of noise and clutter in weather signalsbased on the energy of the first and last IMFs.The analysis is carried out with a large number of data sets, and it found that the new approach successfully removes the ground clutter and denoise the weather signal in all cases. The moment estimation and its comparison with other techniques demonstrate the effectiveness of the signal processing approach in a complex observational environment.
- In Chapter 6, we developed an algorithm for analysing temperature sheets observed from the vertical profiles of VHF radar using Higher order spectral analysis.

Future Directions

- The turbulence studies discussed in previous chapters can extend to understanding the nonlinearities in weather signals caused by turbulence during severe weather conditions by using the indirect approach of the Nonlinear index for empirically calculating the turbulent energy.
- Study the turbulence associated with Squall lines and bow echoes from Mesoscale Convective Systems.
- Otherthan HOSA, Hilbert-Huang Transform technique also reveals the information about presence of nonlinearities in the data. Therefore, we can develop another method of HHT based algorithm for finding nonlinearities in weather signals.
- Development of Rain estimation algorithms and their impact due to statistical distribution of weather signals.

Acknowledgements for Data

I would like to acknowledge Dr. T. N.Rao from NARL for providing the data. The data used in this paper was collected from NARL, Gadanki. The authors also would like to thank NARL for providing data. The authors would also like to thank all their colleagues from the Radar Development Area of ISTRAC/ISRO.

References

Alappattu, D.P., Kunhikrishnan, P.K., 2010. First observations of turbulence parameters in the troposphere over the Bay of Bengal and the Arabian Sea using radiosonde. J. Geophys. Res. Atmos. 115, 1–12. https://doi.org/10.1029/2009JD012916.

Anandan,V.K., Ramachandra Reddy, G., Senior Member, IEEE, and P.B. Rao, 2001. Spectral Analysis of Atmospheric Radar Signal Using Higher Order Spectral Estimation Technique., IEEE Transactions on Geoscience and remote sensing, vol.39.

Atlas, D., 1964. Advances in radar meteorology. Adv. Geophys., 10, Eds., H.LandsbergandJ.vanMieghem, Academic, 317-478.

Atlas, D., Srivastava, R.C., and Sekhon, R.S., 1973. Dopler radar characteristics of precipitation at vertical incidence, Rev. Geophys. Space Phys., 1-35.

Ayenu-Prah, A., Attoh-Okine, N., 2010. A criterion for selecting relevant intrinsic mode functions in empirical mode decomposition. Adv. Adapt. Data Anal.2(1), 1.

Barnell, T., Johnson, L. C., Naitoh, P., Hicks, N., and Nute, C., 1971. Bispectrum analysis of electroencephalogram signal during waking and sleeping, Sciences, ,vol. 172, pp. 401–402.

Bartlet, H., Lohmann, A.W., and Wirnitzer, B., 1984. Phase and amplitude recovery from bispectra, Appl. Opt, Sept., vol. 23, pp. 3121–3129.

Batchelor, G. K., 1950. The application of the similarity theory of turbulence to atmospheric diffusion. Quart. J. r. meteor. Soc., 76, 133-146.

Birkelund, Yngve & Hanssen, Alfred, 2009. Improved bispectrum based tests for Gaussianity and linearity. Signal Processing., vol.89., 2537-2546, 10.1016/j.sigpro.2009.04.013.

Blackman, R.B., and Tukey, J.W., 1958. The measurement of power spectra from the point of view of communication engineering. Dover Publications, 190 pp.

Booker, H.G., and Gordon.,W.E., 1950. A theory of radio scattering in the troposphere. Proceedings of the IRE 38: 401–412.

Brillinger, D.R., Rosenblatt, M., 1967. Computation and interpretation of kth order spectra, B. Harris (Ed.), Spectral Analysis of Time Series, Wiley, New York, NY, 189–232.

Bringi V. N., and Chandrasekar, V., 2001. Polarimetric Doppler Weather Radar: Principles and Applications". Cambridge University Press, 636 pp.

Brewster, K.A. and Zrni'c, D. S., 1986. Comparison of Eddy Dissipation Rates from Spatial Spectra of Doppler Velocities and Doppler Spectrum Widths, J. Atmos. Oceanic Tech. 3, 440–452.

Browning, K. A. and R. Wexler, 1968. The determination of kinematic properties of a wind field using Doppler radar. J. Appl. Meteor., vol. 7,105- 113.

Byung Jun Yoon, P., Vaidyajnathan, P., 2004. Wavelet-based denoising by customized thresholding , ICASP.

Boudraa.A.O., Cexus, J. C., Saidi, Z., 2004. EMD-based signal noise reduction, Int. J. Signal Process. 1(1), 33–37.

Boudraa. A.O., Cexus, J. C., 2006. Denoising via empirical mode decomposition, in Proceedings of the IEEE International Symposium on Control, Communications and Signal Processing (ISCCSP' 06), Marrakech, Morocco,4.

Boudraa. A.O,, Cexus, J. C., 2007. EMD-Based Signal Filtering, IEEE Transactions on Instrumentation and Measurement, Vol. 56, NO. 6, 2196-2202.

Cherneva, Zhivelina & Andreeva, Nataliya & Petrova, Petya, 2004. Bi-spectral analysis of wind wave in the Black Sea coastal zone.

Choudhury, M. A. A. S., Shah, S. L., & Thornhill, N. F., 2003. Diagnosis of poor control loop performance using higher order statistics. Automatica, 40(10), 1719–1728.

Chu, Y. H., 2002. Beam broadening effect on oblique MST radar Doppler spectrum, J. Atmos. Oceanic Technol., 19, 1955–1967.

Clayson, C.A., Kantha, L., 2008. On turbulence and mixing in the free atmosphere inferred from high-resolution soundings. J. Atmos. Ocean. Technol. 25, 833–852. https://doi.org/10.1175/2007JTECHA992.1.

Clothiaux, E. E., Miller, M. A., Albrecht, B. A., Ackerman, T. P., Verlinde, J., Babb, D. M., Peters, R. M., and Syrett, W. J., 1995. An Evaluation of a 94-GHz Radar for Remote Sensing of Cloud Properties. J. Atmos. Oceanic Technol., 12, 201–229, https://doi.org/10.1175/1520-0426(1995)012<0201:AEOAGR>2.0.CO;2.

Coelli, Stefania & Tacchino, Giulia & Visani, Elisa & Panzica, Ferruccio & Silvana, Franceschetti & Bianchi, Anna. 2019. Higher Order Spectral Analysis of scalp EEG activity reveals non-linear behaviour during rhythmic visual stimulation. Journal of Neural Engineering, vol.16,10.1088/1741-2552/ab296e.

Cohn, S. A., 1995. Radar measurements of turbulent eddy dissipation rate in the troposphere: A comparison of techniques, J. Atmos. Oceanic Technol., 12, 85–95.

Coulman, C. E., Vernin, J., and Fuchs, A., 1995. Optical seeingmechanismof formation of thin turbulent laminae in the atmosphere, Appl. Opt., 34, 5461–5474.

Curtis, C., 2018. Weather radar time series simulation: Improving accuracy and performance. J.Atmos.OceanicTechnol.,35, 2169-2187, https://doi.org/10.1175/JTECH-D-17-0215.1.

Dalaudier, F., Sidi, C., Crochet, M., and Vernin, J., 1994. Direct evidence of “sheets” in the atmospheric temperature field, J. Atmos. Sci.,51, 237–248.

Das, S. S., Ghosh, A. K., Satheesan, K., Jain, A. R., and Uma, K. N., 2010. Characteristics of atmospheric turbulence in terms of background atmospheric parameters inferred using MST radar at Gadanki (13.5°N, 79.2°E), Radio Sci., 45, RS4008, doi:10.1029/2009RS004256.

Delage, D., Roca, R., Bertin, F., Delcourt, J., Cremieu, A., Massebeuf, M., and Ney, R., 1997. A consistency check of three radar methods for monitoring eddy diffusion and energy dissipation rates through the tropopause, Radio Sci., 32, 757–767.

Dias J. M. B., and J. M. N. Leitao, 2000. Nonparametric estimation of mean Doppler and spectral width, IEEE Transactions on Geoscience and Remote Sensing, vol. 38, no. 1, 271-282, doi: 10.1109/36.823919.

Domaradzki, J. A and ROGALLO, R. S., 1990. Local energy transfer and nonlocal interactions in homogeneous, isotropic turbulence. Phys. Fluids A 2, 413.

Donaldson, R.J., Jr., 1967. A preliminary report on Doppler radar observation ofturbulence in a thunderstorm. Air force Cambridge Research Laboratories, Environ. Res. Papers No. 255, 19.

Dong X, Hu, J., Hu, C., Chen, Z., and Li, Y., 2022. Rapid Identification and Spectral Moment Estimation of Non-Gaussian Weather Radar Signal, IEEE Transactions on Geoscience and Remote Sensing, vol. 60, 1-12, Art no. 5112912, doi: 10.1109/TGRS.2022.3168153.

Donoho D.L and Johnstone, I. M., 1994. Ideal spatial adaptation by wavelet shrinkage, Biometrika, vol. 81, no. 3, pp. 425 – 455.

Donoho D.L., 1995. De-noising by soft-thresholding, IEEE Trans Inform Theory, vol.14, No.3, 612-627.

Doviak, R. J. and Zrni'c, D. S., 1984. Doppler Radar and Weather Observations, Academic Press, Orlando, FL, 458.

Ecklude, W. L., Carter, D.A., and Balsley, B.B., 1979. Continuous measurement of upper atmospheric winds and turbulence using VHF radar: Preliminary results. J. Atmos.Terr.Phys. 41,983-984

Flandrin. P, G. Rilling, and P. Gonc¸alv'es, 2004. Empirical mode decomposition as a filterbank, IEEE Signal Processing Lett, vol. 11, 112–114.

Flandrin, P., Rilling, G., Goncalces, P., 2005. EMD equivalent filter banks, from interpretations to application, Hilbert-Huang Transform and its Application, N. E. Huang and S. Shen, Eds., 1st ed. Singapore: World Scientific,.

Frisch, A. S. and Clifford, S. F., 1974. A Study of Convection Capped by a Stable Layer Using Doppler Radar and Acoustic Echo Sounders, J. Atmos. Sci. 31, 1622–1628.

Fritts, D.C., Wang, L., Geller, M.A., Lawrence, D.A., Werne, J., Balsley, B.B., 2016. Numerical modeling of multiscale dynamics at a high Reynolds number: instabilities, turbulence, and an assessment of Ozmidov and Thorpe cales. J. Atmos. Sci. 73, 555–578. https://doi.org/10.1175/JAS-D-14-0343.1.

Fukao, Shoichiro & Hamazu, Kyosuke., 2014. Radar for Meteorological and Atmospheric Observations. Springer, 10.1007/978-4-431-54334-3.

Furumoto, J., and Tsuda, T., 2001. Characteristics of energy dissipation rate and effect of humidity on turbulence echo power revealed by MU radar–RASS Measurements, J. Atmos. Sol. Terr. Phys., 63, 285–294.

Gage, K. S., Green, J. L., and Vanzandt, T. E., 1980. Use of Doppler radar for the measurement of atmospheric turbulence parameters from the intensity of clear air echoes, Radio Sci., 15, 407–416.

Ghosh, A. K., Jain, A.R., and Sivakumar,V., 2000. Characteristics of atmospheric wind, associated shear and turbulence: Indian MST radar measurement during summer monsoon season, Indian J. Radio Space Phys., 29, 222–230.

Ghosh A.K, Jain, A.R., and Sivakumar, V., 2003. Simultaneous MST radar and radiosonde measurements at Gadanki (13.5°N, 79.2°E) 2. Determination of various atmospheric turbulence parameters, Radio Science, vol. 38, no. 1, pp. 14-1-14-12, doi: 10.1029/2000RS002528.

Giannakis G. B.,and M. K. Tsatsanis, 1990. Signal detection and classification using matched filtering and higher order statistics, IEEE Trans. Acoust., Speech, Signal Processing, vol. 38, 284–296.

Gossard, E. E. and Strauch, R. G., 1983. Radar Observations of Clear Air and Clouds, Elsevier, Amsterdam, New York, 280.

Gossard, E. E., Wolfe, D. E., Moran, K. P., Paulus, R. A., Anderson, K. D., and Rogers, L. T., 1998. Measurement of Clear-Air Gradients and Turbulence Properties with Radar Wind Profilers, J. Atmos. Oceanic Tech. 15, 321–342.

Groginsky, H.L. and Glover, K.M., 1980. Weather radar canceller design. In Preprints, 19th Radar Meteorology Conference, Boston, MA, American Meteorological Society. 192–198.

Hadjileontiadis. L. J., 2007. Empirical mode decomposition and fractal dimension filter, IEEE Eng. Med. Biol. Mag., 30–39.

Hara, Tetsu & Karachintsev, Andrey, 2003. Observation of Nonlinear Effects in Ocean Surface Wave Frequency Spectra. Journal of Physical Oceanography., vol. 33,422-430.

Hasslemann, K., W. Munk, and G. MacDonald, 1963. Bispectrum of ocean waves, Time Series Analysis, M. Rossenblatt, Ed. New York: Wiley,125–139.

He, Y., Zhu, X., Sheng, Z., He, M. and Feng, Y., 2022. Observations of Inertia Gravity Waves in the Western Pacific and Their Characteristic in the 2015/2016 Quasi-Biennial Oscillation Disruption. Journal of Geophysical Research: Atmospheres 127, e2022JD037208, https://doi.org/10.1029/2022JD037208 .

Helland K,. N., Lii, K. S., and Rosenblatt, M.T., 1978. Bispectra of atmospheric and wind tunnel turbulence. Applications of Statistics (ed. P. It. Krishniah), 223-248. North Holland.

Herring, J., 1980. Theoretical calculations of turbulent bispectra, Journal of Fluid Mechanics, 97(1), 193-204. doi:10.1017/S0022112080002509.

Hildebrand P. H., and Sekhon, R. S., 1974. Objective determination of the noise level in Doppler spectra, J. Appl. Meterol., , vol. 13, 808–811.

Hinich, M. J., 1982. Testing for Gaussianity and linearity of a stationary time series. Journal of Time Series Analysis, 3, 169–176.

Hocking, W. K., 1983. On the extraction of atmospheric turbulence parameters from radar backscatter Doppler spectra, I: Theory, J. Atmos. Terr. Phys., 45, 89–102.

Hocking, W. K., 1985. Measurements of turbulent energy dissipation rates in the middle atmosphere by radar techniques: A review, Radio Sci., 20, 1403–1422.

Hocking. W.K., 1986. Observation and measurement of turbulence in the middleatmosphere with a vhf radar. Journal of Atmospheric and Terrestrial Physics, 48(7), 655-670.

Hocking, W. K., Fukao, S., Yamamoto, M., Tsuda, T., and Kato,S., 1991. Viscosity waves and thermal-conduction waves as a cause of “specular” reflectors in radar studies of the atmosphere, RadioSci., 26, 1281–1303.

Huang.N. E, Z. Shen, S. R. Long, M. C. Wu, H. H. Shin, Q. Zheng, N.C. Yen, C. C. Tung and H. H. Liu, 1998. The Empirical Mode Decomposition and the Hilbert spectrum for nonlinear and non-stationary time series analysis, Proceedings of the Royal Society of London, 454, 903–995.

Huang. HC, and N. Cressie, 2000. Deterministic/stochastic wavelet decomposition for recovery of signal from noisy data, Technometrics, vol. 42, 262–276.

Huang. NE and Z. Wu, 2005. Statistical significance test of intrinsic mode functions, in Hilbert-Huang Transform and Its Applications, N. E. Huang and S. Shen, Eds., 1st ed. Singapore: World Scientific,.

Hubbert, J.C.; Dixon, M.; Ellis, S.M.; Meymaris, G., 2009. Weather Radar Ground Clutter. Part I: Identification, Modeling, and Simulation. J. Atmos. Ocean. Technol., 26, 1165–1180.

Hubbert, J.C.; Dixon, M.; Ellis, S.M.; Meymaris, G. 2009. Weather Radar Ground Clutter. Part II: Real-Time Identification and Filtering. J. Atmos. Ocean.Technol., 26, 1181–1197.

Ice, R. L., Rhoton, R.D.; Krause, J.C., Saxion, D. S., Boydstun, O.E., Heck, A.K., Chrisman, J.N., Berkowitz, D.S., 2009. Automatic clutter mitigation in the WSR-88D, design, evaluation, and implementation. In Proceedings of the 34th Conference on Radar Meteorology, Williamsburg, 5, VA, USA, 5–9.

Imran, Akhtar & Elyyan, Mohammad, 2018. Higher-Order Spectral Analysis to Identify Quadratic Nonlinearities in Fluid-Structure Interaction. Mathematical Problems in Engineering., 1-14. 10.1155/2018/2394124.

Ivic, I. R., and Torres, S. M., 2010. Online determination of noise level in weather radars. Proc. Sixth European Conf. on Radar in Meteorology and Hydrology (ERAD 2010), 7. http://www.Erad 2010.org/pdf/oral/monday/6_ERAD2010_0094.pdf.

Ivic, I.R., Curtis, C. & Torres, S.M, 2013. Radial based noise power estimation for weather radars, Journal of Atmospheric and Oceanic Technology, , 30(12),2737-2753.

Jacoby-Koaly, S., Campistron, B., Bernard, S., B'enech, B., Ardhuin-Girard, F., Dessens, J., Dupont, E., and Carissimo, B., 2002. Turbulent dissipation rate in the boundary layer via UHF wind profiler Doppler spectral width measurements. Boundary-Layer Meteor., 103, 361–389.

Janssen, L. H., and Van Der Spek, G. A., The shape of Doppler spectra from precipitation. IEEE Trans. Aerosp. Electron. Syst, 1985, AES-21, 208–219, https://doi.org/10.1109/TAES.1985.310618.

Jayarao, Y., Jain, A.R., Anandan.V.K., Rao P.B., Viswanathan, G and Aravindan, R., 1994. Some observations of tropical tropopause using ST mode of the Indian MST radar: Multiple stable layer structure, Indian J Radio and Space Phy, 23, 75-85.

Jing-Tian. T, Z. Qing, T. Yan, L. Bin, and Z. Xiao-Kai, 2007. Hilbert-huang transform for ECG denoising, in Proc. 1st Int. Conf. Bioinf. Biomed.Eng (ICBBE 2007).

John J. Hicks, Isadore Katz, Claude R. Landry, and Kenneth R. Hardy, 1967. Clear-Air Turbulence: Simultaneous Observations by Radar and Aircraft, Science, Science :vol. 157. no. 3790, 808–809

Jouny, I.I., Moses, R.L., 1992. The bispectrum of complex signals: definitions and properties, IEEE Trans. Signal Process, vol. 40,2833–2836.

Kantha, L., Hocking, W., 2011. Dissipation rates of turbulence kinetic energy in the free atmosphere: MST radar and radiosondes. Journal of Atmospheric and Solar-Terrestrial Physics, 73(9), 1043–1051.

Keeler, R. J., Passarelli, R.E. 1990. Signal Processing for Atmospheric Radars. In: Atlas, D. (eds) Radar in Meteorology. American Meteorological Society, Boston, MA. https://doi.org/10.1007/978-1-935704-15-7_21

Kim, Y. C., and Powers, E. J., 1979. Digital bispectral analysis and its applications to non - linear wave interactions, IEEE Trans. Plasma Sci, vol. PS-7, 120–131.

Ko, H.C., Chun, H.Y., Wilson, R., Geller, M.A., 2019. Characteristics of atmospheric turbulence retrieved from high vertical-resolution radiosonde data in the United States. J. Geophys. Res. Atmos. 124, 7553–7579. https://doi.org/10.1029/ 2019JD030287.

Kohma, M., Sato, K., Tomikawa, Y., Nishimura, K., Sato, T., 2019. Estimate of turbulent energy dissipation rate from the VHF radar and radiosonde observations in the Antarctic. J. Geophys. Res. Atmos. 124, 2976–2993. https://doi.org/10.1029/ 2018JD029521.

Komaty, A., Boudraa, A.O., Dare, D., 2012. EMD-based filtering using the Hausdoff distance. Proceedings of IEEE International Symposium on Signal Processing and Information Technology (ISSPIT 2012).

Komaty, A., Boudraa, A.O., Augier, B., Dare-Emzivat, D., 2014. EMD based filtering using similarity measure between probability density functions of IMFs. IEEE Trans. Instrum. Meas., 63 (1), 27–34.

Kopsinis,Y., Mclanglin, S., 2009. Development of EMD-based denoising methods inspired by wavelet thresholding, IEEE Trans. Signal Process,. 57 (4) 1351–1362.

Kopsinis. Y., McLaughlin, S., 2008. Empirical Mode Decomposition Based Soft-Thresholding, in Proc. 16th Eur. Signal Process. Conf. (EUSIPCO), Lausanne, Switzerland, 25–29.

Kopsinis. Y and McLauglin, S., 2008. Investigation and performance enhancement of the empirical mode decomposition method based on a heuristic search optimization approach, IEEE Trans. Signal Process, 1–13.

Kopsinis. Y and McLauglin, S., 2008. Empirical mode decomposition based denoising techniques, in Proc. 1st IAPR Workshop Cogn. Inf. Process. (CIP), Santorini, Greece, Jun. 9–10, 42–47.

Kotriwar, Yamini & Kachhara, Sneha & Harikrishnan, K. & Ambika, G, 2018. Higher order spectral analysis of ECG signals.

Kumar, S., Rao, T.N., Rao, M.D., and Patra, A.K., 2021. Experimental Evaluation of Theoretical Formulations for the Correction of Spectral Widths of MST Radar Spectra, in IEEE Transactions on Geoscience and Remote Sensing, vol. 59, no. 8, pp. 6397-6403, Aug. 2021, DOI: 10.1109/TGRS.2020.3026059.

Lagha, Mohand & Bensebti, Messaoud, 2006. Doppler Spectrum Estimation by Ramanujan Fourier Transforms.

Lagha, Mohand & Tikhemirine, M., & Bergheul, S., & Rezoug, Tahar & Bettayeb, Maamar, 2013. De-noised estimation of the weather Doppler spectrum by the wavelet method. Digital Signal Processing, vol.23. 322-328, 10.1016/j.dsp.2012.08.001.

Lane, T.P., Sharman, R.D., Clark, T.L., and Hsu, H.M., 2003. An investigation of turbulence generation mechanisms above deep convection. J. Atmos. Sci, 60, 1297–1321.

Lhermitte, R.M., Atlas, D.,1961. Precipitation motion by pulse Doppler radar. Proc. Weather Radar Conf., 9th, 218-223.

Lee, Jonggil., 2010. Doppler moment estimation in a weather radar. International Journal of Electronics. 583-592. 10.1080/002072102100004433I.

Li, Q., Rapp, M., Schr¨on, A., Schneider, A., Stober, G., 2016. Derivation of turbulent energy dissipation rate with the middle atmosphere Alomar radar system (MAARSY) and radiosondes at Andøya, Norway. Ann.Geophys. 34, 1209–1229. https://doi. org/10.5194/angeo-34-1209-2016.

Li, Y., Zhang, G., Doviak, R.J., Lei, L., Cao, Q., 2013. A New Approach to Detect Ground Clutter Mixed with Weather Signals. IEEE Trans. Geosci. Remote Sens, 51, 2373–2387.

Li, Y., Zhang, G., Doviak, R.J., Saxion, D.S., 2013. Scan-to-Scan Correlation of Weather Radar Signals to Identify Ground Clutter. IEEE Geosci. Remote Sens. Lett., 10, 855–859.

Lii, K.S., Rosenblatt, M., Van Atta, C., 1976. Bispectral measurements in turbulence. J. Fluid Mech. 77(1), 45–62.

Luce, H., Crochet, M., Dalaudier, F., and Sidi, C., 1995. Interpretationof VHF ST radar vertical echoes from in-situ temperature sheetobservations, Radio Sci., 30, 1002–1025.

Luce, H., Crochet and Dalaudier, F., 2001.Temperature sheets and aspect sensitive radar echoes, Annales Geophysicae, 19, 899-920.

MacCready, P. B., Jr., 1953. Structure of Atmospheric Turbulence, Journal of Atmospheric Sciences, 10(6), 434-449. Retrieved 15 July, 2021, from https://journals.ametsoc.org/view/journals/atsc/10/6/15200469_1953_010_0434_soat_2_0_co_2.xml

Mahapatra, Pravas R., 1999. Aviation Weather Surveillance Systems: Advanced Radar and Surface Sensors for Flight Safety and Air Traffic Management, Institution of Electrical Engineers and American Institute of Aeronautics and Astronautics, 453.

Mao. Y and Que, P., 2007. Noise suppression and flaw detection of ultrasonic signals via empirical mode decomposition, Rus. J. NondestructTest, vol. 43, 196– 203.

Middleton, D., 1960. An Introduction to Statistical Communication Theory. New York, McGraw-Hill.

Moffatt, H., 2014. Note on the triad interactions of homogeneous turbulence. Journal of Fluid Mechanics, 741, R3. doi:10.1017/jfm.2013.637.

Molla. M. K. I and K. Hirose, 2007. Single-mixture audio source separation by subspace decomposition of Hilbert spectrum, IEEE Trans. Audio, Speech Lang.Process., 893–900.

Muhsin, M., Sunilkumar, S.V., Ratnam, M.V., Parameswaran, K., Murthy, B.V.K., Ramkumar, G., Rajeev, K., 2016. Diurnal variation of atmospheric stability and turbulence during different seasons in the troposphere and lower stratosphere derived from simultaneous radiosonde observations at two tropical stations, in the Indian Peninsula. Atmos. Res. 180, 12–23. https://doi.org/10.1016/j. atmosres.2016.04.021.

Narayana Rao, D., Kishore, P., Narayana Rao, T., Vijaya Bhaskara Rao, S., Krishna Reddy, K., Yarraiah, M., and Hareesh, M., 1997. Studies on refractivity structure constant, eddy dissipation rate and momentum flux at a tropical latitude, Radio Sci., 32, 1375–1389.

Nasrolahzadeh, Mahda&Mohammadpoory, Zeynab&Haddadnia, Javad, 2018. Higher-order spectral analysis of spontaneous speech signals in Alzheimer’s disease. Cognitive Neurodynamics, vol.12, 10.1007/s11571-018-9499-8.

Nastrom, G. D. and Eaton, F. D., 1997, Turbulence Eddy Dissipation Rates from Radar Observations at 5–20 km at White Sands Missile Range, New Mexico, J. Geophys. Res. 102, 19,495–19, 505.

Nastrom, G. D., 1997, Doppler radar spectral width broadening dueto beamwidth and wind shear, Ann. Geophy., 15, 786–796.

Nath, D., VenkatRatnam, M., Rao, V., Murthy, B., Vijaya, S and Rao, S., 2009. Gravity wave characteristics observed over a tropical station using high-resolution GPS radiosonde soundings. Journal of Geophysical Research Atmospheres. 114. 10.1029/2008JD011056.

Nath, D., Venkat Ratnam, M., Patra, A.K., Krishna Murthy, B.V., Bhaskar Rao, S.V., 2010. Turbulence characteristics over tropical station Gadanki (13.5N, 79.2E) estimated using high-resolution GPS radiosonde data. J. Geophys. Res. Atmos. 115 https://doi. org/10.1029/2009JD012347.

Naumenko, Victoria & Totsky, Alexander & Khlopov, Grygoriy & Voitovych, O. & Astola, J., 2016. Classification of the atmospheric formations by using bicoherence-based features extracted from weather radar backscattering signals. Telecommunications and Radio Engineering., vol. 75, pp. 463-475, 10.1615/TelecomRadEng.v75.i5.70.

Nikias, C.L., and Mendel, J. M., 1993. Signal processing with higher-order spectra, IEEE Signal Processing Mag, 10–38.

Nikias, C. L., and. Petropulu, A. P., 1993. Higher-Order Spectral Analysis: A Nonlinear Signal Processing Framework, Prentice-Hall, Inc.

Nikias C. L., and Raghuveer, M. R., 1987. Bispectral estimation: A digital signal processing framework, Proc. IEEE, vol. 75, 869–891.

Ning. B, Qiyu, S., Zhihua, Y., Daren, H., and Jiwu, H., 2007. Robust image watermarking based on multiband wavelets and empirical mode decomposition, IEEE Trans.Image Process., 1956–1966.

Orszag, S. A., 1970. Analytical theories of turbulence. J. Fluid Mech. 41 (part 2), 363–386.

Ottersten H., 1969. Atmospheric structure and radar backscattering in clear air, in Radio Science, vol. 4, no. 12, 1179-1193, doi: 10.1029/RS004i012p01179.

Panchev, S., 1971. Random functions and Turbulence, Pergamon press.

Papoulis, A. 1965. Probability, Random Variables and Stochastic Processes. New York, McGraw-Hill.

Peng, Z.K., Peter, W.T., Chu, F.L., 2005. Comparison study of improved Hilbert-Huang transform and wavelet transform: Application to fault diagnosis for rolling bearing. Mech. Syst. Signal Process. 19(5), 974.

Peter J. S, and Scharf, L.L., 2006. Higher-order spectral analysis of complex signals, Signal Processing, Volume 86, Issue 11, Pages 3321-3333, ISSN 0165-1684, https://doi.org/10.1016/j.sigpro.2006.02.027

Peter Zsolt, Poloskei & Papp, Gergely & Por, Gabor & Horvath, Laszlo & Pokol, Gergo, 2018. Bicoherence analysis of nonstationary and nonlinear processes.

Pires, Carlos & Hannachi, Abdel., 2021. Bispectral analysis of nonlinear interaction, predictability and stochastic modelling with application to ENSO. Tellus A: Dynamic Meteorology and Oceanography, vol. 73, 1-30, 10.1080/16000870.2020.1866393.

Pope, S., 2000. Turbulent Flows. Cambridge., Cambridge University Press. Doi: 10.1017/CBO9780511840531.

Pradhan, Cauchy & Jena, Susant & Nadar, Sreenivasan & Pradhan, N., 2012. Higher-Order Spectrum in Understanding Nonlinearity in EEG Rhythms. Computational and mathematical methods in medicine, 206857.10.1155/2012/206857.

Praskovsky, A. A., Gledzer, E. B., Karyakin, M. Y. & Zhou, Y. 1993. The sweeping decorrelation hypothesis and energy-inertial scale interaction in high Reynolds number Flows. J. Fluid Mech. 248, 493–511.

Probert-Jones, J.R. 1962. The radar equation in meteorology. Quarterly Journal of the
Royal Meteorological Society 88: 485–495.

Qu, CS, T. Z. Lu, Tan, Y. 2010. A modified empirical mode decomposition method in Applications to signal de-noising [J], Acta Autom.Sin.36 (1), 67–73.

Ramyakrishna Enugonda, Anandan, V. K., & Basudeb Ghosh, 2022. Higher order spectral analysis of weather signals, Journal of Electromagnetic Waves and Applications, 10.1080/09205071.2022.2112762.

Rao, T. S., and Gabr, M. M., 1980. A Test For Linearity Of Stationary Time Series, Journal of Time Series Analysis, Wiley Blackwell, vol. 1(2), 145-158.

Rao P.B., Jain, A.R., Kishore, P., Balamuralidhar, P., Damle, S.H., and Viswanathan, G., 1995. Indian MST radar 1. System description and samplevector wind measurements in ST mode, Radio Sci., vol. 30, 1125–1138.

Rao T.N, Rao, D.N., and Raghavan, S., 1999. Tropical precipitating systems observed with Indian MST radar, Radio Science, vol. 34, no. 5, pp. 1125-1139, doi: 10.1029/1999RS900054.

Rao, md & Kamaraj, Pandian & Kumar, J. & Jayaraj, K. & Prasad, K.M.V. & Raghavendra, J. & Rao Fna Fasc, T. & Patra, A.K., 2020. The Advanced Indian MST Radar (AIR): System Description and Sample Observations. Radio Science. 55. 10.1029/2019RS006883.

Richard J. Doviak, Dušan Zrnić, S., 1984. Doppler Radar and Weather Observations (Second Edition), Academic Press, ISBN9780323149167, 119.

Rilling. G and P. Flandrin, 2008. One or two frequencies? The empirical mode decomposition answers, IEEE Trans. Signal Process, 85–95.

Rogers, R.R., 1979. A Short Course in Cloud Physics. Pergamon Press, 235pp.

Rosenblatt, M., and Van Ness, J.W., 1965. Estimation of the Bispectrum, Ann.Math.Statist., vol. 36, 1120-1136.

Röttger, J.,1980. Reflection and scattering of VHF radar signals from atmospheric refractivity structures, Radio Sci., vol. 15, 259–276.

Ryle Martin, 1952. A new radio interferometer and its application to the observation of weak radio stars, Proc.R.Soc.Lond. A211351–375, http://doi.org/10.1098/rspa.1952.0047

Sachidananda, M., and Zrnić D., 2000. Clutter filtering and spectral moment estimation for Doppler weather radars using staggered pulse repetition time (PRT). J. Atmos. Oceanic Technol, 17, 323–331.

Sadler, B.M., Giannakis, G.B., and Lii, K.S., 1994. Estimation and detection in non-Gaussian noise using higher order statistics. IEEE Trans.Signal Processing,vol. 42, 2729–2741.

Sasi, M. N., and Sen Gupta, K.,1986, A reference atmospherefor Indian equatorial zone from surface to 80 km-1985, Sci. Rep. SPL:SR:006:85, Space Phys. Lab., Vikram Sarabhai Space Cent., Trivandrum, India.

Satheesan, K., and Krishnamurthy, B.V., 2002. Turbulence parameters in the tropical troposphere and lower stratosphere, Journal of Geophysical Research Vol, 107, No DI, 4002, 10.029/2000JD000146.

Sato, T., Tsuda, T., Kato, S., Morimoto, S., Fukao, S., and Kimura, I., 1985. High-resolution MST observations of turbulence using the MU radar, Radio Sci., 20, 1452–1460.

Sato, K., Hashiguchi, H., and Fukao, S.,1995. Gravity waves and turbulence associated with cumulus convection observed with the UHF/VHF clear-air Doppler radars. Journal of Geophysical Research, 100(D4), 7111–7119. https://doi.org/10.1029/95JD00198

Sekine, M., Musha, T., Tomita, Y., Hagisawa, T., Irabu, T., and Kiuchi, E., 1979. On Weibull-Distributed Weather Clutter, IEEE Transactions on Aerospace and Electronic Systems, Nov., vol. AES-15, no. 6, pp. 824-830, doi: 10.1109/TAES.1979.308767.

Sharman, R.D., Trier, S.B., Lane, T.P., and Doyle, J.D., 2012. Sources and dynamics of turbulence in the upper troposphere and lower stratosphere: A review. Geophysical Research Letters. 39. 12803-. 10.1029/2012GL051996.

Siggia, A. D., and Passarelli, R. E., 2004. Gaussian model adaptive processing (GMAP) for improved ground clutter cancellation and moment calculation. Third European Conference on Radar in Meteorology and Hydrology (ERAD) together with the COST 717 Final Seminar, Copernicus GmbH, 67–73.

Sirmans, D., and Bumgarner, B., 1975: Numerical Comparison of Five Mean Frequency Estimators. J. Appl. Meteor. Climatol., 14, 991–1003, https://doi.org/10.1175/1520-0450(1975)014<0991:NCOFMF>2.0.CO;2.

Sloss, P.W., and Atlas, D., 1968. Wind shear and reflectivity gradient effects on Doppler radar spectra, J. Atmos. Sci., 25, 1080-1089,1968.

Smyth, W. D. and Moum, J. N., 2000. Length scales of turbulence in stably stratified mixing layers, Phys. Fluids, 12, 1327–1342.

Smyth, W., Moum, J. & Caldwell, D. 2001 The efficiency of mixing in turbulent patches: inferencesfrom direct simulations and microstructure observations. J. Phys. Oceanogr. 31, 1969–1992.

Strauch, R.G., Merritte, D.A., Moran, K.P., Earnshaw, K.B., and van de Kamp, J. D., 1984. The Colorado wind profiling network. J. Atmos. Oceanic Tech.1, 37-49.

Sunilkumar, S. V., Muhsin, M., Parameswaran, K., Venkat Ratnam, M., Ramkumar, G., Rajeev, K., Krishna Murthy, B. V., Sambhu Namboodiri, K. V., Subrahmanyam, K. V., Kishore Kumar, K., Shankar Das, S., 2015. Characteristics of turbulence in the troposphere and lower stratosphere over the Indian Peninsula. Journal of Atmospheric and Solar-Terrestrial Physics. 133. 10.1016/j.jastp.2015.07.015.

Tang, Y.W., Tai, C.C., Su, C.C., 2010. A correlated empirical mode decomposition method for partial discharge signal denoising. Meas. Sci. Technol. 21(8), 085.

Tatarskii, V.I., 1961.Wave Propagation in a Turbulent Medium. McGraw Hill, 285 pp.

Tatarskii, V. I., 1971. The effects of the turbulent atmosphere on wave propagation, U.S., Department of Commerce, Washington, DC, 74–76.

Thorpe, S. A., Deacon, G. E. R., 1977. Turbulence and mixing in a Scottish Loch., Philos. Trans. R. Soc. London. Ser. A, Math. Phys. Sci. 286, 125–181. https://doi.org/10.1098/rsta.1977.0112.

Totsky, Alexander & Egiazarian, Karen., 2018. Bispectrum and Bicoherence-Based Discriminative Features Used for Classification of Radar Targets and Atmospheric Formations, , 10.5772/intechopen.71034.

Trier, S.B., Sharman, R.D., Muñoz-Esparza, D., and Lane, T.P., 2020. Environment and Mechanisms of Severe Turbulence in a Midlatitude Cyclone. Journal of the Atmospheric Sciences. 77. 1-63. 10.1175/JAS-D-20-0095.1.

Tsolis. G.S., and Xenos, T.D., 2011. Signal Denoising Using Empirical Mode Decomposition and Higher Order Statistics, International Journal of Signal Processing, Image Processing and Pattern Recognition, vol. 4, No. 2, 91-106.

Urkowitz, H., and J. D. Nespor, 1992. Obtaining spectral moments by discrete Fourier transform with noise removal in radar meteorology, IGARSS '92: International Geoscience and Remote Sensing Symposium; International Space Year, IEEE, 12–14.

Van Atta, C.W., 1976. Bispectral measurements in turbulence, J. Fluid Mech., vol. 77, 45–62.

Vanatta, C. W., 1979. Inertial range bispectra in turbulence. Phys. Fluids. 22, 1440-1442.

Wacławczyk, M., Ma, Y.F., Kopeć, J. M., and Malinowski, S. P., 2017. Novel approaches to estimating the turbulent kinetic energy dissipation rate from low and moderate resolution velocity fluctuation time series, Atmos. Meas. Tech., 10, 4573–4585, https://doi.org/10.5194/amt-10-4573-2017.

Waleffe, F., 1992. The nature of triad interactions in homogeneous turbulence. Phys. Fluids A 4, 350.

Warde. D.A and Torres, S. M., 2014. The Autocorrelation Spectral Density for Doppler-Weather-Radar Signal Analysis, IEEE Transactions on Geoscience and Remote Sensing, Jan., vol. 52, no. 1, 508-518, doi: 10.1109/TGRS.2013.2241775.

Williams, Christopher & Maahn, Maximilian & Hardin, Joseph & Boer, Gijs., 2018. Clutter mitigation, multiple peaks, and high-order spectral moments in 35 GHz vertically pointing radar velocity spectra. Atmospheric Measurement Techniques. 11. 4963-4980. 10.5194/amt-11-4963-2018.

Wilson, R., Luce, H., Dalaudier, F., Lefr`ere, J., 2010. Turbulence patch identification in potential density or temperature profiles. J. Atmos. Ocean. Technol. 27, 977–993. https://doi.org/10.1175/2010JTECHA1357.1.

Wilson R., Dalaudier, F., Luce, H., 2011. Can one detect small-scale turbulence from standard meteorological radiosondes?, Atmos.Meas.Tech., 4, 795–804. http: //dx.doi.org/10.5194/amt-4-795-2011.

Wilson, R., Luce, H., Hashiguchi, H., Nishi, N., and Yabuki, Y., 2014. Energetics of persistent turbulent layers underneath mid-level clouds estimated from concurrent radar and radiosonde data. Journal of Atmospheric and Solar-Terrestrial Physics, 118, 78–89. https://doi.org/10.1016/j.jastp.2014.01.005

Woodman, R.F., and Hagfors, T., 1969. Methods for the measurement of vertical ionospheric motions near the magnetic equator by incoherent scattering, J.Geophys.Res., 74,1205- 1212.

Woodman, R.F., 1985. Spectral moments estimation in MST radars, Radio Science, vol. 20, no. 6, 1185–1195.

Woodman, R.F., and A Guillen, 1985. Radar observations of winds andturbulence in the stratosphere and mesosphere, J. Atmos. Sci., 31,493-505.

Worthington R.M., Palmer, R.D., and Fukao, S., 1999. An investigation of tilted aspect-sensitive scatterers in the lower atmosphere using the MU and Aberystwyth VHF radars, Radio Sci., vol. 34, 413–426.

Wu. Z and Huang, N. E., 2004. A study of the characteristics of white noise using the empirical mode decomposition method, Proc. Roy. Soc. London A, vol. 460, 1597–1611.

Yamada, T., Itoh, S.I., Inagaki, S., Nagashima, Y., Shinohara, S., Kasuya, N., Terasaka, K., Kamataki, K., Arakawa, H., Yagi, M., 2010. Two-dimensional bispectral analysis of drift wave turbulence in cylindrical plasma. Phys. Plasmas 17(5), 052313.

Yang. G, Liu, Y., Wang, Y., Zhu, Z., 2015. EMD interval thresholding denoising based on similarity measure to select relevant modes, Signal Processing, 109, 95–109.

Yeh, T. T., and Vanatta, C. W., 1973. Spectral transfer of scalar and velocity fields in heated-grid turbulence. J. Fluid Mech. 58, 233-261.

Yeung, P., Brasseur, J. G. and Wang, Q., 1995. Dynamics of direct large-small scale couplings in coherently forced turbulence: concurrent physical-and Fourier-space views. J. Fluid Mech. 283, 43–96.

Yinguang, L.; Guifu, Z.; Doviak, R.J., 2011. A new approach to detect the ground clutter mixed with weather echoes. In IEEE Radar Conference (RADAR), Kansas City, MO, USA.

Yoshikawa, Eiichi & Takizawa, Naoya& Kikuchi, Hiroshi &Mega, Tomoaki & Ushio, T., 2021. An Estimator for Weather Radar Doppler Power Spectrum via Minimum Mean Square Error. IEEE Transactions on Geoscience and Remote Sensing., PP. 1-16. 10.1109/TGRS.2020.3044111.

Yu T. Y, R. R. Rondinel, and R. D. Palmer, 2009. Investigation of non-Gaussian Doppler spectra observed by weather radar in a tornadic supercell, J. Atmos. Ocean. Technol., vol. 26, no. 3, 444–461.

Zhang, Y., Gao, Y., Wang, L., Chen, J., and Shi, X., 2007. The removal of wall components in Doppler ultrasound signals by using the empirical mode decomposition algorithm, IEEE Trans. Biomed. Eng, vol. 9, 1631–1642.

Zhang, G., Doviak, R. J., 2014. Ground Clutter Detection Using the Statistical Properties of Signals Received with a Polarimetric Radar. IEEE Trans. Signal Process., 62, 597–606.

Zhang M, Wei G, 2020. An integrated EMD adaptive threshold denoising method for reduction of noise in ECG, Plos One, 15(7).

Zrnic D. S, 1975. Simulation of weather like Doppler spectra and signals, J. Appl. Meteorol., vol. 14, no. 4, 619 pp.

Zhou, Y., 1993a. Degrees of locality of energy transfer in the inertial range. Phys. Fluids A 5 (5), 1092–1094.

Zhou, Y., 1993b. Interacting scales and energy transfer in isotropic turbulence. Phys. Fluids A 5 (10), 2511–2524.

List of Publications and Conferences

- Ramyakrishna Enugonda, V. K. Anandan & Basudeb Ghosh "Application of Empirical Mode Decomposition for Denoising and Ground Clutter Removal on Weather Radar signals", Journal of Electromagnetic Waves and Applications, May 2023, DOI:10.1080/09205071.2023.2218044.

- Ramyakrishna Enugonda, V.K Anandan, Basudeb Ghosh, "A new approach to atmospheric turbulence measurements using HOSE on radar backscattered echoes", Journal of Atmospheric and Solar-Terrestrial Physics, Volume 243, February 2023, 106023, ISSN 1364-6826, DOI:10.1016/j.jastp.2023.106023.

- Ramyakrishna Enugonda, V. K. Anandan & Basudeb Ghosh "Higher order spectral analysis of weather signals", Journal of Electromagnetic Waves and Applications, August 2022, DOI: 10.1080/09205071.2022.2112762.

Manuscript Under Preparation

- Ramyakrishna Enugonda, V. K. Anandan & Basudeb Ghosh "Study of Temperature sheets using Higher order Spectral Analysis",**(Under Preparation).**Aim to submit in Elsevier Journal Publications.

List of Workshops/Conferences

- Attended for the SMART training programme on "Principles and Applications of Doppler Weather Radar" held at SAC, Ahmedabad, from 19-22 November 2019.

- E.Ramyakrishna, V.K.Anandan and Basudeb Ghosh, "Study of Weather Signal Characteristics using Higher Order Spectral Analysis". Paper presented at:URSI conference. 12th -14th February 2020(Oral Presentation).

- E.Ramyakrishna, V.K.Anandan and Basudeb Ghosh, "A New Approach to Atmospheric Turbulence Measurements using HOSE on Radar Backscattered Echoes". Paper presented at:International Symposium on TropicalMeteorology (INTROMET 2021)". 23rd-26th November, 2021(Oral Presentation).

- E.Ramyakrishna, V.K.Anandan and Basudeb Ghosh, “Observation of Bow Echoes during mesoscale convective event by X-band Polarimetric Doppler weather Radar”. Paper presented at:IRAD conference. 9th-11th January, 2022(Oral Presentation).

- Attended for the Annual Monsoon E-Workshop and National E-Symposium on “Changing climate and extreme events: impacts, mitigation & Role of oceans” for the presentation on “Turbulence studies during a convective system using nonlinear Properties” through online on 21st – 23rd February 2022, which is organized by Indian Meteorological Society, Pune Chapter (IMSP) (Oral Presentation).